Draft version October 1, 2025
Typeset using LaTeX **twocolumn** style in AASTeX7.0.1

The Open-Source `Photochem` Code: A General Chemical and Climate Model for Interpreting (Exo)Planet Observations

Nicholas F. Wogan,[1,2] Natasha E. Batalha,[2] Kevin Zahnle,[2] Joshua Krissansen-Totton,[3] David C. Catling,[3] Eric T. Wolf,[4,5] Tyler D. Robinson,[6,7] Victoria Meadows,[8] Giada Arney,[9] and Shawn Domagal-Goldman[9]

[1] *SETI Institute, Mountain View, CA 94043*
[2] *NASA Ames Research Center, Moffett Field, CA 94035*
[3] *Dept. Earth and Space Scienes, University of Washington, Seattle, WA 98103*
[4] *Laboratory for Atmospheric and Space Physics, University of Colorado Boulder, Boulder, CO, USA*
[5] *Blue Marble Space Institute of Science, Seattle, WA, USA*
[6] *Lunar & Planetary Laboratory, University of Arizona, Tucson, AZ 85721 USA*
[7] *NASA Nexus for Exoplanet System Science Virtual Planetary Laboratory, University of Washington, Box 351580, Seattle, WA 98195, USA*
[8] *Dept. Astronomy, University of Washington, Seattle, WA 98103*
[9] *NASA Goddard Space Flight Center, Greenbelt, MD 20771, USA*

ABSTRACT

With the launch of the James Webb Space Telescope, we are firmly in the era of exoplanet atmosphere characterization. Understanding exoplanet spectra requires atmospheric chemical and climate models that span the diversity of planetary atmospheres. Here, we present a more general chemical and climate model of planetary atmospheres. Specifically, we introduce the open-source, one-dimensional photochemical and climate code `Photochem`, and benchmark the model against the observed compositions and climates of Venus, Earth, Mars, Jupiter and Titan with a single set of kinetics, thermodynamics and opacities. We also model the chemistry of the hot Jupiter exoplanet WASP-39b. All simulations are open-source and reproducible. To first order, `Photochem` broadly reproduces the gas-phase chemistry and pressure-temperature profiles of all six planets. The largest model-data discrepancies are found in Venus's sulfur chemistry, motivating future experimental work on sulfur kinetics and spacecraft missions to Venus. We also find that clouds and hazes are important for the energy balance of Venus, Earth, Mars and Titan, and that accurately predicting aerosols with `Photochem` is challenging. Finally, we benchmark `Photochem` against the popular `VULCAN` and `HELIOS` photochemistry and climate models, finding excellent agreement for the same inputs; we also find that `Photochem` simulates atmospheres 2 to $\sim 10^2\times$ more efficiently. These results show that `Photochem` provides a comparatively general description of atmospheric chemistry and physics that can be leveraged to study Solar System worlds or interpret telescope observations of exoplanets.

1. INTRODUCTION

In the current era of the James Webb Space Telescope (JWST), our understanding of exoplanets has come from reconciling spectra with atmospheric chemistry and climate models. Researchers routinely rely upon photochemical and climate simulations to interpret JWST detections of disequilibrium species like SO_2, CH_4 and CO_2 in hot Jupiter, sub-Neptune and brown dwarf atmospheres (e.g., S.-M. Tsai et al. 2023; B. Benneke et al. 2024; S. A. Beiler et al. 2024). Models of planetary climate and coupled photochemical-climate models have also become integral to the search for atmospheres of warm rocky exoplanets orbiting M stars. The models predict the expected planetary thermal emission under different atmospheric compositions or thicknesses which are then used to contextualize JWST emission spectra and photometry (e.g., J. Ih et al. 2023; A. P. Lincowski et al. 2023).

The search for exoplanetary life with the next generation Extremely Large Telescopes (ELTs) and NASA's future Habitable Worlds Observatory (HWO) will also depend upon our knowledge of atmospheric chemistry and physics (D. C. Catling et al. 2018; E. W. Schwieterman et al. 2018). The life-detection strategy of these missions is predicated on the circumstellar habitable zone (J. F. Kasting et al. 1993), a theoretical concept that emerged in part from climate calculations of early Venus and Mars (J. F. Kasting 1988, 1991). Photochemistry can enhance (e.g., A. Segura et al. 2005), suppress (e.g.,

S. D. Domagal-Goldman et al. 2011) or mimic biosignatures (e.g., V. S. Meadows et al. 2018, and references therein), and so ELT and HWO detections of CH_4 and O_2 will be significantly more compelling biosignatures if the photochemical context on the planet is well understood (e.g., M. H. Currie & V. S. Meadows 2025). For example, if photochemical calculations suggest the lifetime of CH_4 is short, this would imply a significant surface flux that is more credibly explained by metabolic methanogenesis, rather than geological processes (M. A. Thompson et al. 2022). Similarly, a detection of atmospheric O_2 can be made more robust by assessing and ruling out the likelihood that it is generated by abiotic photolyisis of H_2O and CO_2 (e.g., V. S. Meadows et al. 2018).

The photochemical and climate models used to interpret exoplanet observations should ideally capture the large possible diversity of planetary atmospheres. For some JWST sub-Neptune targets, we do not know whether the planets have primordial Jupiter-like atmospheres, a secondary atmosphere like Venus or Earth's, or no detectable atmosphere (e.g., LHS 1140b; C. Cadieux et al. 2024). Temperate rocky worlds detected by HWO may have Venus-, Earth- or Mars-like atmospheres, or perhaps an entirely unanticipated composition. Evaluating spectra of unexplored worlds will require modeling tools that can reliably accommodate the wide range of possibilities.

Here we describe and validate a more general model of planetary atmospheres: the open-source 1-D photochemical and climate model `Photochem`. Using a single set of kinetics, thermodynamics and opacities, we benchmark `Photochem` against the observed compositions and climates of many Solar System atmospheres: Venus, Earth, Mars, Titan, and Jupiter. We also address the hot Jupiter exoplanet WASP-39b, which resides in a region of parameter space very different from what is found in the Solar System. Our goal is not to perfectly reproduce any single atmosphere. Instead, we aim to demonstrate a description of atmospheric chemistry and physics that broadly captures a wide diversity of planets to enable exoplanet research. A byproduct will be to shed light on poorly understood aspects of Solar System atmospheres, motivating the work needed to improve simulations. All of our calculations are open-source and reproducible to best facilitate future research in this area (https://doi.org/10.5281/zenodo.16509802). `Photochem` has previously been used to study the early Earth (N. F. Wogan et al. 2023), sub-Neptunes (N. F. Wogan et al. 2024; B. Benneke et al. 2024; S. P. Schmidt et al. 2025), hot Jupiters (S. Mukherjee et al. 2024, 2025), and brown dwarfs (N. F. Wogan et al. 2025; S. A. Beiler et al. 2024). Despite these applications of the code, there is no paper that fully describes and benchmarks `Photochem`. This article also serves that purpose.

2. METHODS

The `Photochem` software package contains three modules: 1-D photochemistry (Section 2.2), 1-D climate (Section 2.3), and an equilibrium chemistry solver (Section 2.4). The model is written in Fortran 2008 and modern C and it has a Python interface enabled by Cython (S. Behnel et al. 2011). The source code is available on GitHub[10] and Zenodo (Section 2.6), and pre-built binaries can be installed from the Conda-Forge servers using the Conda package manager.[11] In the following subsections we first describe the heritage of `Photochem` (Section 2.1), then detail the photochemical, climate and equilibrium chemistry modules (Sections 2.2–2.4), and finally give our overall approach for benchmarking the code against Solar System atmospheres (Section 2.5).

2.1. *History and Motivation*

The photochemical and climate models in `Photochem` are motivated in part by the `Atmos` code. `Atmos` was originally developed to study the photochemistry and climate of early Earth, Venus, and Mars (J. F. Kasting et al. 1979; K. J. Zahnle 1986; J. F. Kasting 1988, 1991), and more recently `Atmos` has been further developed, and used to model exoplanet atmospheres (e.g., R. K. Kopparapu et al. 2013; G. Arney et al. 2016; A. P. Lincowski et al. 2018). N. F. Wogan et al. (2022) made a Python wrapper to the photochemical model in `Atmos`, called `PhotochemPy`, which they used to study Earth's Great Oxidation Event. `Atmos` and `PhotochemPy` are written in Fortran 77 and have decades of technical debt, making them challenging to build upon. Therefore, N. F. Wogan et al. (2023) developed a new photochemical and climate model from the ground up: `Photochem`. N. F. Wogan et al. (2023) used `Photochem` version 0.3.14 and the present article describes version 0.6.7.

While `Photochem` is inspired by `Atmos`, the models now have fundamental differences many of which are listed below:

- `Photochem` solves a different derivation of the 1-D photochemical equations than `Atmos` (Section 2.2). The `Atmos` derivation assumes a hard-coded N_2 background filler gas while `Photochem`'s implementation does not require a background gas to be specified.

[10] https://github.com/Nicholaswogan/photochem
[11] https://conda-forge.org/

- The `Atmos` photochemical model is effectively limited to temperate rocky planets, while `Photochem` can consider rocky planets and gas giants over a wide range of temperatures ($\sim$ 50–2000 K).

- The chemical network shipped with `Photochem` is applicable to a wide range of atmospheric temperatures and compositions (Section 3). `Atmos` has several separate chemical networks built for specific planets (e.g., the modern and Archean Earth).

- The photochemical model in `Photochem` can optionally reverse chemical reactions using thermodynamics, whereas `Atmos` cannot. Reversing chemical reactions is important for modeling warm planets ($\gtrsim$ 500 K).

- The photochemical model in `Photochem` can accommodate reactions with an arbitrary number of reactants and products, while `Atmos` can only consider reactions of a specific format.

- The photochemical model in `Atmos` implements a centered finite volume scheme for particle transport and molecular diffusion which can be unstable because both of these processes involve advection. `Photochem` instead implements an upwind scheme to avoid these instabilities (Section 2.2).

- The photochemical model in `Photochem` uses the state-of-the-art CVODE integrator (A. C. Hindmarsh et al. 2005) capable of accurately time-evolving atmospheres. `Atmos` uses a backward Euler method.

- The photochemical model in `Photochem` can have an arbitrary number of condensibles while `Atmos` has a limited number of hard-coded condensibles.

- The climate model in `Photochem` mixes k-distributions using the "resort rebin" method (D. S. Amundsen et al. 2017) permitting the code to include many absorbers (e.g., 10) and still be computationally efficient. The climate model in `Atmos` does not implement a k-distributions mixing method, and therefore is limited to $\lesssim$ 4 absorbers. If the `Atmos` climate model uses more than four absorbers, then the code is prohibitively slow.

- The climate model in `Photochem` uses a novel root-finding method to iterate to radiative-convective equilibrium (RCE; Section 2.3). `Atmos` uses a less efficient time-integration approach.

- The climate model in `Photochem` can consider an arbitrary number of condensibles and their latent heating impact on the convective lapse rate, while `Atmos` only considers the latent heating from H_2O and CO_2.

- `Photochem` can be easily installed with the Conda package manager, without the need for compilers. Using `Atmos` requires a Fortran compiler.

- `Photochem` has a seamless Python wrapper enabled by Cython while `Atmos` does not have an effective Python wrapper.

- The photochemical or climate models in `Photochem` can be used interactively in a Jupyter Notebook or in a Python script, while `Atmos` must be used via its driver Fortran programs.

- `Photochem` can readily perform multiple photochemical or climate calculations in parallel using Python multiprocessing. `Atmos` is much harder to parallelize.

- In `Atmos`, many array sizes are fixed at compile time (e.g., the number of species). Changing the number of species requires you to recompile the code. In contrast `Photochem` dynamically allocates arrays and only needs to be compiled once.

`Photochem` is also based, in part, on the open-source `Cantera` chemical engineering tool (D. G. Goodwin et al. 2024). `Photochem` uses an object-oriented coding approach that is inspired by `Cantera`, and adopts a similar file format for specifying chemical reaction rates and thermodynamics. `Cantera` uses the CVODE integrator (A. C. Hindmarsh et al. 2005) for evolving chemical kinetics, which influenced its use in `Photochem`.

2.2. *Photochemistry*

2.2.1. *Model equations*

Here, we provide a brief description of the fundamental equations solved in the photochemistry module of `Photochem` while Appendix A gives a complete derivation. The photochemistry code is governed by a one-dimensional continuity equation

$$\frac{\partial n_i}{\partial t} = -\frac{\partial}{\partial z}\Phi_i + \sigma_i \tag{1}$$

Here n_i is the number density of a species (atom, molecule, or particle), i per cubic centimeter, t is time in seconds, z is altitude in cm, Φ_i is the flux of molecules cm^{-2} s^{-1}, and σ_i is the source or sink of the species (cm^{-3} s^{-1}). Sources and sinks include chemical reactions, rainout in droplets of water, and condensation or

evaporation. Section 2.2.2 details our chemical reaction network. As is usual in 1-D atmospheric chemistry code, the flux of gases (Φ_i) is determined by molecular and eddy diffusion (Equation (A2)). We assume that particles are transported by a fall velocity (Equation (A3)).

To numerically approximate Equation (1), we discretize altitude with a finite volume method. We use finite volumes because the approximation guarantees molecule conservation, which is not always the case for other discretization techniques (e.g., finite difference or finite element). Conservation is desirable because it allows the model to accurately determine, for example, the fluxes of gases going into and out of the surface of a planet. We use a second-order centered scheme for all spatial derivatives except for the advective terms that arise from molecular diffusion and particle transport, where we use first-order upwind schemes for stability. "Molecular diffusion" is a misnomer because the processes includes both advective and diffusive transport. For a heavy molecule in a light background gas, molecular advection can dominate transport, warranting the stability of an upwind discretization.

Our finite volume discretization converts the Equation (1) system of partial differential equations (PDEs) to a larger system of ordinary differential equations (ODEs) of the form

$$\frac{dn_i^j}{dt} = \Omega_i^j n_i^{j+1} + \Gamma_i^j n_i^j + \Lambda_i^j n_i^{j-1} + \sigma_i^j(n_1^j, n_2^j, ..., n_N^j) \quad (2)$$

Here, the superscript j indexes each altitude grid cell, and N is the total number of species. The Ω_i^j, Γ_i^j, and Λ_i^j coefficients arise from our finite volume method (Appendix A.2). Chemical reactions cause some gases to change concentration much more rapidly than others, which makes the system of ODEs stiff. Therefore, to evolve Equation (2), we use the CVODE stiff integrator (A. C. Hindmarsh et al. 2005) that implements the backward differential formulas.

Any stiff integrator like CVODE requires the Jacobian of Equation (2). Given that dn_i^j/dt largely depends on gas densities in the $j+1$, j and $j-1$ atmospheric layers, the Jacobian is approximately banded with a bandwidth of $2N+1$. We compute the transport Jacobian terms analytically and estimate the chemistry and other source Jacobian terms (σ_i^j) using forward mode automatic differentiation (e.g., J. Revels et al. 2016). In brief, automatic differentiation efficiently computes derivatives by systematically applying the chain rule at the elementary operation level, avoiding the numerical errors of finite differences and the complexity of symbolic differentiation. There was previously no freely available modern Fortran automatic differentiation package that met our needs, so we wrote our own for `Photochem`, called `Differentia`, taking inspiration from the `DNAD` and `ForwardDiff` packages (J. Revels et al. 2016; W. Yu & M. Blair 2013). `Differentia` is open-source and can be used in other Fortran applications (N. Wogan 2025a). In older versions of `Photochem` we computed chemistry Jacobian terms using finite differences, but we have found that using `Differentia` results in more stable integrations.

In this article, we model all atmospheres by computing steady-state solutions of Equation (2) (i.e., $dn_i^j/dt = 0$). This is a reasonable approach because atmospheres are often in quasi-steady-states over geologic time. In our models of Venus, Earth, Mars, Titan, we assume a steady-state is achieved after integrating Equation (2) to ~ 3 billion years. Our simulations of Jupiter and WASP-39b (and other gas-giants) follow the `VULCAN` convergence criteria (S.-M. Tsai et al. 2021) and assume a steady-state when the maximum change of all volume mixing ratios is less than 1% over the last $t_n/2$ seconds, where t_n is the current integration time. While we consider steady-state atmospheres here, `Photochem` can also accurately evolve atmospheres over time. N. F. Wogan et al. (2023) used this feature to study transient atmospheres on the early Earth after massive asteroid impacts.

2.2.2. *Chemical Network*

Our full photochemical network is an updated version of chemistry used in K. Zahnle et al. (2016), N. F. Wogan et al. (2023) and N. F. Wogan et al. (2024). We consider 98 neutral gas-phase species composed of H, O, C, N, S, Cl, and He, connected by 610 forward chemical reactions and 95 photolysis reactions. All 614 non-photolysis reactions are reversed using the principle of microscopic reversibility (C. Visscher & J. I. Moses 2011). The network does not include ions. Photolysis rates are computed using quadrature two-stream radiative transfer (O. B. Toon et al. 1989). The Zenodo archive https://doi.org/10.5281/zenodo.15785405 contains the rate coefficients, citations and notes for each non-photolysis reaction. Most of the rates and thermodynamics from the NIST Kinetic Database and WebBook, although there are exceptions. Table 4 details the source of each photolysis cross section and quantum yield. Many of the photolysis cross sections and yields come from the Leiden and PHIDRATES databases (A. N. Heays et al. 2017; W. F. Huebner & J. Mukherjee 2015).

The network includes 16 condensed-phase species. Most aerosols like condensed H_2O or NH_3 are produced and destroyed through condensation and evaporation (Appendix A.4), while hydrocarbon haze particles form by gas-phase reactions. In reality, in hazy atmosphere

like Titan's and others (e.g., early Earth at certain times), hydrocarbon particles form by the condensation of gas phase molecules that are often larger than what we can model explicitly in our chemical scheme. Therefore, we approximate haze formation by reacting two large hydrocarbons (e.g., $C_2H + C_4H_2$) assuming the products ultimately undergo further polymerization and condensation to haze (P. P. Lavvas et al. 2008). Once particles form, we make no attempt to simulate their detailed microphysical evolution. Particles have a radius prescribed by the user, and fall according to Stokes' law (Appendix A.7) until they leave the bottom of the model domain or evaporate.

2.3. *Climate*

The 1-D climate module in `Photochem` solves for atmospheric radiative and convective energy balance governed by conservation of energy,

$$\rho c_p \frac{\partial T}{\partial t} = \frac{\partial F_{\rm rad}}{\partial z} + \frac{\partial F_{\rm conv}}{\partial z} \tag{3}$$

Here, ρ is the gas density in g cm^{-3}, c_p is the specific heat at constant pressure in erg g^{-1} K^{-1}, T is temperature in Kelvin, and $F_{\rm rad}$ and $F_{\rm conv}$ are the net radiative and convective energy fluxes, respectively, in ergs cm^{-2} s^{-1}. We compute $F_{\rm rad}$ with standard two-steam radiative transfer (O. B. Toon et al. 1989) with optical properties for photolysis, Rayleigh scattering, collision-induced absorption, and aerosols. The user must specify the aerosol densities, radii, and optical properties as a function of pressure (i.e., aerosols must be "painted" onto the atmosphere). We approximate line absorption with k-distributions. The code mixes k-distributions using the "resort rebin" method (D. S. Amundsen et al. 2017). All opacities used in this article are detailed in Table 2, 3 and 4. Our current set of k-distributions are primarily designed for rocky planets, and are not applicable for many gas giants, especially hot Jupiters like WASP-39b. The next several paragraphs describe how we account for convection ($F_{\rm conv}$).

Applying a centered finite volume scheme to Equation (3) yields

$$\left(\rho c_p \frac{dT}{dt}\right)^j = \frac{F_{\rm rad}^{j+1/2} - F_{\rm rad}^{j-1/2}}{\Delta z^j} + \frac{F_{\rm conv}^{j+1/2} - F_{\rm conv}^{j-1/2}}{\Delta z^j} \tag{4}$$

Like in Section 2.2, the super script j denotes an atmospheric grid cell with thickness Δz^j.

Most 1-D climate codes (F. Selsis et al. 2023; G. Arney et al. 2016; M. Malik et al. 2017; T. D. Robinson & D. Crisp 2018) numerically integrate Equation (4) forward in time to a steady-state climate ($\frac{\partial T}{\partial t} = 0$). However, this approach can be prohibitively slow because the upper and lower atmospheric layers often have significantly different rates of temperature change. Small time steps are needed for stability in the low density upper atmosphere, while the deep atmosphere has a large thermal inertia that takes substantially more time to reach an equilibrium. To avoid this problem, `Photochem` instead solves for the steady-state of Equation (4) with a root finding algorithm that permits rapid convergence. Several other climate codes use root finding (e.g., S. Mukherjee et al. 2023; C. P. McKay et al. 1989), however, to our knowledge, these models do not allow for an arbitrary convective pattern in the atmosphere or account for the impact of latent heat on the convective lapse rate. The approach we present below remedies both shortcomings.

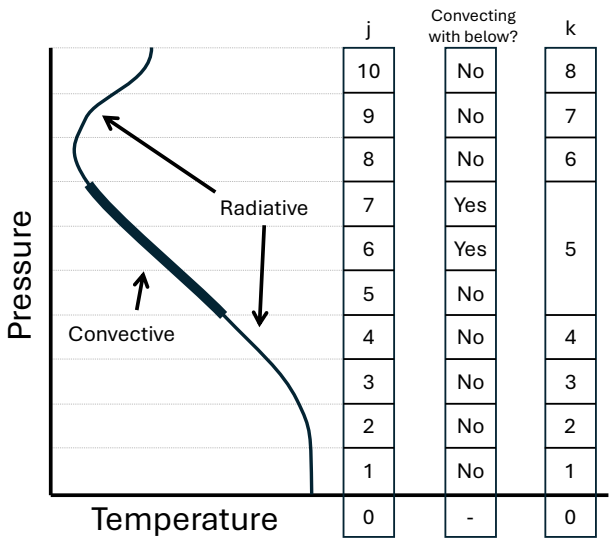

Figure 1. A schematic pressure-temperature profile to aid explanation of our climate model. On the right-hand-side, j indexes each atmospheric layer, and the column labeled "Convecting with below" indicates if a given j layer is convecting with the layer below it. Note that layer $j = 5$ is convecting with the layer above it ($j = 6$), but not with the layer below it ($j = 4$), so it is labeled "No" in the "Convecting with below" column. A new atmospheric grid k can be defined that groups the convecting layers, simplifying the iteration to radiative-convective equilibrium (see text).

To solve Equation (4) with root-finding, we reformulate it to the following:

$$g^j(T^j) = (F_{\rm rad}^{j+1/2} - F_{\rm rad}^{j-1/2}) + (F_{\rm conv}^{j+1/2} - F_{\rm conv}^{j-1/2}) \tag{5}$$

The roots of $g^j(T^j)$ are a temperature profile where the radiative and convecting energy entering and leaving each layer are balanced. The expression ignores all variables relevant to the atmosphere's thermal inertia (ρ, c_p, and Δz).

Now, consider the example temperature profile in Figure 1 divided into 10 atmospheric layers and the ground. Suppose we know which layers are convective and radiative. In Figure 1, layer $j = 7$ is convecting with layer $j = 6$, and $j = 6$ is convecting with $j = 5$. Index k defines a new set of layers where convecting zones are grouped together. For the k grouping, all layers are exchanging energy by radiation only, therefore Equation 5 simplifies to,

$$g^k(T^k) = F_{\text{rad}}^{k+1/2} - F_{\text{rad}}^{k-1/2} \tag{6}$$

We define T^k as the temperature in the lowest j atmospheric layer of the the convecting zone, so in Figure 1, the $k = 5$ and $j = 5$ temperatures are equal. To calculate the radiative fluxes (e.g., $F_{\text{rad}}^{k+1/2}$), we need the temperature of the $j = 6$ and $j = 7$ layers. Our code computes these temperatures by integrating the multispecies pseudo-adiabat in R. J. Graham et al. (2021) upward from the temperature at the bottom of the convective zone. This approach accounts for the latent heating of an arbitrary number of condensibles. Also, Figure 1 has a single convective zone but the algorithm works with any number of convective zones.

Our code solves for the roots of Equation (6) using the "hybrj" routine in `MINPACK` (J. J. Moré et al. 1980), a modified version of Newton's method. The algorithm requires the Jacobian of Equation (6) which we compute with finite differences.

The text above describes how to solve for radiative-convective equilibrium if it is known which atmospheric layers are convecting, but it does not explain how to determine the convecting pattern in the first place. To determine this initial pattern, consider the following reorganization of Equation 4 that ignores convection:

$$h^j(T^j) = \frac{dT^j}{dt} = \left(\frac{1}{\rho c_p}\right)^j \frac{F_{\text{rad}}^{j+1/2} - F_{\text{rad}}^{j-1/2}}{\Delta z^j} \tag{7}$$

Suppose we have a temperature profile T_0^j which can be expressed as the vector $\boldsymbol{T}_0$. Using a single damped Newton iteration, we can perturb $\boldsymbol{h}(\boldsymbol{T}_0)$ towards radiative equilibrium. The Newton perturbation ($\Delta\boldsymbol{T}$) is given by solving the linear equation,

$$\boldsymbol{J_h}(\boldsymbol{T}_0)\Delta\boldsymbol{T} = \boldsymbol{h}(\boldsymbol{T}_0) \tag{8}$$

Here, $\boldsymbol{J_h}(\boldsymbol{T}_0)$ is the Jacobian ($d\boldsymbol{h}/d\boldsymbol{T}$) of $\boldsymbol{h}$ at $\boldsymbol{T}_0$. $\boldsymbol{J_h}(\boldsymbol{T}_0)$ is a square matrix with a width and height equal to the number of atmospheric layers plus the surface layer. The new temperature profile ($\boldsymbol{T}_1$) becomes

$$\boldsymbol{T}_1 = \boldsymbol{T}_0 + \epsilon\Delta\boldsymbol{T} \tag{9}$$

Where, ϵ is a dampening term for the Newton iteration that we set to ~ 0.1. Next, we compare the lapse rate of $\boldsymbol{T}_1$, defined as $\Gamma = \frac{\partial \ln T}{\partial \ln P}$, to the lapse rate of the multispecies pseudo-adiabat (Γ_a) derived in R. J. Graham et al. (2021). We assume convection occurs in layers where the lapse rate exceeds the adiabat ($\Gamma > \Gamma_a$). The above convection scheme is very similar to the "convective adjustment" approaches employed in other codes (e.g., F. Selsis et al. 2023; G. Arney et al. 2016; M. Malik et al. 2017). Other models with "convective adjustment" time integrate Equation (7) to a steady-state and periodically adjust the temperature profile so that the lapse rate does not exceed an adiabat. Our approach modifies this standard "convective adjustment" by replacing the time integration with a root-finding scheme.

Our algorithm finds radiative-convective equilibrium by repeating the Equation (6) root solve and the convection update described above. We consider the temperature structure converged when the convection update does not change the convecting pattern. The scheme works remarkably well, even for fairly crude initial guesses of the temperature profile and convecting regions of the atmosphere. The benchmark in Section 4.5 shows how our root-finding scheme compared to the accelerated time-stepping method in the `HELIOS` climate model.

The climate code takes input gas concentrations as either surface partial pressures or as volume mixing ratios. For a set surface partial pressure, the code distributes the gases throughout the atmospheric column accounting for its saturation vapor pressure, cold trapping, and its latent heating impact on convection. Any specified volume mixing ratio can vary as a function of pressure.

`Photochem` also contains a so-called "inverse" climate model similar to the ones described in R. K. Kopparapu et al. (2013) and J. F. Kasting (1988). We do not use this simple model in this paper, but we briefly describe it here because it is a valuable feature. Given the surface temperature and the reservoir of each atmospheric volatile in terms of partial pressures, the code draws a pseudo-adiabat temperature profile (R. J. Graham et al. 2021) upward until it intersects an assumed isothermal stratosphere. The code then performs radiative transfer on the newly constructed atmosphere to estimate the outgoing longwave and absorbed shortwave radiation. To find a quasi-equilibrium climate, the model solves a non-linear equation for the surface temperature that balances the absorbed and emitted radiation. N. F. Wogan et al. (2023) and N. F. Wogan et al. (2024) previously used this simpler algorithm to reproduce the R. K. Kopparapu et al. (2013) runway greenhouse limit as well as estimate the climate of early Earth and the K2-18b exoplanet.

2.4. *Equilibrium Chemistry*

`Photochem` contains a module that solves for the chemical composition that minimizes the Gibbs energy for a fixed temperature and pressure (i.e., chemical equilibrium). The module is a modified version of `easyCHEM` (E. Lei & P. Mollière 2024) which itself is a clone of the NASA Chemical Equilibrium Analysis tool (S. Gordon & B. J. McBride 1994). The code considers ideal gases and solid-phase species. S. Gordon & B. J. McBride (1994) gives a full description of the numerical method, although in brief, the approach uses the method of Lagrange multipliers to reformulate the Gibbs minimization problem into a system of non-linear equations and solves the system with a variation of Newton's method. We primarily use the equilibrium chemistry solver to set lower boundary conditions for photochemical simulations of gas giants (e.g., Jupiter and WASP-39b; Sections 3.5.1 and 3.6) in which the model domain extends to deep regions of the atmosphere where equilibrium is a valid assumption.

2.5. *Overall Modeling Approach*

We validate `Photochem` against six planetary atmospheres: Venus, Earth, Mars, Titan, Jupiter, and WASP-39b. For each world, we first simulate the atmosphere's photochemistry using a temperature profile and other inputs from the literature, and compare the predicted steady-state composition to observations (Table 5). Next, we compute the planet's steady-state climate with the composition predicted by the photochemical model, and compare the resulting pressure-temperature profile to measured global averages or model predictions from the literature. We do not compute the climate of WASP-39b as our climate model does not include all the opacities relevant to such a hot atmosphere.

To be clear, for our benchmarks, we do not iterate the photochemical and climate model to a completely self-consistent composition and temperature because fully coupled models are hard to interpret. For example, suppose we simulated Venus with a fully coupled model and the resulting deep-atmosphere temperature profile did not match the global average and several chemical species did not agree with observed values. In this case, it would be hard to know if the mismatch is due to a failure in our climate or photochemical models. Independently considering photochemistry and climate avoids this ambiguity. Note that `Photochem` is capable of computing a self-consistent composition and climate, which we illustrate and discuss in Section 4.3.

All nominal simulations use the same chemical network (Section 2.2.2), thermodynamics, opacities, and other model data (Appendix B). However, for some planets we omit species containing chlorine and/or sulfur because we assume these molecules are absent or play a minor role. Our simulations of Venus do not omit any molecules. Models of Mars, Jupiter and Titan only consider H, N, O, C and He species and neglect Cl- and S-containing molecules. Our models of Earth and WASP-39b include S but exclude Cl. Climate simulations use the same set of opacities detailed in Table 2, 3 and 4. All Solar System atmospheres use the ATLAS 3 reference spectrum of the Sun (G. Thuillier et al. 2004) scaled to each world. Our photochemical simulations of WASP-39b use the stellar spectrum presented in S.-M. Tsai et al. (2023).

2.6. *Reproducibility*

Below, we summarize the Zenodo archives that reproduce Section 3, contain the `Photochem` v0.6.7 source code and model data, and archive many of the Solar System atmospheric observations used in this article:

- Reproduce Section 3 calculations: https://doi.org/10.5281/zenodo.16509802 (N. Wogan 2025b)
- Main `Photochem` v0.6.7 source: https://doi.org/10.5281/zenodo.16322107 (N. Wogan 2025c)
- `Photochem` v0.6.7 climate model source: https://doi.org/10.5281/zenodo.15786151 (N. Wogan 2025d)
- `Photochem` v0.6.7 equilibrium solver source: https://doi.org/10.5281/zenodo.16508386 (N. Wogan 2025e)
- `Photochem` v0.6.7 model data: https://doi.org/10.5281/zenodo.15785405 (N. Wogan 2025f)
- `Differentia` v0.1.4: https://doi.org/10.5281/zenodo.15678369 (N. Wogan 2025a)
- Solar System observations (Table 5): https://doi.org/10.5281/zenodo.16509950 (N. Wogan 2025g)

3. RESULTS

In the following subsections we benchmark `Photochem` against the observed compositions and climates of Venus, Earth, Mars, Titan, Jupiter and WASP-39b. All of our work is open-source and can be reproduced with the following Zenodo archive: https://doi.org/10.5281/zenodo.16509802.

3.1. *Venus*

3.1.1. *Photochemistry*

Our approach to modeling Venus's photochemistry is unique compared to previous works (C. J. Bierson & X.

Zhang 2020; L. Dai et al. 2024; F. Wunderlich et al. 2023; P. B. Rimmer et al. 2021). Many past models have fixed the concentration of key species (e.g. OCS and SO_2) at the surface to match observations. Fixing a gas concentration implicitly assumes that there are surface gas fluxes into or out of the planet that maintain the specified abundance. These implicit fluxes can sometimes be justified by geologic processes, such as volcanism or dry deposition, but in other cases the imposed fluxes are unphysical and are merely compensating for flaws in a chemical network.

Here, to avoid surface gas fluxes, we simulate Venus's atmosphere as a closed system where the surface and top-of-atmosphere have zero-flux boundary conditions. We initialize the atmosphere with $\sim$ 96.5% CO_2, 3.5% N_2, 100 ppm SO_2, 35 ppm H_2O, 5 ppm OCS, 10 ppm CO, 500 ppb HCl and 4.5 ppb H_2 (loosely following Table 3 in P. B. Rimmer et al. 2021), which yields the following atomic column abundances in mol cm^{-2}: 0.17 H, 168 N, 4632 O, 2316 C, 0.25 S and 0.0012 Cl. We then evolve the atmosphere to a steady-state with zero-flux boundary conditions for every species, predicting gas concentrations at all altitudes. This approach assumes that surface gas sources and sinks as well as atmospheric escape have minor impacts on Venus's composition compared to gas-phase chemistry. Our model uses the Venus International Reference Atmosphere (VIRA) temperature profile at 45 degrees latitude (A. Seiff et al. 1985) and the P. B. Rimmer et al. (2021) eddy diffusion profile (Figure 13). In addition to gas absorption and scattering, our radiative transfer model also includes H_2SO_4 cloud opacity using optical properties from K. F. Palmer & D. Williams (1975) and accounts for the unknown UV absorber using Equation 11 in P. B. Rimmer et al. (2021) except that we assume the UV absorber has zero optical depth for $\lambda > 400$ nm following V. A. Krasnopolsky (2012). The model accounts for H_2SO_4 condensation, forming droplets with an assumed 2 μm radius. H_2SO_4 droplets form above $\sim$ 50 km and fall to the warm lower atmosphere where they all evaporate before reaching the surface.

Figure 2 shows the predicted steady-state composition for key species in our nominal model compared to observations. For CO, HCl, H_2S, H_2SO_4 and SO, we adequately reproduce observed values at all altitudes. On the other hand, there are some model-data discrepancies for SO_2, H_2O, OCS, S_3, and S_4.

SO_2 and H_2O: Like other photochemical models in the literature (e.g., P. B. Rimmer et al. 2021), we do not capture the observed decrease in SO_2 abundance in and above Venus's clouds ($\gtrsim$ 50 km; L. Zasova et al. 1993). In our model, the main SO_2 and H_2O depletion mechanism is the formation of sulfuric acid droplets:

$$SO_2 + h\nu \rightarrow SO + O \tag{10a}$$
$$SO_2 + O + M \rightarrow SO_3 + M \tag{10b}$$
$$SO_3 + 2\,H_2O \rightarrow H_2SO_4 + H_2O \tag{10c}$$
$$H_2SO_4 \rightarrow H_2SO_4(l) \tag{10d}$$
$$2\,SO_2 + H_2O \rightarrow SO + H_2SO_4(l) \tag{10, net}$$

Reaction 10 requires 1 H_2O molecule to capture 2 SO_2 molecules. In our nominal model, H_2O is 35 ppm and SO_2 is 101 ppm below the clouds consistent with observations (B. Bézard et al. 2011; S. Chamberlain et al. 2013; G. Arney et al. 2014; E. Marcq et al. 2008), hence Reaction 10 mechanism can only decrease SO_2 to 31 ppm, limited by availability of H_2O. Given this mass conservation, it is understandable that our code cannot deplete SO_2 to the $<$ 1 ppm observed near $\sim$ 60 - 80 km (L. Zasova et al. 1993; T. Encrenaz et al. 2012). A solution to this "SO_2 problem" may demand a more sophisticated treatment of Venus' clouds. For example, P. B. Rimmer et al. (2021) proposed that SO_2 might dissolve in H_2SO_4 droplets, a loss process that we do not account for. P. B. Rimmer et al. (2021) argue that dissolution requires a neutralizing base, maybe in the form of hydroxide salts, to increase droplet pH, enhancing its ability to store SO_2.

OCS, S_3 and S_4: Our modeled abundances of OCS, S_3 and S_4 do not match observations in Venus's lower atmosphere ($<$ 50 km). Observations (B. Bézard & C. de Bergh 2007; G. Arney et al. 2014) find that OCS is $\sim$ 15 ppm near the surface, which drops to less than 1 ppm at 35 km altitude. By contrast, our model predicts a constant mixing ratio of $\sim$ 0.6 ppm below 50 km. Also, `Photochem` under predicts S_3 and S_4 in the lower atmosphere compared to observations (V. A. Krasnopolsky 2013), species that are closely coupled to OCS (e.g., $CO + S_3 \leftrightarrow S_2 + OCS$). This model-data disagreement is unsurprising because the relevant sulfur kinetics are poorly understood (Section 4.1). The dotted lines in Figure 2 are the thermochemical equilibrium of each layer in our nominal photochemical model. The equilibrium abundances of OCS, S_3 and S_4 are in closer agreement with the deep-atmosphere observations, suggesting that we are missing chemical pathways or that our existing kinetics are too slow.

O_2: Historically, photochemical models have predicted too much O_2 above the clouds compared to the observational upper-limits (e.g., E. Marcq et al. 2018). Our model does not resolve this mystery. Our nominal simulation predicts an O_2 column of 30×10^{18} molecules cm^{-2}

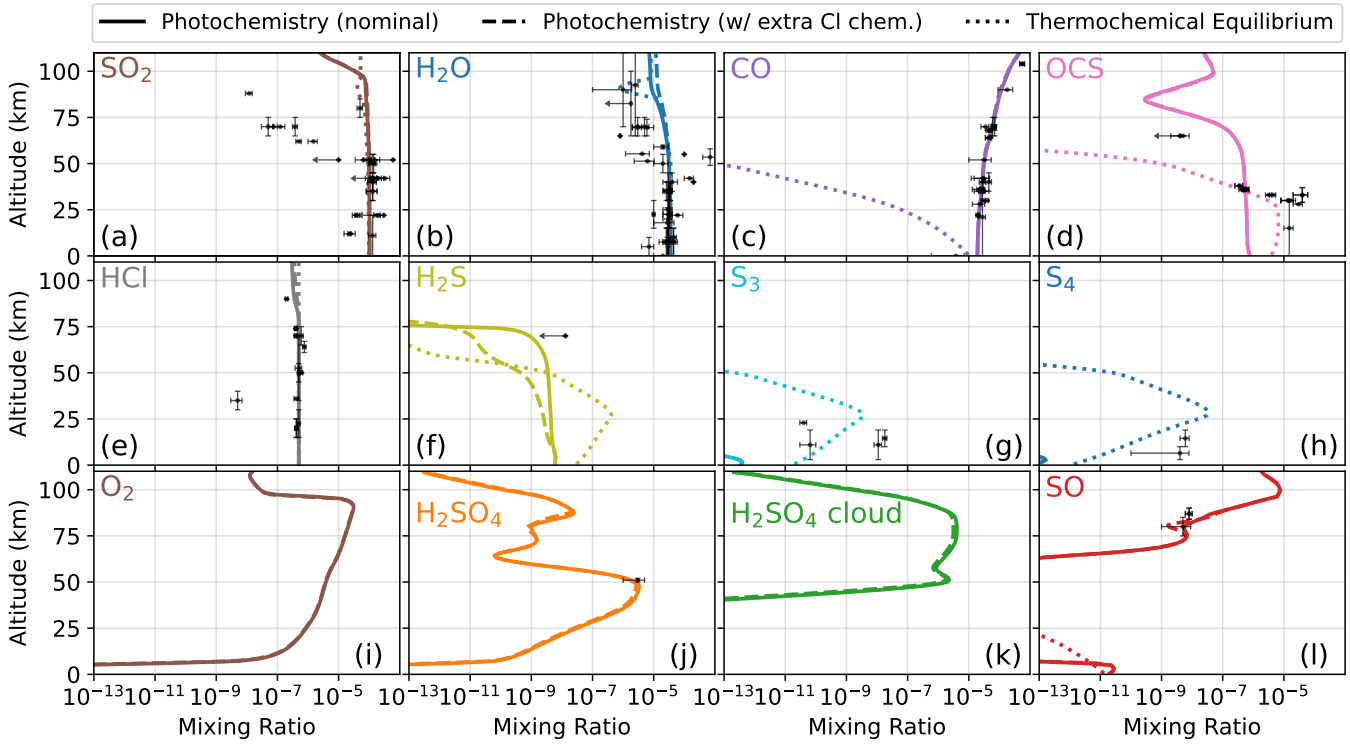

Figure 2. Photochemical simulations of Venus's atmosphere as a closed system (lines) compared to observations (black dots). Table 5 lists the sources for all observations. The solid lines are the nominal model, while the dashed lines are a sensitivity test that adds additional chlorine chemistry as described in Section 3.1.1. The dotted lines are the thermochemical equilibrium of each atmospheric layer in the nominal model. Panel (k) is the H_2SO_4 cloud mixing ratio computed with $f_{H_2OSO_4(l)} = n_{H_2OSO_4(l)}/n$, where $n_{H_2OSO_4(l)}$ is the molecules cm^{-3} in the condensed phase and n is the total gas phase number density. Overall, our nominal model reproduces the observed concentrations of CO, HCl, H_2SO_4, H_2S, and SO at all altitudes, but fails to explain the measured abundances of SO_2, H_2O, OCS, S_3 and S_4. Most of these model-data discrepancies are long standing unsolved problems in Venus photochemistry (P. B. Rimmer et al. 2021; C. J. Bierson & X. Zhang 2020).

above 62 km, while observational upper-limits range between $< 0.8 \times 10^{18}$ and $< 15 \times 10^{18}$ molecules cm^{-2}.

V. A. Krasnopolsky & V. A. Parshev (1981) and Y. L. Yung & W. B. Demore (1982) suggested that catalytic cycles involving ClCO and $ClCO_3$ could draw down O_2 by oxidizing CO to CO_2 (e.g., Equation 4a in Y. L. Yung & W. B. Demore (1982)), chemistry that our nominal model does not account for. The dashed lines in Figure 2 illustrate an additional test that includes this relevant chlorine chemistry. Specifically, we added the species ClCO, $ClCO_3$, $COCl_2$, then added all the reactions in Table 5 of P. B. Rimmer et al. (2021) involving species in our network (see "input/Venus/rimmer2021.yaml" in https://doi.org/10.5281/zenodo.16509802). The additional chlorine chemistry does not substantially change upper-atmospheric O_2 (Figure 2i). The reason is likely because we adopted the mean enthalpy for ClCO reported by J. M. Nicovich et al. (1990) (-21.8 ± 2.5 kJ/mol at 298 K), making the gas thermally unstable in Venus's atmosphere, inhibiting the catalytic cycle. F. P. Mills & M. Allen (2007) found the chlorine catalyzed O_2 destruction is most effective for smaller ClCO enthalpy and a colder upper atmosphere than we used here.

3.1.2. *Climate*

Figure 3 shows several climate simulations of Venus's atmosphere. Our first model (Figure 3a, black lines) adopts the composition and sulfuric acid cloud density from our nominal photochemical simulation shown in Figure 2. Like in our photochemical simulations, the climate model uses the P. B. Rimmer et al. (2021) parameterization for the unknown UV absorber with zero opacity for $\lambda > 400$ nm. Key radiatively active gases include CO_2, H_2O, SO_2, OCS and HCl. The calculation predicts a temperature profile that disagrees with VIRA by 10s of Kelvin at most altitudes (Figure 3a top). Also, the model's net solar fluxes (i.e., shortwave fluxes) are smaller than those measured by Pioneer Venus (Figure 3a, bottom; M. G. Tomasko et al. 1980). These model-data discrepancies can be attributed to the simplified treatment of Venus's clouds. In Figure 3a, we assume the H_2SO_4 cloud aerosols predicted by the photochemical model (Figure 2). The predicted cloud has a total

column mass of 5.5 mg cm^{-2}, a value slightly smaller than the 18 mg cm^{-2} measured by Pioneer Venus (R. G. Knollenberg & D. M. Hunten 1980). However, the predicted cloud has unrealistic optical properties because we assume all aerosols have a 2 μm radius, but, in reality, Venus's clouds have a complex size distribution ranging from 0.5 to nearly 4 microns that changes with altitude (D. Crisp 1986).

Model b in Figure 3 documents a climate simulation where we have instead adopted the cloud optical properties of D. Crisp (1986) which are based on a range of spacecraft and ground-based observations. The predicted temperate profile agrees with VIRA at altitudes below 10^{-2} bar (Figure 3b, top). Additionally, the modeled net solar fluxes match measured values from M. G. Tomasko et al. (1980). This result demonstrates that our photochemical model does not predict an H_2SO_4 cloud layer that reproduces Venus's energy balance.

Both of the Figure 3a and 3b climate simulations use the SO_2 profile from our nominal photochemical model (Figure 2a), which overestimates SO_2 above $\sim$ 50 km. To test the impact of these inaccurate SO_2 concentrations on Venus's energy balance, we performed a third climate simulation (Figure 3c) with the SO_2 profile adjusted so that it matches the data points in Figure 2a. Correcting the SO_2 cools the predicted $\sim 10^{-4}$ bar temperature from $\sim$ 220 K down to $\sim$ 180 K, a temperature more in line with the VIRA P-T profile (Figure 3c).

Our model has also revealed that the planet's energy balance depends strongly on the adopted CO_2-CO_2 collision induced absorption (CIA) opacity. In the Figure 3 simulations that reproduce Venus's climate (and all other climate simulations shown in this paper), we use the same CIA as T. D. Robinson & D. Crisp (2018), except for $\lambda < 2.5$ μm, where use the Y. J. Lee et al. (2016) recommendations. When we instead use the HITRAN CO_2-CO_2 CIA cross sections (T. Karman et al. 2019) the model under-predicts the deep atmosphere opacity leading to surface temperatures that are far too cold ($\lesssim$ 700 K; not shown). Overall, the "HITRAN2020" CIA does not reproduce Venus largely because it does not include any $\lambda < 2.5$ μm opacity (see I. E. Gordon et al. (2022) Table 11 lists bands only from 1-3250 $cm^{-}1$), a region important for capturing the observed emission at the 2.3 μm and 1.7 μm atmospheric windows (e.g., Y. J. Lee et al. 2016). However, the Y. J. Lee et al. (2016) NIR CIA cross sections are not based on laboratory measurements. The NIR CO_2-CO_2 opacities are instead tuned by researchers to permit agreement between Venus observations and radiative transfer models (e.g., E. Marcq et al. 2006; V. Meadows & D. Crisp 1996).

Overall, the Figure 3 simulations demonstrate that our climate model can reproduce Venus's energy balance, provided that we use the observed clouds, the observed SO_2 high altitude mixing ratio, and the NIR CO_2-CO_2 opacity recommended by Y. J. Lee et al. (2016).

3.2. *Earth*

3.2.1. *Photochemistry*

Our photochemical simulation of modern Earth generally follows the model setup of R. Hu et al. (2012), with some modifications. The model adopts the S. T. Massie & D. M. Hunten (1981) eddy diffusion profile, and, for a temperature profile, we use the COSPAR International Reference Atmosphere (CIRA) 1986 at the equator in January (Figure 13). Table 1 shows the surface boundary conditions. We fix the surface pressure of N_2, O_2 and CO_2 to 0.79, 0.213 and 4.05×10^{-4} bar, respectively. The model condenses out H_2O at the input 40% relative humidity, which sets the tropospheric concentration. Earth's average relative humidity varies between 77% near the surface and 20% at the tropopause (S. Manabe & R. T. Wetherald 1967). Our model only accepts a single altitude-independent relative humidity, so we choose 40% as an average tropospheric value. Water condensation in the atmosphere forms droplets with prescribed 10 μm radii that fall to the surface. The calculation uses a range of surface gas fluxes and deposition velocities (Table 1) from the literature (e.g., J. H. Seinfeld & S. N. Pandis (2016) and D. A. Hauglustaine et al. (1994)), that represent biologic production (e.g., N_2O from denitrification), anthropogenic sources (e.g., CO from burning fossil fuels), and dry deposition. Gases are also removed from the atmosphere using the F. Giorgi & W. L. Chameides (1985) parameterization for rainout in droplets of H_2O assuming modern Earth's rainfall rate of 1.1×10^{17} molecules cm^{-2} s^{-1} (F. Giorgi & W. L. Chameides 1985). We turn on diffusion-limited H and H_2 escape to space. `Photochem` simulates diffusion-limited H and H_2 escape with an effusion velocity at the upper boundary determined by their rate of molecular diffusion through the background gas.

Figure 4 shows that our `Photochem` simulation of Modern Earth broadly reproduces much of the observed trace gases in the atmosphere. For the observations in Figure 4 that do not report an error, we follow S.-M. Tsai et al. (2021) and assume one order-of-magnitude error bars to account for diurnal and spatial variations. Therefore, many error bars in Figure 4 do not represent one standard deviation uncertainty in a measurement. Our predicted gas abundances result from well-established chemistry in the atmospheric science literature (e.g., see

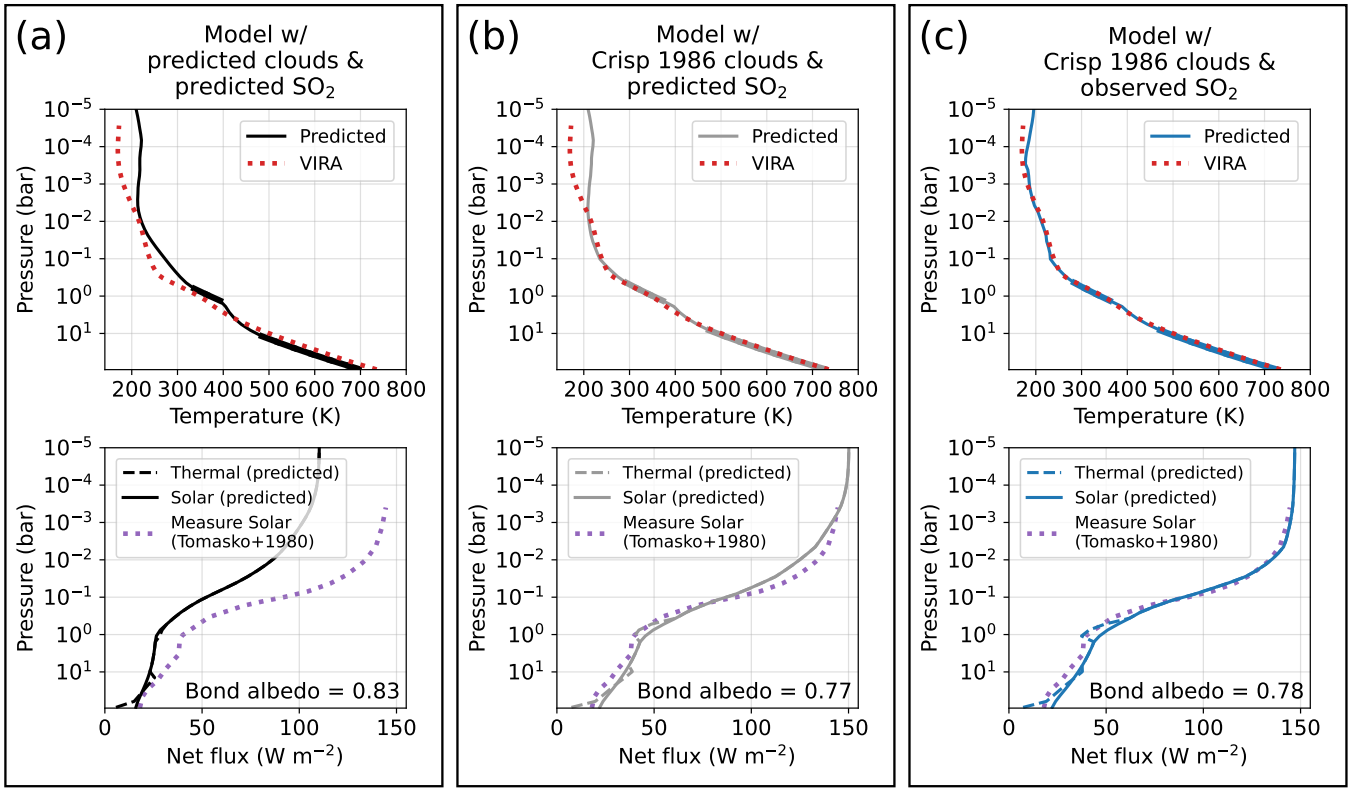

Figure 3. Climate simulations of Venus's atmosphere. (a) A climate model that uses the H_2SO_4 clouds and gas concentrations predicted by the nominal photochemical simulation in Figure 2. (b) The same as (a), except the model uses observed cloud optical properties from D. Crisp (1986). (c) The same as (b), except the simulation uses Venus's observed SO_2 profile. In (a), (b) and (c), the top panels shows predicted temperature profiles compared to the Venus International Reference Atmosphere (VIRA, A. Seiff et al. 1985). Thick portions of the predicted P-T profile indicate convecting layers. The bottom panels are the net thermal and solar fluxes compare to the solar fluxes measured by Pioneer Venus (M. G. Tomasko et al. 1980). Our climate model can reproduce Venus's energy balance (panel (c)) when we correct for inaccurate clouds and SO_2 predicted by the photochemical model.

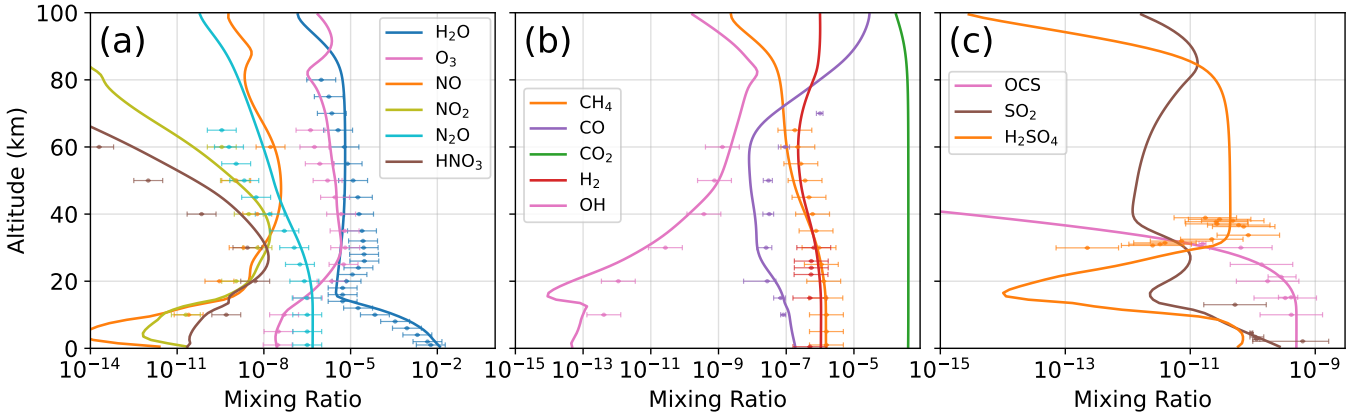

Figure 4. Photochemical simulation of modern Earth's atmosphere (lines) compared to observations (dots). Table 5 lists the sources for all observations. For observations that do not give an error bar, we assume a one order-of-magnitude error to account for diurnal and spatial variations following S.-M. Tsai et al. (2021). `Photochem` broadly reproduces the observed composition of Earth's atmosphere.

Table 1. Modern Earth lower boundary conditions

Species	Pressure (bar)	Surface Flux (molec. cm^{-2} s^{-1})	v_{dep} (cm s^{-1})	Ref.
H_2O	40% RH	-	-	-
N_2	0.79	-	-	-
O_2	0.213	-	-	-
CO_2	4.05×10^{-4}	-	-	-
CO	-	3.7×10^{11}	0.03	a, b
CH_4	-	1.4×10^{11}	0	c
NO	-	3×10^{9}	0.01	a, b
N_2O	-	1.5×10^{9}	0	d, b
NH_3	-	1.5×10^{10}	1	a, e
NO_2	-	0	0.05	b
NO_3	-	0	0.05	b
SO_2	-	9×10^{9}	1	a
H_2S	-	2×10^{8}	0.015	a, e
OCS	-	5.4×10^{7}	0.003	a, f
H_2SO_4	-	7×10^{8}	1	a, e
HCN	-	1.7×10^{8}	0.13	g, f
CH_3CN	-	1.3×10^{8}	0.13	g, f
HNO_3	-	0	4	f

Notes. a: J. H. Seinfeld & S. N. Pandis (2016); b: D. A. Hauglustaine et al. (1994); c: R. B. Jackson et al. (2020); d: E. W. Schwieterman et al. (2022); e: R. Hu et al. (2012); f: S.-M. Tsai et al. (2021); g: Q. Li et al. (2003)

chapter 5 and 6 of J. H. Seinfeld & S. N. Pandis 2016). For example, stratospheric ozone is produced and destroyed by the Chapman mechanism (e.g., J. H. Seinfeld & S. N. Pandis 2016) as well as several catalytic cycles. One important cycle involves NO and NO_2, where the NO is largely sourced from a surface flux boundary condition (Table 1):

$$NO + O_3 \rightarrow NO_2 + O_2 \quad (11a)$$
$$NO_2 + O \rightarrow NO + O_2 \quad (11b)$$
$$O_3 + O \rightarrow 2\,O_2 \quad (11, \text{net})$$

OH and HO_2 also destroy ozone with the same net reaction:

$$OH + O_3 \rightarrow HO_2 + O_2 \quad (12a)$$
$$HO_2 + O \rightarrow OH + O_2 \quad (12b)$$
$$O_3 + O \rightarrow 2\,O_2 \quad (12, \text{net})$$

The hydroxyl radicals (OH) in Reaction 12 are supplied by the net photochemical reaction of ozone with water vapor: $O_3 + h\nu \rightarrow O(^1D) + O_2$ followed by $O(^1D) + H_2O \rightarrow OH + OH$. Our model ignores catalytic loss of O_3 from chlorine chemistry. As a result of ozone production from the Chapman mechanism and the destruction paths listed above, our model estimates a total O_3 column of 193 Dobson Units (DU), a value consistent with the $\sim$ 190 to 500 DU range observed on modern Earth (R. J. Salawitch et al. 2022).

Hydroxyl plays a critical role in several systems beyond ozone photochemistry. One example is the oxidation of CH_4, beginning with $CH_4 + OH \rightarrow CH_3 + H_2O$. This reaction determines methane's lifetime in the atmosphere, which we find to be $\sim$ 10 years, consistent with literature estimates (D. C. Catling & J. F. Kasting 2017). Including the CH_4 + OH reaction, the carbon in CH_4 is ultimately oxidized to CO_2 through a series of $\sim$ 6 reactions via the following intermediates: CH_3, CH_3O_2, CH_3O, H_2CO and CO.

Like in Venus's atmosphere, SO_2 in Earth's atmosphere is photochemically processed to sulfuric acid, although the mechanism is different because of Earth's more plentiful hydroxyl. On Earth, SO_3 forms by $SO_2 + OH + M \rightarrow HSO_3 + M$ followed by $HSO_3 + O_2 \rightarrow HO_2 + SO_3$, then sulfuric acid is produced from Reaction 10c. In the troposphere, H_2SO_4 dissolves in water droplets and rains out of the atmosphere. In the upper troposphere and lower stratosphere, H_2SO_4 condenses to sulfuric acid aerosols, which, in our model, fall until they evaporate at $\lesssim$ 10 km altitude.

To summarize, `Photochem` works well for Earth. The code captures the important chemistry in Earth's atmosphere, reproducing its observed composition.

3.2.2. *Climate*

Our climate simulations of Earth use most of the gas abundances predicted by our photochemical model shown in Figure 4. One exception is the water profile, which the climate code calculates to be self-consistent with the temperature profile for a 40% relative humidity. Another exception is that we consider two total ozone column abundances: one with 193 dobson units (DU) from our Figure 4 photochemical model, and the other with 500 DU. These ozone concentrations span typical values for Earth (R. J. Salawitch et al. 2022). Following many previous 1-D models of Earth (e.g., J. F. Kasting et al. 1984), we account for water clouds by using a surface albedo of 0.2, which is larger than Earth's true value of $\sim$ 0.15. This approach effectively "paints" clouds on the surface. We take this approach because our model cannot yet account for patchy clouds. We reserve a more complete treatment of clouds to future work (Section 4.2).

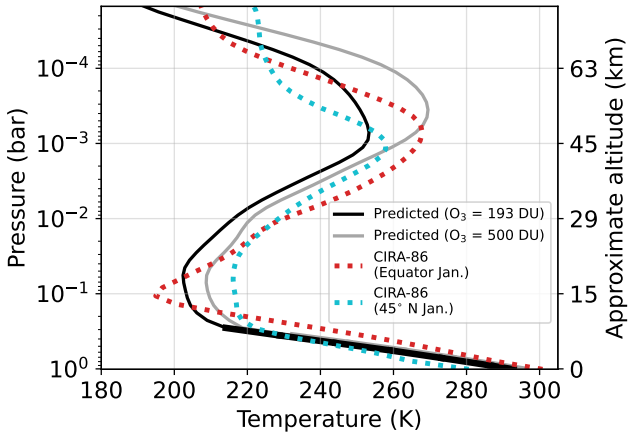

Figure 5. Climate simulations of modern Earth's atmosphere with 193 and 500 DU of ozone (black and grey lines, respectively) compared to temperature profiles at the equator and 45° N (red and blue lines, respectively) in January from the COSPAR International Reference Atmosphere 1986 (CIRA-86). Thick portions of the predicted P-T profiles indicate convection. Our model broadly reproduces Earth's pressure-temperature profile.

Figure 5 shows computed P-T profiles for two ozone columns (193 DU and 500 DU for the black and gray lines, respectively), compared to January equator and 45° N temperature profiles from the COSPAR International Reference Atmosphere 1986 (CIRA-86). In both simulations, we compute a surface temperature near $\sim$ 290 K, a tropopause at 15 km with a $\sim$ 210 K temperature, and a stratopause near 50 km with a $\sim$ 250 and 270 K temperature, all values consistent with Earth's global average P-T profile (e.g., Chapter 1 of D. C. Catling & J. F. Kasting (2017)).

3.3. *Mars*

3.3.1. *Photochemistry*

Our photochemical simulation of Mars is largely motivated by the model setup of K. Zahnle et al. (2008). We use their temperature and eddy diffusion profiles (Figure 13). For boundary conditions, the we fix the surface CO_2 and N_2 pressures to 6.0 and 0.03 mbar, respectively, and sets the H_2O relative humidity of condensation to 10%. Note however, that Mars' relative humidity is highly variable (E. Fischer et al. 2019). We include 0.02 cm/s deposition velocities for H_2O_2 and O_3 that represent the atmospheric oxidation of Mars's surface. H_2 and H escape the model domain at the diffusion limited rate. Our model ignores oxygen escape and assumes that H_2O_2 and O_3 deposition represent the main loss of oxidants from the atmosphere. K. Zahnle et al. (2008) showed that Mars' simulated atmospheric composition is insensitive to whether oxidants leave the atmosphere from surface deposition or from escape.

The computed steady-state composition, shown in Figure 6a, is generally consistent with a wide range of atmospheric observations and with several past models of Mars's chemistry (K. Zahnle et al. 2008; V. A. Krasnopolsky 2006a). The trace abundances of CO, O_2, H_2, O_3, and H_2O_2 are the result of CO_2 and H_2O photochemistry. CO_2 photolysis produces CO and atomic oxygen, and ultimately O_2 and O_3 after the O atoms combine. Water vapor photolysis yields OH and atomic hydrogen. Hydrogen atoms liberated by water photolysis react quickly with O_2 to form HO_2 ($H + O_2 + M \Rightarrow HO_2 + M$). When HO_2 reacts with O, it creates OH that speeds CO_2 recombination:

$$H + O_2 + M \rightarrow HO_2 + M \quad (13a)$$
$$HO_2 + O \rightarrow OH + O_2 \quad (13b)$$
$$CO + OH \rightarrow CO_2 + H \quad (13c)$$
$$\overline{\qquad\qquad\qquad\qquad}$$
$$CO + O \rightarrow CO_2 \quad (13, \text{net})$$

Direct CO_2 recombination by $CO + O + M \rightarrow CO_2 + M$ is slow because it is spin-forbidden. HO_2 can also react with a hydrogen atom to make H_2, or with itself to form H_2O_2. The H_2 escapes to space, while H_2O_2 is lost to surface deposition.

3.3.2. *Climate*

Mars's climate depends on two main opacity sources: CO_2 gas and dust aerosols. The planet has a clear season with little atmospheric dust during 0–180 Solar longitude (northern spring and summmer), and a relatively dusty atmosphere for the remainder of the year because perihelion occurs then at 251 solar longitude (e.g., L. Montabone et al. 2015). Also, every several years, Mars has global dust storms. We construct three climate models corresponding to the three levels of dust-loading. The simulations use the global and annual mean dust radii and density profiles from the Ames Legacy Mars GCM M. A. Kahre et al. (2023) and, also following M. A. Kahre et al. (2023), we use dust optical properties from M. J. Wolff et al. (2009) based on Mars Reconnaissance Orbiter observations. We scale the dust density such that 9.3 μm dust optical depths of 0.075, 0.375, and 1 represent the clear season, the dusty season, and a global dust storm. These optical depths are based on a compilation of spacecraft observations analyzed in L. Montabone et al. (2015) (see their Figure 21). The models use gas abundances from our photochemical model (Figure 6a) and uses a 0.2 surface albedo.

Figure 6b shows that the three climate simulations encompass the ±45° latitude average from the M. A.

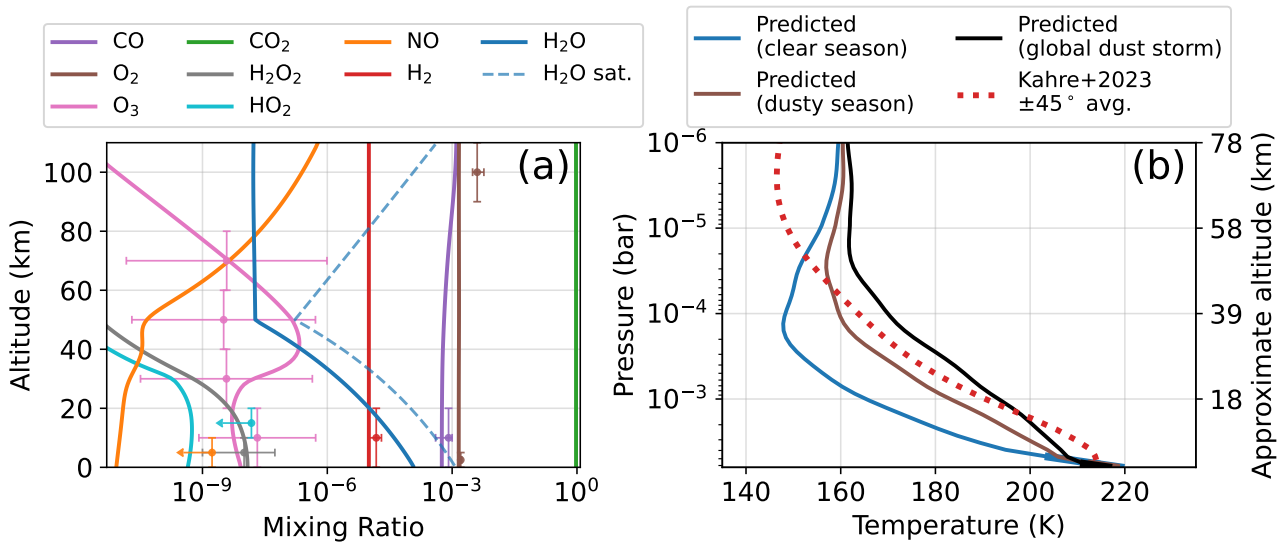

Figure 6. (a) A photochemical model of Mars (lines) compared to observations (dots). Table 5 lists the sources for all observations. The dashed blue line is the saturation mixing ratio of H_2O. (b) Three climate simulations of Mars representing the clear season (blue line), dusty season (brown line), and a global dust storm (black line). The red dotted line is a $\pm 45^{\circ}$ latitude average from the Ames Legacy Mars GCM M. A. Kahre et al. (2023). Thick portions of the predicted P-T profiles indicate convection. The `Photochem` code generally reproduces Mars composition (panel (a)) and climate (panel (b)).

Kahre et al. (2023) GCM. More dust increases sunlight absorption and warms much of the atmosphere above 5 km and has a minor cooling effect on the surface. In the "clear" and "dusty" models, near infrared CO_2 sunlight absorption causes a temperature inversion at $P \lesssim 10^{-4}$ bar. Our models compute a warmer temperature than the M. A. Kahre et al. (2023) average for $P < 10^{-5}$ bar, although we do not consider this an issue. Mars Trace Gas Orbiter observations and other spacecraft have shown that Mars's $\sim 10^{-6}$ bar temperature varies between $\sim$ 120 and 180 K (e.g., see Figure 8 in M. A. López-Valverde et al. (2023)). We conclude that the $\sim$ 160 K at $\sim 10^{-6}$ bar computed by `Photochem` is reasonable.

3.4. *Titan*

3.4.1. *Photochemistry*

To model Titan's photochemistry, we use the P-T profile from Figure 3 in R. Moreno et al. (2012) and the J. C. Loison et al. (2015) eddy diffusion coefficient (Figure 13). For boundary conditions, the model fixes the surface N_2 to 1.5 bar and CO to 76.5×10^{-6} bar (i.e., $\sim 5.1 \times 10^{-5}$ mixing ratio). We assume a 100% CH_4 relative humidity of condensation. We add 5×10^6 molecules cm^{-2} s^{-1} downward fluxes of O and OH at the top of the atmosphere, representing in-fall from micrometeorite ablation (J. C. Loison et al. 2015). Mass leaves the atmosphere from diffusion limited H_2 escape, and when aerosols (haze or condensed CH_4, C_2H_6, HCN, etc.) fall to the surface. Haze particles have an assumed constant 0.5 micron radius based loosely on M. G. Tomasko et al. (2008b) with B. N. Khare et al. (1984) Mie optical properties. We model the production and transport of a number of other condensate aerosols (i.e., C_2H_6, C_2H_2, HCN, etc.) with an assumed 10 μm radii, although we do not account for how they absorb or scatter sunlight. The model accounts for the influence of Galactic Cosmic Rays (GCR) by prescribing altitude-dependent N_2 destruction and N and N(^{2}D) production rates given by P. P. Lavvas et al. (2008) (their Figure 3). We assume 82.5% of N_2 GCR destruction forms grounds state N and 17.5% makes N(^{2}D). Titan is the only planet in this article where we considering GCR effects.

Our computed steady-state composition generally agrees with observations to within a factor of several (Figure 7). One exception is that we underpredict the observed NH_3 abundances near 1000 km by about four orders of magnitude. According to J. C. Loison et al. (2015), ion chemistry is important to NH_3 formation in the upper atmosphere, a process that we ignore.

Like in previous work (e.g., P. P. Lavvas et al. 2008; J. C. Loison et al. 2015; B. K. D. Pearce et al. 2020), we find that CH_3 is an important radical in Titan's atmosphere. At high altitudes CH_3 forms from CH_4 photolysis, while at lower altitudes, it is created catalytically

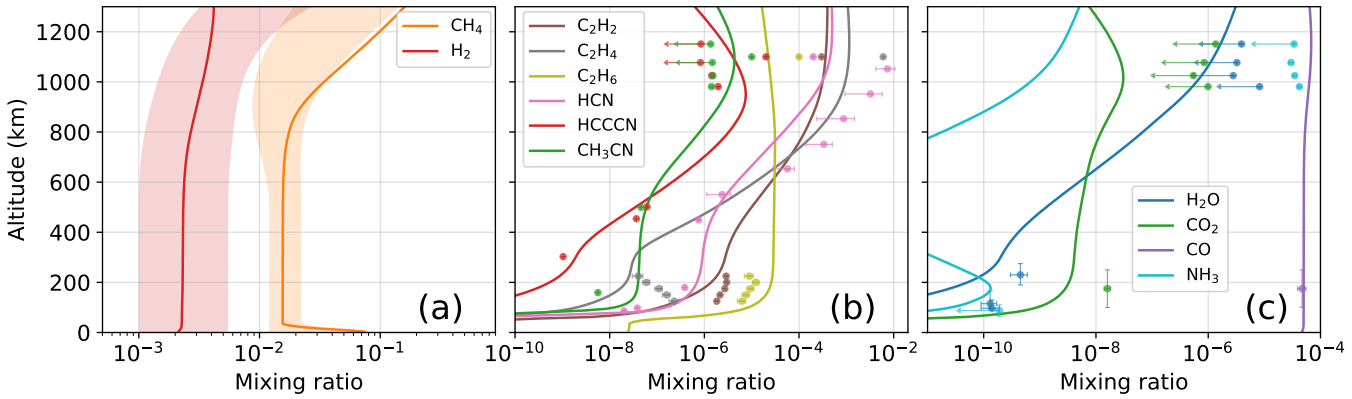

Figure 7. A photochemical simulation of Titan's atmosphere (lines) compared to observations (dots and shading). Some observations do not have error bars because no error was reported. The shading in panel (a) outlines the minimum and maximum H_2 and CH_4 concentrations from the J. H. Waite et al. (2013) empirical model of Titan. Table 5 lists the sources for all observations. For all species, except NH_3, the model is within a factor of several of observed concentrations.

from acetylene:

$$C_2H_2 + h\nu \rightarrow C_2H + H \quad (14a)$$
$$C_2H + CH_4 \rightarrow C_2H_2 + CH_3 \quad (14b)$$
$$\text{---}$$
$$CH_4 \rightarrow CH_3 + H \quad (14, \text{net})$$

Methyl radicals combine to make C_2H_6 ($CH_3 + CH_3 + M \rightarrow C_2H_6 + M$) and also help create C_2H_4 through several intermediate steps. C_2H_4 photolysis is the primary source for C_2H_2. Consistent with previous research (e.g., B. K. D. Pearce et al. 2020), we find that HCN is primarily created by a sequence of reactions involving CH_3:

$$N_2 + h\nu \rightarrow N + N(^2D) \quad (15a)$$
$$N + CH_3 \rightarrow H + H_2CN \quad (15b)$$
$$N(^2D) + CH_4 \rightarrow H_2CN + H_2 \quad (15c)$$
$$H_2CN + H \rightarrow HCN + H_2 \quad (15d)$$
$$\text{---}$$
$$N_2 + CH_4 + CH_3 + H \rightarrow 2\,HCN + 3\,H_2 \quad (15, \text{net})$$

About 50% of the N_2 dissociation in Reaction (15a) is from UV photolysis and the other half is from GCRs. Cyanoacetylene (HCCCN) is created when HCN reacts with C_2H: $C_2H + HCN \rightarrow HCCCN + H$.

The main hydrocarbons and nitriles are destroyed by haze formation throughout the atmosphere or by direct condensation at $\lesssim$ 100 km altitude. Following P. P. Lavvas et al. (2008), we parameterize haze formation with three reactions, the most important being $H_2CN + HCN \rightarrow$ haze. In total, our code predicts a haze production rate of 7×10^{-15} g cm^{-2}, in agreement with other estimates (C. P. McKay et al. 2001). The loss of hydrocarbons and nitriles to condensation leaves behind H_2 (e.g., Reactions (14) and (15)) near $\sim 0.2\%$ that escapes at the diffusion limited rate.

3.4.2. *Climate*

Figure 8 shows three climate models of Titan compared to the minimum and maximum temperature profiles from the J. H. Waite et al. (2013) empirical model. Our nominal simulation (Figure 8a), uses the gas concentrations and haze densities predicted by our photochemical model (Figure 7). Important opacities include haze aerosols, CH_4, C_2H_6, C_2H_4, as well as N_2-N_2, N_2-CH_4 and N_2-H_2 collision induced absorption. The nominal case predicts an acceptable bond albedo of 0.25 (E. C. Creecy et al. 2021) and a 99 K surface temperature, a value only several degrees warmer than Titan's $\sim$ 95 K global average (C. P. McKay et al. 1989). However, the computed 10^{-3} to 10^{-6} bar temperature is 140–150 K, but Titan's observed value is closer to $\sim$ 180 K at these altitudes (J. H. Waite et al. 2013).

Titan's stratospheric temperature is largely determined by the balance of CH_4, C_2H_6 and C_2H_4 infrared emission, and heating when CH_4 and haze aerosols absorb sunlight (C. P. McKay et al. 1989). The model uses CH_4, C_2H_6 and C_2H_4 concentrations that generally agree with observations (Figure 7), so we expect the code is adequately accounting for their emission. On the other hand, the haze opacity in the Figure 8a model is questionable because we crudely assume that all haze particles have a 0.5 μm radius with the B. N. Khare et al. (1984) optical properties using Mie theory. Indeed, the simulated net solar fluxes disagree with fluxes derived from Cassini/Huygens observations (Figure 8a, bottom; M. G. Tomasko et al. 2008a).

Figure 8b shows an additional climate simulation that uses the M. G. Tomasko et al. (2008b) haze optical properties inferred from Huygens probe observations.

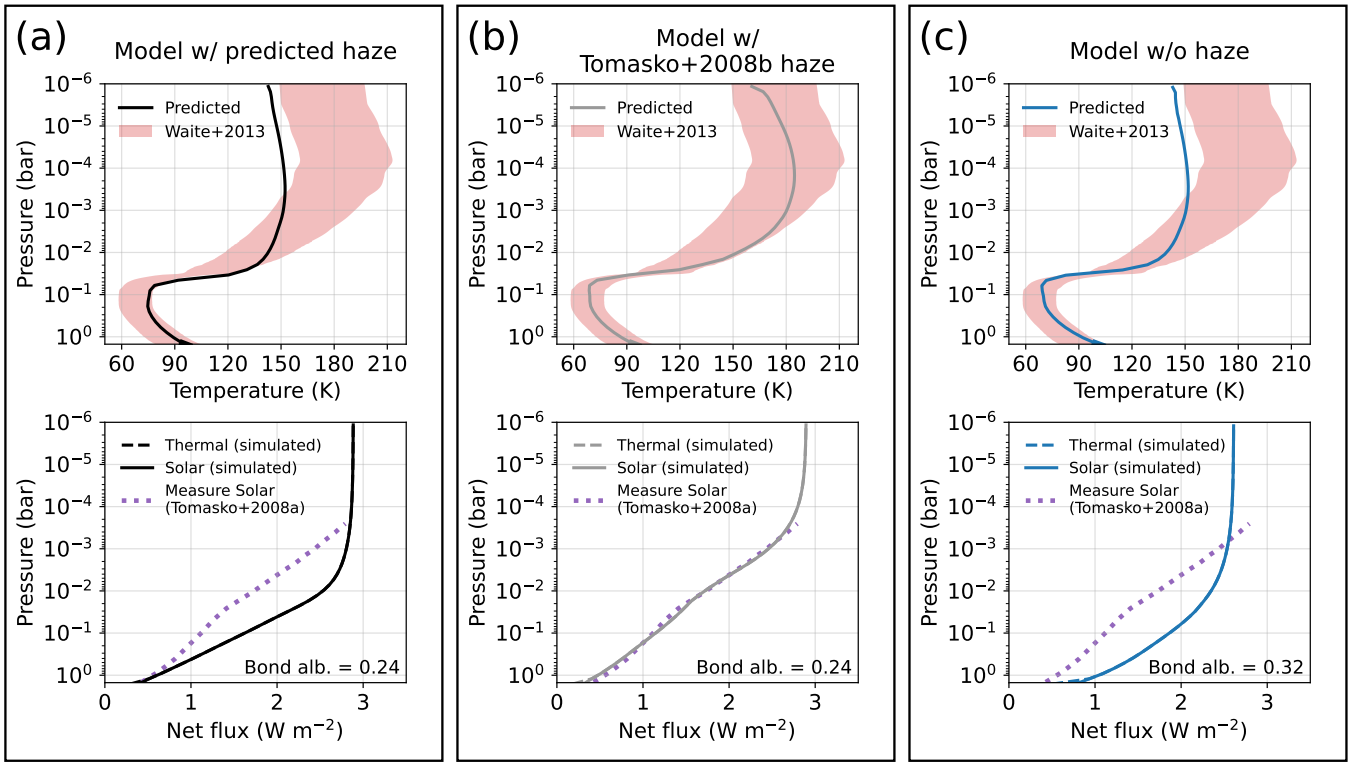

Figure 8. Climate simulations of Titan's atmosphere. (a) A climate model that uses the haze and gas concentrations predicted by the Figure 7 photochemical model. (b) The same as (a), except that the model replaces the computed haze with the observed M. G. Tomasko et al. (2008b) haze optical properties at solar wavelengths based on the Cassini/Huygens mission. (c) The same as (a), except that the model removes all haze opacity. In (a), (b) and (c), the top panels show predicted temperature profiles compared to the minimum and maximum of the J. H. Waite et al. (2013) empirical model (red shading). The bottom panels are the net thermal and solar fluxes compare to solar fluxes from Cassini/Huygens (Figure 3 in M. G. Tomasko et al. 2008a). Our climate model can reproduce Titan's energy balance (panel (b)) when we correct for the inaccurate haze opacities predicted by the photochemical model.

Specifically the model uses the M. G. Tomasko et al. (2008b) haze opacities between 350–5000 nm, and the haze predicted by our photochemical model in the infrared (> 5000 nm). We do not replace our far-infrared haze optical properties with measured values because Huygens did not observe them. The predicted temperature profile and net solar fluxes in Figure 8b agree with observations, even in the stratosphere. We estimate a 97 K surface temperature that is consistent with Titan's measured global average (∼ 95 K; C. P. McKay et al. 1989). This result demonstrates that our photochemical model does not predict a haze that reproduces Titan's energy balance.

To further test the radiative impact of Titan's haze, we conduct an additional simulation that removes all haze opacity (Figure 8c). The haze-free model yields a too warm 104 K surface temperature showing, like previous work (C. P. McKay et al. 1991), that Titan's haze has an anti-greenhouse effect.

3.5. *Jupiter*

3.5.1. *Photochemistry*

We conclude our tour of the Solar System with Jupiter. Our photochemistry setup follows the similar calculation in S.-M. Tsai et al. (2021). We use their P-T profile and eddy diffusion coefficient (Figure 13). The lower boundary of the model is at 10,000 bars where we fix all species to a chemical equilibrium concentration for the following composition: He/H = 0.0785 (0.92× solar; S. K. Atreya et al. 2020), C/H = 1.2×10^{-3} (4.4× solar S. K. Atreya et al. 2020), O/H = 2.6×10^{-4} (0.5× solar; T. Cavalié et al. 2023), and N/H = 2×10^{-4} (2.9× solar; C. Moeckel et al. 2023). At the upper boundary, near $\sim 3 \times 10^{-9}$ bar, we impose a downward flux of 4×10^4, 4×10^4, and 10^4 molecules cm^{-2} s^{-1} for H_2O, CO and CO_2, respectively, capturing micrometeorite ablation.

Figure 9 shows that our photochemical simulation matches observations at most altitudes. One notable exception is that our model underpredicts C_2H_6 near 10^{-2} bars by roughly one order of magnitude. Previous

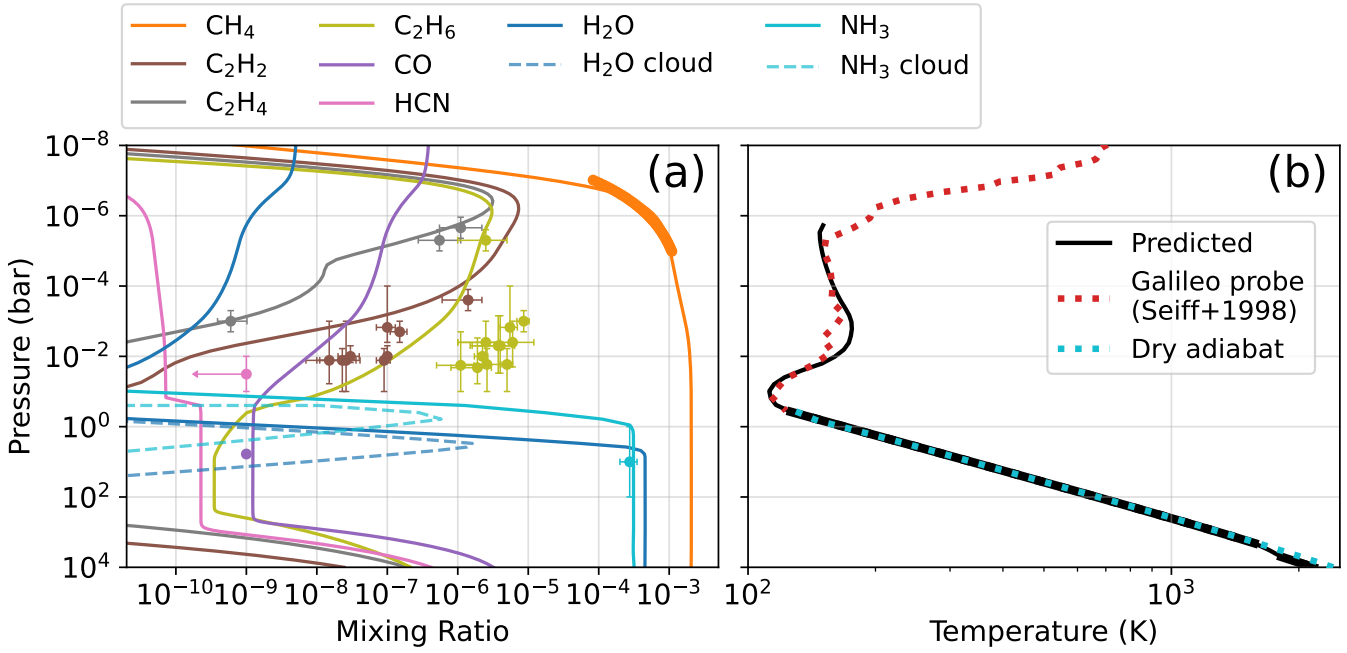

Figure 9. (a) A photochemical model of Jupiter (lines) compared to observations (dots). Table 5 lists the sources for all observations. (b) A climate simulation of Jupiter's atmosphere (black line). Thick portions of the predicted P-T profiles indicate convection. The red dotted line is from A. Seiff et al. (1998) profile based on Galileo probe measurements, and the cyan dotted line is a dry He/H_2 adiabat. `Photochem` captures the main chemistry in Jupiter's atmosphere and reproduces the planet's pressure-temperature profile.

photochemical models have been able to fit these C_2H_6 concentrations with the same P-T-K_{zz} profile that we use here (J. I. Moses et al. 2005; S.-M. Tsai et al. 2021; P. B. Rimmer & C. Helling 2016). However, we believe that S.-M. Tsai et al. (2021) and P. B. Rimmer & C. Helling (2016) were only able to reproduce these data by using CH_4 cross sections from PHIDRATES (W. F. Huebner & J. Mukherjee 2015; W. F. Huebner et al. 1992), which incorporates CH_4 photolysis up to 237.2 nm. The $\lambda > 160$ nm CH_4 cross sections in PHIDRATES ($\leq 6 \times 10^{-24}$ cm^2 molecule^{-1}) appear to be extrapolations of the G. H. Mount et al. (1977) experimental values. The more recent A. Y. T. Lee et al. (2001) measurements find that methane's cross section sharply decreases with increasing wavelength to 4.5×10^{-24} cm^2 molecule^{-1} at 152 nm, suggesting the cross section becomes even more negligible at longer wavelengths. A. Y. T. Lee et al. (2001) also argued that G. H. Mount et al. (1977) over-estimated the CH_4 cross section for $\sim 150 < \lambda < 160$ nm because the G. H. Mount et al. (1977) experiments contained impurities (i.e., their samples contained trace amounts of C_2H_6, CO_2, etc.). Therefore, PHIDRATES likely over-predicts the CH_4 cross section for $\lambda > 150$ nm. When we use the PHIDRATES CH_4 photolysis cross sections, our model predicts ~ 1 ppm C_2H_6 at 10^{-2}, in agreement with $\sim 10^{-2}$ bar observations. While our nominal Jupiter model (Figure 9) underpredicts C_2H_6 near 10^{-2} bars, it uses the most up-to-date methane photolysis cross sections and quantum yields (A. N. Heays et al. 2017; A. Y. T. Lee et al. 2001; B. Gans et al. 2011). We leave a full reconciliation of our code with Jupiter's C_2H_6 profile to future work.

The main hydrocarbons, including C_2H_6, C_2H_4, and C_2H_2, are produced by similar pathways to those in Titan's atmosphere (Section 3.4.1). However, unlike Titan, insignificant HCN is created photochemically in Jupiter's atmosphere because there is little available atomic nitrogen (J. I. Moses et al. 2010). N_2 photolysis is ineffective at delivering N because H_2 absorbs and scatters most of the 80–100 nm photons needed to split N_2. NH_3 sourced from the deep atmosphere cannot supply N because ammonia condenses at 10^{-1} bar as it is mixes upward.

Ground-based telescopes have measured ~ 1 ppb CO near 6 bars (B. Bézard et al. 2002). Our model explains this CO concentration with quenching in the deep atmosphere. For pressures $\gtrsim 500$ bar, the atmosphere is hot (> 1000 K), and fast reactions enforce a chemical equilibrium composition. As gases mix upward to lower pressures and temperatures, reactions slow, ultimately causing an equilibrium to disequilibrium transition (i.e., quenching). We find that the reactions linking CO to CH_4 quench near 500 bars, with a rate limiting step of

$CH_3OH + M \rightarrow CH_3 + OH + M$ (Equation 15 in C. Visscher & J. I. Moses (2011)). Researchers have tried to use the observed 1 ppb CO in Jupiter's troposphere, in conjunction with kinetics quenching models like `Photochem`, to estimate the deep-atmosphere O/H ratio because CO reduction depends on H_2O (C. Visscher & J. I. Moses 2011; C. Visscher et al. 2010; T. Cavalié et al. 2023). However, CO quenching also depends on the uncertain deep-atmosphere mixing coefficient (i.e., K_{zz}), so there remains considerable uncertainty in Jupiter's O/H ratio (e.g., O/H = 0.1–0.8 × solar; T. Cavalié et al. 2023).

3.5.2. *Climate*

The climate model in Photochem does not have opacities designed for gas-giant atmospheres like Jupiter's. Most of our k-distributions assume air or self-broadening instead of He/H_2 broadening. Also, we currently do not include species like TiO, VO, or FeH that can be important opacity sources at high pressures and temperatures (see Table 2, 3 and 4 for our included opacities). With these caveats, we regardless apply our climate code to Jupiter's atmosphere to see if our limited set of opacities can capture Jupiter's temperature profile and bond albedo. We use the gas concentrations from our photochemical simulations of the planet (Figure 9a) and include a 7.485 W m^{-2} interior heat flow (i.e., a 107 K intrinsic temperature; L. Li et al. 2018). Our climate simulation does not include any clouds.

Our model (black line in Figure 9b) broadly reproduces the A. Seiff et al. (1998) upper atmosphere temperature profile ($P \lesssim 1$ bar) based on Galileo spacecraft observations. Like in Titan's stratosphere, Jupiter's upper atmosphere temperature is largely determined by the balance of heating when CH_4 absorbs sunlight, and cooling from CH_4, C_2H_6 and C_2H_4 infrared emission. The simulation has a bond albedo of 0.39, in general agreement with observed values between 0.34 and 0.5 (L. Li et al. 2018). In the deep atmosphere ($P \gtrsim 10$ bar), where Jupiter's temperature has not been measured, our model predicts the atmosphere is convective, and has a P-T profile that follows a dry He/H_2 adiabat.

Despite our incomplete set of opacities, the Figure 9b simulation broadly capture's Jupiter's expected P-T profile because of the planet's large interior heat flow. In our model, Jupiter's heat flow drives convection throughout the deep atmosphere even though we underestimate its opacity. For a gas-rich planet with a lower interior heat flow (e.g., K2-18b; N. F. Wogan et al. 2024), our limited set of absorbers should under predict the deep atmosphere temperature because the model would under estimate its opacity. To reliably use the climate model in `Photochem` for gas-rich planets, future work should include the relevant deep-atmosphere absorbers (LiCl, FeH, Na, MgH, etc.).

3.6. *WASP-39b*

The final planet that we consider is the hot Jupiter exoplanet WASP-39b. WASP-39b has roughly the mass of Saturn (0.28 $M_{\rm Jup}$), Jupiter's radius (1.28 $R_{\rm Jup}$), orbits a Sun-like star, and receives ∼ 260 times Earth's bolometric radiation (zero bond albedo T_{eq} = 1116 K; L. Mancini et al. 2018). The planet was one of the first observed by the James Webb Space Telescope with transmission spectroscopy. The data revealed a ∼ 10× solar metallicity atmosphere containing H_2O, CO_2, CO, and SO_2 (e.g., Z. Rustamkulov et al. 2023). The SO_2 is generated photochemically and was anticipated by chemical models prior to the launch of JWST (K. Zahnle et al. 2016). More recently, S.-M. Tsai et al. (2023) applied four separate photochemical codes to WASP-39b (`VULCAN`, `ARGO`, `KINETICS`, and `ATMO`) showing that the observed SO_2 abundance is consistent with model predictions. Given that WASP-39b's atmosphere has been studied with a wide range of photochemical codes, it is an ideal hot Jupiter benchmark for `Photochem`.

We conduct two simulations with `Photochem` and one with the `VULCAN` code. For all models we use the S.-M. Tsai et al. (2023) setup for the evening terminator of WASP-39b. Specifically, we use their P-T profile (Figure 13), eddy diffusion coefficient (Figure 13), incident UV spectrum, a 83 degree solar zenith angle, and a 10 times solar metallicity assuming the K. Lodders (2019) composition for the Sun. Our first simulation, shown in Figure 10a, uses `Photochem` with the same chemical network used for the Solar System planets. We predict a peak ∼ 20 ppm SO_2 abundance at 3×10^{-5} bar, a result consistent with the four photochemical calculations in S.-M. Tsai et al. (2023) (see their Figure 1b). Also, other relevant sulfur species, like H_2S, S, S_2 and SO match the S.-M. Tsai et al. (2023) ensemble of calculations. Like past work (K. Zahnle et al. 2016; S.-M. Tsai et al. 2023), we find that SO_2 (and H_2) is made when H_2S is oxidized by H_2O, mediated by ∼ 6 reactions that include water vapor photolysis (e.g., see Equation 1 in S.-M. Tsai et al. (2023)).

As a further benchmark, Figure 10b shows two additional models of WASP-39b: one with `Photochem` and other with `VULCAN`. Both calculations use the `VULCAN` thermodynamics, photolysis cross sections and the same chemical network used by `VULCAN` in S.-M. Tsai et al. (2023) (i.e., their "SNCHO_photo_network"). The `Photochem` software can convert `VULCAN` chemical networks to the `Photochem` format, making comparisons like Figure 10b straightforward. Given very similar in-

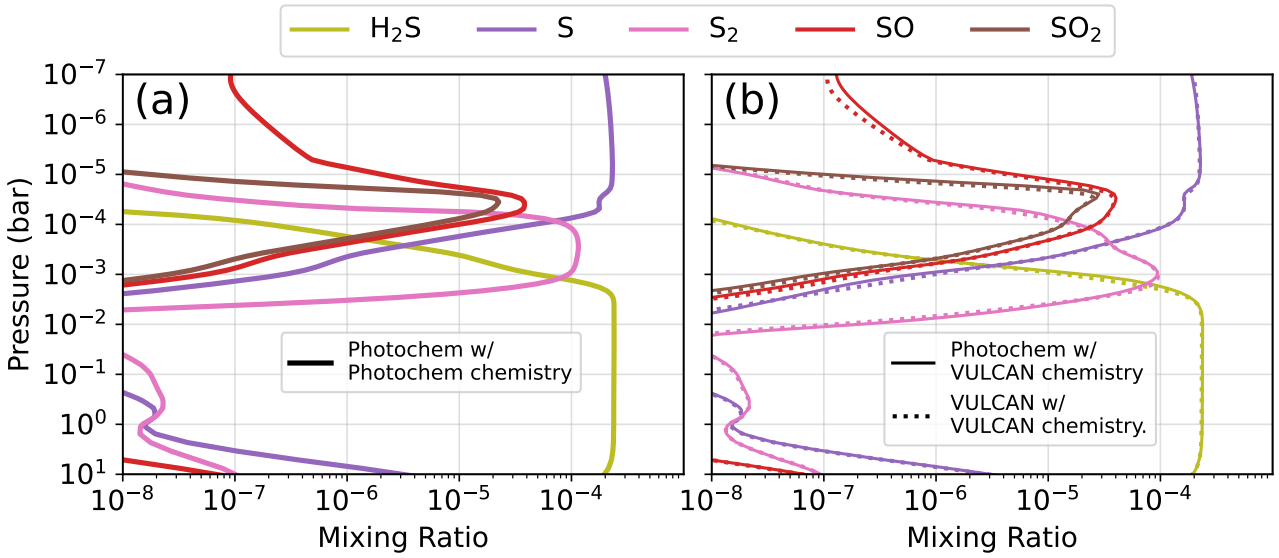

Figure 10. Photochemical simulations of WASP-39b's atmosphere at the evening terminator. (a) A model using `Photochem` with our nominal chemical network (Section 2.2.2). (b) Calculations with `Photochem` (thin solid lines) and `VULCAN` (dotted lines) where both codes use a `VULCAN` chemical network, photolysis cross sections, and thermodynamics. With our nominal chemistry `Photochem` reproduces the observed SO_2 in WASP-39b's atmosphere (S.-M. Tsai et al. 2023), and `Photochem` and `VULCAN` predict a very similar atmospheric composition for the same inputs.

puts, we find excellent agreement between `Photochem` and `VULCAN`. Some minor differences are expected (e.g., SO near 10^{-7} bar), because the calculations do not use the same Rayleigh scattering cross sections or molecular diffusion coefficients. Overall, the model consistency validates the numerical schemes in both `Photochem` and `VULCAN`.

4. DISCUSSION

4.1. *The Data and Modeling Needed to Better Understand Venus*

In our tour of the Solar System, our photochemical simulations of Earth, Mars, Titan and Jupiter predict compositions within a factor of several of observations in most cases. In contrast, Venus has the some glaring model-data discrepancies, mainly for sulfur species like OCS, S_3, S_4 and SO_2. Here we discuss the new reaction rates, opacities, and modeling approaches that would improve our understanding of the planet.

The reason why `Photochem` does not reproduce Venus observed OCS, S_3 and S_4 abundances is because these sulfur species and other relevant molecules have poorly characterized kinetics. One example is S_3 and S_4 photolysis, which is important in our Figure 2 simulations. The photolysis cross sections of both species have only sparse and controversial measurements (R. I. Billmers & A. L. Smith 1991; R. Steudel 2003). Another example is the reaction $CO + S_3 \leftrightarrow S_2 + OCS$, which is the most important production and destruction mechanism for OCS and S_3 in the deep atmosphere of our model. We use the rate constant $k = 10^{-11} \exp(-10,000/T)$ which is based on V. A. Krasnopolsky (2007) and V. A. Krasnopolsky (2013), but they instead adopt a higher activation energy of 20,000 K. There are no laboratory measurements or ab initio calculations for this reaction. V. A. Krasnopolsky (2007) chose the rate constant by considering the analogous reactions $CO + NO_2$ and $CO + SO_2$. A number of other rate constants in our network that are important to sulfur in Venus's deep atmosphere are also, at best, educated guesses. Improved simulations of Venus' sulfur chemistry requires new rate measurements or first-principle estimates for these uncertain reactions.

`Photochem` also does not capture the SO_2 depletion above $\sim$ 50 km. As noted in Section 3.1.1, one hypothesis has SO_2 dissolving in H_2SO_4 cloud droplets, a process we do not account for. P. B. Rimmer et al. (2021) used 1-D photochemical models to show that this is perhaps a plausible explanation for Venus' SO_2 depletion. Following P. B. Rimmer et al. (2021), L. Dai et al. (2024) also used droplet chemistry in a separate photochemical model to match the observed SO_2 profile. Resolving this mystery would be challenging with only modeling and lab experiments. Spacecraft probes like DAVINCI (J. B. Garvin et al. 2022) are likely needed to understand the role of Venus's clouds, if any, in sequestering SO_2.

No previous 1-D photochemical simulation of Venus's atmosphere from the surface to $\sim$ 110 km (L. Dai et al. 2024; C. J. Bierson & X. Zhang 2020; F. Wunderlich

et al. 2023; P. B. Rimmer et al. 2021) used thermodynamics to reverse all chemical reactions. The P. B. Rimmer et al. (2021) model comes closest, which reverses all but a handful of reactions using the principle of microscopic reversibility (i.e., using Gibbs free energies). P. B. Rimmer et al. (2021) perhaps omitted several reversals because they involve species with uncertain thermodynamics. L. Dai et al. (2024), C. J. Bierson & X. Zhang (2020) and F. Wunderlich et al. (2023) reversed many (but not all) reactions manually by specifying independent forward and reverse rate constants. The danger of reversing only selected reactions, or choosing forward and reverse rates independently from the literature, is that it can lead to a chemical network that is thermodynamically inconsistent (e.g., Chapter 9 of R. J. Kee et al. 2003). To avoid this issue, our nominal model in Figure 2 reverses all reactions with thermodynamics, and we argue that future models of Venus should do the same.

Additionally, as discussed in Section 3.1.2, photochemical models should take care when fixing gases at Venus's surface. Fixed surface abundances imply surface sources or sinks that may not be justified by a geologic process like volcanism. In the same vein, fixing a gas concentration throughout the atmospheric column, as has been done previously (L. Dai et al. 2024; C. J. Bierson & X. Zhang 2020; F. Wunderlich et al. 2023), is unphysical because it breaks mass conservation. Conservation of mass is important because it is the reason why sulfuric acid cloud formation by itself cannot explain the SO_2 depletion above Venus's clouds (Reaction 10, P. B. Rimmer et al. 2021). In our model, we do not fix any gas throughout the atmospheric column. We opt instead to impose zero-flux surface boundary conditions for all molecules. The zero-flux assumption at Venus' surface is equivalent to assuming that atmosphere-surface interactions are not currently important for Venus' today. To be clear, our model is not an argument against surface gas deposition (e.g., T. Constantinou et al. 2025) or the observational evidence for volcanism on modern Venus (e.g., J. Filiberto et al. 2020). Instead, our modeling approach contends that these surface processes do not substantially impact Venus' steady-state atmospheric composition today.

Through our climate simulations (Section 3.1.2), we found that Venus's energy balance is sensitive to the CO_2-CO_2 CIA opacity, even for NIR wavelengths ($\lambda < 2.5$ μm) because the surface emits strongly in the NIR. Previous work has also pointed out the importance of the CO_2 continuum to Venus's net thermal flux (e.g., Y. J. Lee et al. 2016). Further laboratory measurements of CIA opacity ($\lambda < 2.5$ μm for $400 < T < 750$ K) would likely improve our understanding of the planet's climate and Venus-like exoplanets.

4.2. *Clouds Are Hard to Predict and Are Important in Many Solar System Climates*

Although `Photochem` predicts the existence of clouds and hazes, it does not predict them accurately enough to reproduce the climates of Venus, Earth, Mars and Titan. To adequately simulate Venus's and Titan's P-T profile we had to replace the sulfuric acid and hydrocarbon hazes calculated by the model with cloud/haze optical properties derived from spacecraft and ground based observations (Section 3.1.2 and 3.4.2). For Mars, we had to prescribe observed dust aerosol densities and radii to model the planet's climate, because `Photochem` does not have a scheme for predicting atmospheric dust (Section 3.3.2). In our climate model of Earth, we parameterized water clouds with an increased surface albedo (Section 3.2.2).

This shortcoming motivates an improved treatment of aerosols in future versions of `Photochem`. The current method in the photochemical module is crude: particles form with a prescribed particle radius, then fall until they evaporate or leave the bottom of the model domain. One benefit of this parameterization is that it conserves mass. A better scheme would include more aerosol microphysics. One option is to adopt a modification of the A. S. Ackerman & M. S. Marley (2001) approach, which has previously been used by J. D. Windsor et al. (2023) to model water clouds with the `Atmos` climate code. We leave this update to future work. For now, the cloud and haze densities predicted by `Photochem` should be treated with caution when using them to predict a planet's climate.

4.3. *Simulating Atmospheres With a Self-Consistent Chemistry and Climate*

To benchmark `Photochem` against Solar System atmospheres, Section 3 does not fully couple the photochemical and climate models to compute self-consistent composition and temperature profiles. As described in Section 2.5, we choose to do fairly independent photochemical and climate simulations because they are easier to interpret when there are discrepancies between the model and observations.

However, self-consistent simulations are possible in `Photochem` by iterating between the photochemical and climate models using the approach described in G. Arney et al. (2016). In brief, we first compute an estimated climate from the atmosphere's bulk constituents. Next, we feed the resulting P-T profile into the photochemical model and compute a steady-state composition. Then, using the output composition from the

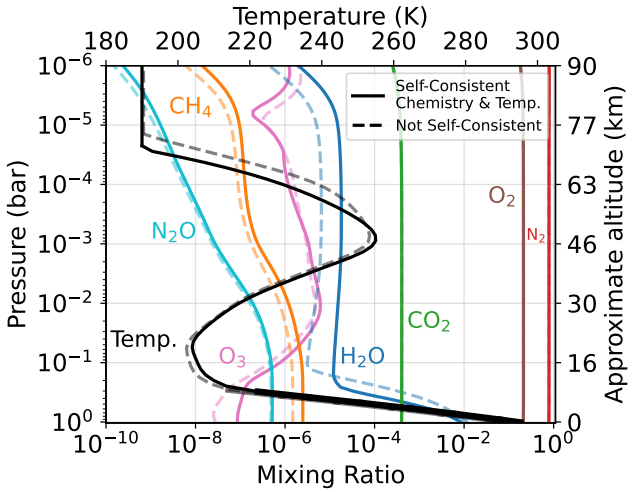

Figure 11. A self-consistent photochemical-climate simulation of the modern Earth (solid lines) compared to photochemical and climate simulations described in Section 3.2 that are not self-consistent (dashed lines). Temperature (black lines) are referenced to the top axis, and mixing ratios (colored lines) are referenced to the bottom axis.

photochemical model, we compute a new P-T profile. We iterate back and forth in this manner until the temperature at all altitudes ceases to change to some tolerance (e.g., < 1 K). To illustrate this capability, Figure 11 shows a self-consistent simulation of Earth (solid lines) with the same model setup and boundary conditions described in Section 3.2. Figure 11 also plots the Figure 4 and 5 models that are not self-consistent (dashed lines). The self-consistent model has an altered tropospheric H_2O concentration given that water vapor on Earth is largely controlled by its saturation vapor pressure (which depends on temperature). The different H_2O profile changes photolytic OH production, and OH impacts the concentration of many atmospheric constituents like O_3 and CH_4 (Section 3.2.1).

Whether the complexity of a self-consistent simulation is justified depends on the problem. For example, self-consistent simulations were warranted in T. Kozakis et al. (2022) because the objective was to understand the feedback between ozone chemistry and stratospheric temperature and the resulting impact on an Earth-like planet's emission spectrum. On the other hand, decoupled models are a more reasonable approach to simulating the photochemistry of the exoplanet K2-18b as a habitable ocean world (N. F. Wogan et al. 2024), because a habitable climate on such a planet is uncertain and perhaps not feasible (N. F. Wogan et al. 2024; H. Innes et al. 2023; J. Leconte et al. 2024).

4.4. *Comparison With the VULCAN 1-D Photochemical Model*

Here, we compare `Photochem` to `VULCAN` which is perhaps the most widely used open-source 1-D photochemical model for interpreting JWST observations. Note that Section 2.1 already compares `Photochem` to the open-source `Atmos` photochemical model for temperate rocky planets. There are several closed-source photochemical models, like `ARGO` and `KINETICS` (P. B. Rimmer & C. Helling 2016; M. Allen et al. 1981), but we do not address them here because they are hard to compare to without the source code.

`VULCAN` was first published by S.-M. Tsai et al. (2017) as a kinetics/diffusion model without photolysis reactions and was later updated by S.-M. Tsai et al. (2021) to include photons. The model was initially designed for warm gas giants and has since been adapted to rocky planets. `Photochem` had the opposite trajectory: N. F. Wogan et al. (2023) first used `Photochem` to model the early Earth atmosphere, and later N. F. Wogan et al. (2024) modified the code for gas giants.

`Photochem` and `VULCAN` (the version used in S.-M. Tsai et al. (2023)) differ in their approaches to solving the photochemical equations. For example, at each timestep, `VULCAN` re-normalizes gas number densities to maintain a hydrostatic atmosphere. This renormalization means `VULCAN` does not conserve mass. In contrast, `Photochem` conserves mass and maintains a hydrostatic atmosphere by incorporating the hydrostatic equation in the expressions for eddy and molecular diffusion (Appendix A.5 and A.6). Another difference is that `VULCAN` uses a centered finite difference scheme to discretize vertical transport from molecular diffusion. As detailed in Section 2.2.1, `Photochem` instead uses an upwind scheme for molecular diffusion to maintain numerical stability. Regardless of these differences, for the same inputs, we find that `VULCAN` and `Photochem` produce nearly identical results for our hot Jupiter WASP-39b test case (Figure 10b).

There are also differences between `VULCAN` and `Photochem`'s chemical networks and photolysis cross sections. To build both networks, chemical reaction rates were largely sourced from the NIST Kinetic Database, although some chemistry is poorly understood and not listed by NIST (e.g., Venus sulfur chemistry), so the two networks have discrepancies (Figure 10). We believe it is valuable to apply both sets of chemical reactions to the same problem (i.e., interpreting a JWST exoplanet spectrum), because the degree to which the results differ should give a sense of the uncertainty in the models attributable to chemical kinetics.

Photochem is generally faster than the version of VULCAN used in S.-M. Tsai et al. (2023). Photochem is largely written in compiled Fortran (with a Python interface), while VULCAN is currently written in pure Python. In the Figure 10b model of WASP-39b, where both models use nearly the exact same inputs, Photochem took 399 seconds for 3367 integration steps (8.4 steps/second) to reach a steady-state while VULCAN took 972 seconds over 4475 steps (4.6 steps/second). In this scenario, Photochem is about a factor of ~ 2 faster when considering integration steps per second.

There are some other practical difference that affect usage. Photochem is a standalone Python package that can be installed with the Conda package manager, then imported using standard Python syntax. Also, Photochem can be used in Python scripts or interactively in Jupyter Notebooks. In contrast, VULCAN cannot be installed and imported as a standard Python package or easily used in a Jupyter Notebook. To use the code, you must download the VULCAN repository from GitHub, then run the model's "driver" script.

4.5. *Other Open-Source 1-D Climate Models for Rocky Planets and A Benchmark With HELIOS*

The climate model in Photochem is one of relatively few open-source 1-D codes designed for rocky planets. Other examples include Atmos, Exo_k, and HELIOS (J. Leconte 2021; F. Selsis et al. 2023; M. Malik et al. 2017, 2019b,a). We consider the climate model in Photochem to be an updated version of the one in Atmos (Section 2.1). Exo_k is a Python based package that was initially designed to manage gas opacities (J. Leconte 2021), but now includes a 1-D climate module (F. Selsis et al. 2023). Exo_k has many similar features to Photochem, such as its ability to consider an arbitrary number of condensibles and their impact on the lapse rate. We anticipate that the two codes will be benchmarked against each other as a part of a CUISINES model inter-comparison (L. E. Sohl et al. 2024). HELIOS version 3.1 can simulate both gas giants and rocky planet atmospheres, although it has a limited ability to treat moist convection. Recently, HELIOS has been a popular model used by the community to evaluate JWST emission observations of warm rocky planets orbiting M stars (e.g., J. Ih et al. 2023; Q. Xue et al. 2024; M. Fortune et al. 2025). HELIOS is unique because it makes use of graphics processing units (GPUs) whereas Photochem and many other climate models use CPUs. GPUs are generally considered to be faster than CPUs for highly parallel problems like radiative transfer where calculations are wavelength independent.

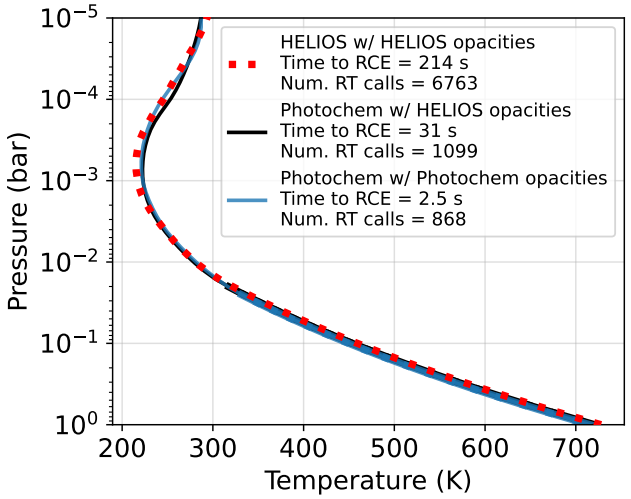

Figure 12. A benchmark between the climate model in Photochem and the HELIOS GPU code for a CO_2-H_2O atmosphere (50% each) on an Earth-sized planet orbiting the Sun at 0.5 AU. Three cases are shown: HELIOS with HELIOS k-distributions (red dotted line), Photochem with HELIOS k-distributions (black line), and Photochem with Photochem k-distributions (blue line). See text for more benchmark details. The acronyms "RCE" and "RT" in the legend stand for "radiative-convective equilibrium" and "radiative transfer", respectively. Both codes produce very similar P-T profiles, and Photochem's root-finding approach (Section 2.3) reaches RCE in $\sim 6\times$ fewer radiative transfer calls.

Here, we conduct a benchmark between HELIOS version 3.1 and Photochem to gauge possible performance differences between a GPU and CPU code. The test computes radiative-convective equilibrium for a planet with Earth's mass, Earth's radius, a 1 bar atmosphere composed of 50% CO_2 and H_2O, set 0.5 AU from the Sun. We consider three cases: HELIOS with HELIOS k-distributions, Photochem with HELIOS k-distributions, and Photochem with Photochem k-distributions (Table 2). For all scenarios, the code only uses CO_2 and H_2O k-distributions and omits all other opacity sources (i.e., no Rayleigh scattering or CIA). The tests that use HELIOS's k-distributions, adopt the k-tables shipped with version 3.1 of the model (385 wavelength bins each with twenty k-terms). Both codes use the same "resort rebin" method to mix k-distributions (D. S. Amundsen et al. 2017). We ignore condensation and use a dry adiabat. We use HELIOS's adaptive time stepping scheme and assume an initially isothermal 500 K P-T profile.

Figure 12 shows that the predicted P-T profiles are very similar. With HELIOS's opacities, Photochem took 31 seconds and 1099 radiative transfer calculations to reach radiative-convective equilibrium using 8 cores of a MacBook M1 Pro. HELIOS took 214 seconds and 6763 radiative transfer calls using an NVIDIA Tesla V100 16

GB GPU. Photochem's root finding approach (Section 2.3) speeds convergence with $\sim 6\times$ fewer radiative transfer calls and an overall runtime that is $\sim 7\times$ shorter (for this hardware and these opacities). In terms of radiative transfer calls per second, HELIOS and Photochem exhibit similar performance for the same opacities. We suspect that HELIOS's GPU radiative transfer is not faster because the HELIOS k-tables are at fairly low resolution ($R \approx 50$), so the problem may not be parallel enough to benefit significantly from GPUs.

All climate calculations in Section 3 use even lower resolution k-tables ($2 < R < 60$, with an average $R \approx 15$) and a smaller number of k-terms (eight) than adopted by HELIOS's opacities. When we repeat the climate benchmark with Photochem's lower resolution opacities (Table 2), Photochem iterates to nearly the same P-T profile in just 2.5 seconds on the same hardware (blue line in Figure 12), $86\times$ faster than the HELIOS calculation. We were unable to test our low resolution opacities with HELIOS because the latter is limited to k-distributions with twenty terms. This result illustrates that the $R \approx 50$ and 20 term HELIOS k-distributions are excessive for this test case. Adopting Photochem with its nominal opacities for problems similar to this benchmark, such as modeling a warm rocky exoplanet observed by JWST, should be ~ 10 to $100\times$ faster than using HELIOS (with its nominal opacities) without sacrificing meaningful accuracy.

5. CONCLUSIONS

To interpret spectroscopic observations of exoplanet atmospheres, the community needs models of atmospheric chemistry and climate that are applicable to the widest possible diversity of planetary atmospheres. To this end, we present the open-source 1-D photochemical and climate model Photochem. To demonstrate the model's generality, we benchmark it against the observed compositions and climates of Venus, Earth, Mars, Titan and Jupiter using a single set of kinetics, thermodynamics and opacities. We also model the chemistry of the hot-Jupiter WASP-39b. All of these tests are open-source and fully reproducible to best support future model development (https://doi.org/10.5281/zenodo.16509802). From our tour of the Solar System and one exoplanet our conclusions are as follows:

- To first order, Photochem predicts gas concentrations and P-T profiles that are broadly consistent with observations of five Solar System atmospheres (Venus, Earth, Mars, Titan and Jupiter). The code also reproduces the photochemical SO_2 observed by JWST in WASP-39b's atmosphere.
- Of the Solar System worlds, the most egregious model-data discrepancies involve sulfur species in Venus's atmosphere, motivating an improved understanding of sulfur's chemical kinetics. We also urge that future Venus photochemical models use networks that are thermodynamically self-consistent and explicitly conserve mass (Section 4.1). Furthermore, near-infrared measurements of CO_2-CO_2 CIA opacity would improve our understanding of Venus' climate.
- Photochem predicts clouds and hazes that do not yet accurately reproduce the climates of planets, motivating an improved treatment of aerosols in future versions of the model. We reproduced these climates by prescribing observed cloud or haze optical properties.
- We benchmark the photochemical model in Photochem against the VULCAN code. We find that the two models are in excellent agreement for the same inputs, and we find that Photochem is about twice as fast (Section 3.6).
- We also found that our climate model in Photochem agrees with the HELIOS GPU-accelerated climate model for the same problem. In our test case, Photochem's root-finding approach for computing radiative-convective equilibrium takes $\sim 6\times$ less radiative-transfer calls than HELIOS's time-integration scheme. Radiative transfer calculations by the two codes have comparable run times on the hardware we tested, suggesting that the correlated-k radiative transfer in our benchmark case is not sufficiently parallel to benefit from GPUs.

Overall, Photochem provides a general description of atmospheric chemistry and physics that captures a wide range of planetary atmospheres. We conclude that Photochem is a good option for future study of exoplanets.

ACKNOWLEDGMENTS

We thank our two reviewers who improved the quality of this article. Conversations with David Crisp, Sonny Harman, Mark Claire, Sandra Bastelberger, Ravi Kopparapu, Andrew Lincowski, Sukrit Ranjan, and Shangmin Tsai benefited the development of Photochem. NFW was supported by the NASA Postdoctoral Program. N.E.B acknowledges support from NASA'S Interdisciplinary Consortia for Astrobiology Research

(NNH19ZDA001N-ICAR) and JWST Theory Grant JWST-AR-02232- 001-A. VSM, ETW, TDR, and DCC acknowledge support from the Virtual Planetary Laboratory, a member of the NASA Nexus for Exoplanet System Science (NExSS), funded via the NASA Astrobiology Program grant Nos. 80NSSC23K1398 and 80NSSC18K0829, respectively. DCC and JKT also acknowledge support from the Alfred P. Sloan Foundation under Grant No. 2025-25204.

AUTHOR CONTRIBUTIONS

NFW wrote the original paper draft, performed the calculations, wrote and manages the `Photochem` code. KZ built the reaction and thermodynamic database. NEB and KZ provided numerical and coding advice to NFW as he wrote and developed `Photochem`. All authors contributed to writing the manuscript.

APPENDIX

A. THE PHOTOCHEMICAL EQUATIONS

In this Appendix, we derive the fundamental equations solved in the photochemistry module of `Photochem`. Some of our derivation overlaps with Appendix C.1 in N. F. Wogan et al. (2023), however, we believe that the repetition is justified because some of our assumptions have changed, and the derivation here is more complete than the one in N. F. Wogan et al. (2023).

A.1. *The Continuity Equations*

We begin our derivation of the governing photochemical equations with a statement of the conservation of molecules. Such statements of conservation are often called continuity equations.

$$\frac{\partial n_i}{\partial t} = -\frac{\partial \Phi_i}{\partial z} + \sigma_i \tag{A1}$$

Here, n_i is the number density of molecule i in units of molecules cm^{-3}; t is time in seconds; z is altitude in cm; Φ_i is the flux of species i in units of molecules cm^{-2} s^{-1}; and σ_i represents the sources and sinks of species i in units of molecules cm^{-3} s^{-1}. Equation (A1) states that a molecule's concentration changes over time at a point in space in response to molecules entering or leaving the space (i.e., Φ_i) and the production or destruction of molecules (i.e., σ_i). This version of the continuity equation is one-dimensional and assumes that species concentrations change only in the vertical (z) direction.

The flux of a gas species i ($\Phi_{i,\text{gas}}$) is determined by eddy and molecular diffusion. The flux of particles ($\Phi_{i,\text{particle}}$) is approximated by how rapidly particles fall through the atmosphere.

$$\Phi_{i,\text{gas}} = \Phi_{i,\text{eddy}} + \Phi_{i,\text{molecular}} \tag{A2}$$

$$\Phi_{i,\text{particle}} = \Phi_{i,\text{fall}} \tag{A3}$$

Here, $\Phi_{i,\text{eddy}}$, $\Phi_{i,\text{molecular}}$ and $\Phi_{i,\text{fall}}$ are approximated by

$$\Phi_{i,\text{eddy}} = -K_{zz} n_i \left(\frac{1}{n_i}\frac{\partial n_i}{\partial z} + \frac{1}{H_a} + \frac{1}{T}\frac{\partial T}{\partial z} \right) \tag{A4}$$

$$\Phi_{i,\text{molecular}} = -D_i n_i \left(\frac{1}{n_i}\frac{\partial n_i}{\partial z} + \frac{1}{H_i} + \frac{1}{T}\frac{\partial T}{\partial z} \right) \tag{A5}$$

$$\Phi_{i,\text{fall}} = -w_i n_i \tag{A6}$$

Here, K_{zz} is the eddy diffusion coefficient in cm^2 s^{-1}; H_a is the scale height in cm; T is temperature in Kelvin; D_i is the molecular diffusion coefficient of species i in cm^2 s^{-1}; and H_i is scale height of species i in cm. Appendix A.5 derives Equation (A4) while Appendix A.6 derives Equation (A5) starting with the general molecular diffusion equation. Equations (A4) and (A5) assume the atmosphere is an ideal gas at hydrostatic equilibrium. Furthermore,

Equation (A5) assumes that the diffusing gas is a minor atmospheric constituent and ignores thermal diffusion. In Equation (A6), w_i is the fall velocity of a particle, which can be estimated with Stokes' law (Appendix A.7).

In a real atmosphere, particles are also transported by turbulent mixing (i.e., parameterized with eddy diffusion), but we choose to ignore this effect because we do not include detailed microphysics. Without microphysics, we have found that particle turbulent mixing can lead to undesirable solutions. For example, a large eddy diffusion coefficient can loft small particles in a way that eliminates a cold trap. While such a process can sometimes occur in a real atmosphere, a credible model of it would require microphysics that we do not account for.

We assume that the sources and sinks of a molecule or particle i are chemical production (P_i), chemical loss (L_i), rainout in droplets of liquid ($R_{i,\text{rainout}}$), and condensation or evaporation (E_i):

$$\sigma_i = P_i - L_i - R_{i,\text{rainout}} + E_i \tag{A7}$$

`Photochem` computes chemical production and loss using the elementary, three-body, and photolysis reactions detailed in Section 2.2.2. We model rainout following the H. Georgii & F. X. Meixner (1980) parameterization with solubility data from R. Sander (2015). Appendix A.4 describes our treatment of condensation and evaporation.

To facilitate a finite volume discretization (Appendix A.2), below, we reorganize Equation (A2) into advective and diffusive terms:

$$\Phi_{i,\text{gas}} = -\alpha_i \frac{\partial n_i}{\partial z} - \beta n_i - \gamma_i n_i \tag{A8}$$

$$\alpha_i = K_{zz} + D_i \tag{A9}$$

$$\beta = K_{zz}\left(\frac{1}{H_a} + \frac{1}{T}\frac{\partial T}{\partial z}\right) \tag{A10}$$

$$\gamma_i = D_i\left(\frac{1}{H_i} + \frac{1}{T}\frac{\partial T}{\partial z}\right) \tag{A11}$$

The 1-D continuity equation (Equation (A1)) and corresponding fluxes (Equations (A8) and (A3)) and source terms (Equation (A7)) are a system of partial differential equations (PDEs) describing how the number density (n_i) of each chemical species i changes over altitude and time. In the following Appendix subsection, we discretize this system of PDEs using a finite volume method.

A.2. *Finite Volume Discretization*

We use the finite volume method to discretize Equation (A1) allowing an approximate numerical solution. The finite volume method divides the spatial domain (z) into grid cells, or finite volumes, in order to approximate the cell-averaged value of a species number density, n_i. Approximations to the cell-averaged value of n_i are modified over time by considering the flux of molecules through the edges of the cells, and the sources and sinks of molecules within the cell. The main advantage of this approach is that the approximation conserves molecules, which is not always the case for other PDE discretization methods (e.g., finite difference or finite element methods). Molecule conservation is valuable for understanding whether a model run has reached steady-state, or interrogating the redox fluxes into and out of an atmosphere. Below, we describe the application of the finite volume method to Equation (A1). For an in-depth understanding of the finite volume method, see R. J. LeVeque et al. (2002).

Consider an atmosphere that has been vertically divided into m grid-cell (i.e. finite volumes) of thickness Δz^j. The superscript j refers to a grid cell (j does not refer to a power), where $j = l$ is the lowest altitude grid-cell $j = m$ highest grid-cell. z^j is the altitude at the center of grid-cell j, such that the upper and lower edges of the cell are given by $z^{j+1/2} = z^j + \frac{\Delta z^j}{2}$ and $z^{j-1/2} = z^j - \frac{\Delta z^j}{2}$, respectfully.

Consider a single grid cell between altitudes $z = z^{j-1/2}$ and $z = z^{j+1/2}$. Integrating Equation (A1) from the bottom to the top of the grid cell gives

$$\frac{\partial}{\partial t}\int_{z^{j-1/2}}^{z^{j+1/2}} n_i dz = -(\Phi_i(z^{j+1/2}) - \Phi_i(z^{j-1/2})) + \int_{z^{j-1/2}}^{z^{j+1/2}} \sigma_i dz \tag{A12}$$

The average value of n_i and σ_i between $z^{j-1/2}$ and $z^{j+1/2}$ are given by the integrals

$$\overline{n_i}^j = \frac{1}{\Delta z^j} \int_{z^{j-1/2}}^{z^{j+1/2}} n_i dz \tag{A13}$$

$$\overline{\sigma_i}^j = \frac{1}{\Delta z^j} \int_{z^{j-1/2}}^{z^{j+1/2}} \sigma_i dz \tag{A14}$$

Substituting the above expressions into Equation (A12) yields

$$\frac{\partial}{\partial t}\overline{n_i}^j(t) = -\frac{\Phi_i(z^{j+1/2},t) - \Phi_i(z^{j-1/2},t)}{\Delta z^j} + \overline{\sigma_i}^j(t) \tag{A15}$$

Equation (A15) states that the average number density of species i in the j atmospheric layer ($\overline{n_i}^j$) changes over time because of the fluxes at the edges of the layer (e.g. $\Phi_i(z^{j+1/2},t)$), and the average production or loss of the species in the layer ($\overline{\sigma_i}^j$). The above formula is exact for $\overline{n_i}^j(t)$. However, now we introduce some approximations. First, we assume that $\overline{n_i}^j(t)$, $\overline{\sigma_i}^j(t)$, $\Phi_i(z^{j+1/2},t)$ and $\Phi_i(z^{j-1/2},t)$ are constant over small segments of time. Also, we approximate $\Phi_i(z^{j+1/2},t)$, $\Phi_i(z^{j-1/2},t)$ and $\overline{\sigma_i}^j(t)$ in terms of cell-averaged quantities, such as $\overline{n_i}^j$. We denote the approximate quantities in the following way

$$\begin{aligned} n_i^j &\approx \overline{n_i}^j & \Phi_i^{j+1/2} &\approx \Phi_i(z^{j+1/2},t) \\ \sigma_i^j &\approx \overline{\sigma_i}^j(t) & \Phi_i^{j-1/2} &\approx \Phi_i(z^{j-1/2},t) \end{aligned} \tag{A16}$$

Substituting the approximate quantities into Equation (A15) gives

$$\frac{\partial n_i^j}{\partial t} = -\frac{\Phi_i^{j+1/2} - \Phi_i^{j-1/2}}{\Delta z^j} + \sigma_i^j \tag{A17}$$

We now must derive expressions for the gas and particle fluxes at grid-cell edges that are accurate and stable for our problem.

A.2.1. *Gases*

The equation for gas flux (Equation (A8)) contains the γ_i advection term which can be much stronger than the diffusion term (α_i), especially high in the atmosphere when a heavy species (e.g., S_8) is transported through a light background gas (e.g., H_2). The β advection term, on the other hand, is generally small compared to the diffusion term. Therefore, for stability, we use a first-order upwind scheme for the γ_i term, and a centered scheme for the α_i and β terms. To accomplish this, we first separate Equation (A8) in the following way

$$\Phi_{i,\text{gas}} = \Phi_{i,\text{center}} + \Phi_{i,\text{upwind}} \tag{A18}$$

$$\Phi_{i,\text{center}} = -\alpha_i \frac{\partial n_i}{\partial z} - \beta n_i \tag{A19}$$

$$\Phi_{i,\text{upwind}} = -\gamma_i n_i \tag{A20}$$

Therefore, we can write Equation (A17) as

$$\frac{\partial n_{i\in\text{gas}}^j}{\partial t} = -\frac{\Phi_{i,\text{center}}^{j+1/2} - \Phi_{i,\text{center}}^{j-1/2}}{\Delta z^j} - \frac{\Phi_{i,\text{upwind}}^{j+1/2} - \Phi_{i,\text{upwind}}^{j-1/2}}{\Delta z^j} + \sigma_i^j \tag{A21}$$

Applying a centered scheme (Equation 4.10 in R. J. LeVeque et al. (2002)) to $\Phi_{i,\text{center}}$ yields:

$$\Phi_{i,\text{center}}^{j+1/2} = -\alpha_i^{j+1/2} \left(\frac{\partial n_i}{\partial z}\right)^{j+1/2} - \beta_i^{j+1/2} n_i^{j+1/2} \tag{A22}$$

$$\left(\frac{\partial n_i}{\partial z}\right)^{j+1/2} \approx \frac{n_i^{j+1} - n_i^j}{\Delta z^{j+1/2}} \tag{A23}$$

Where $\Delta z^{j+1/2} = \frac{1}{2}\Delta z^j + \frac{1}{2}\Delta z^{j+1}$. Also, $n_i^{j+1/2}$ can be estimated by linearly interpolating between the two adjacent cells.

$$n_i^{j+1/2} \approx \frac{\Delta z^j n_i^{j+1} + \Delta z^{j+1} n_i^j}{\Delta z^{j+1} + \Delta z^j}$$

Therefore,

$$\Phi_{i,\text{center}}^{j+1/2} = -\alpha^{j+1/2} \frac{n_i^{j+1} - n_i^j}{\Delta z^{j+1/2}} - \beta_i^{j+1/2} \frac{\Delta z^j n_i^{j+1} + \Delta z^{j+1} n_i^j}{\Delta z^{j+1} + \Delta z^j} \tag{A24}$$

Using a similar procedure, $\Phi_{i,\text{gas}}^{j-1/2}$ is given by

$$\Phi_{i,\text{center}}^{j-1/2} = -\alpha^{j-1/2} \frac{n_i^j - n_i^{j-1}}{\Delta z^{j-1/2}} - \beta_i^{j-1/2} \frac{\Delta z^{j-1} n_i^j + \Delta z^j n_i^{j-1}}{\Delta z^j + \Delta z^{j-1}} \tag{A25}$$

To apply a first-order upwind scheme to $\Phi_{i,\text{upwind}}$, we first recognize that γ_i is often positive, except under extreme temperature gradients, so information frequently travels from up to down in the model. Therefore, an upwind scheme approximates the advective fluxes with a forward difference

$$\frac{\Phi_{i,\text{upwind}}^{j+1/2} - \Phi_{i,\text{upwind}}^{j-1/2}}{\Delta z^j} \approx \frac{\Phi_{i,\text{upwind}}^{j+1} - \Phi_{i,\text{upwind}}^{j}}{\Delta z^j} = \frac{-\gamma_i^{j+1} n_i^{j+1} + \gamma_i^j n_i^j}{\Delta z^j} \tag{A26}$$

Substituting Equations (A24), (A25) and (A26) into Equation (A21) and re-arranging gives an expression of the form

$$\begin{aligned} \frac{\partial n_i^j}{\partial t} &= (A_i^{j,\text{upper}} + B_i^{j,\text{upper}}) n_i^{j+1} \\ &+ (A_i^{j,\text{center}} + B_i^{j,\text{center}}) n_i^j \\ &+ (A_i^{j,\text{lower}} + B_i^{j,\text{lower}}) n_i^{j-1} \\ &+ \sigma_i^j \end{aligned} \tag{A27}$$

The A and B coefficients for gases correspond to the diffusive and advective approximations to the cell-edge fluxes, respectively:

$$\begin{aligned} A_{i,\text{gas}}^{j,\text{upper}} &= \frac{\alpha_i^{j+1/2}}{\Delta z^j \Delta z^{j+1/2}} \\ A_{i,\text{gas}}^{j,\text{center}} &= -\frac{\alpha_i^{j+1/2}}{\Delta z^j \Delta z^{j+1/2}} - \frac{\alpha_i^{j-1/2}}{\Delta z^j \Delta z^{j-1/2}} \\ A_{i,\text{gas}}^{j,\text{lower}} &= \frac{\alpha_i^{j-1/2}}{\Delta z^j \Delta z^{j-1/2}} \\ B_{i,\text{gas}}^{j,\text{upper}} &= \frac{\beta_i^{j+1/2}}{\Delta z^{j+1} + \Delta z^j} + \frac{\gamma_i^{j+1}}{\Delta z^j} \\ B_{i,\text{gas}}^{j,\text{center}} &= \beta_i^{j+1/2} \frac{\Delta z^{j+1}}{\Delta z^j (\Delta z^{j+1} + \Delta z^j)} - \beta_i^{j-1/2} \frac{\Delta z^{j-1}}{\Delta z^j (\Delta z^j + \Delta z^{j-1})} - \frac{\gamma_i^j}{\Delta z^j} \\ B_{i,\text{gas}}^{j,\text{lower}} &= -\frac{\beta_i^{j-1/2}}{\Delta z^j + \Delta z^{j-1}} \end{aligned} \tag{A28}$$

The lower boundary condition is the flux through the lower edge of the lowest-altitude cell, $\Phi_i^{l-1/2} = \Phi_i^{\text{lower}}$. Similarly, the upper boundary condition is the flux through through the top edge of the highest-altitude cell, $\Phi_i^{m+1/2} = \Phi_i^{\text{upper}}$. It follows from Equation (A17) that

$$\frac{\partial n_i^l}{\partial t} = -\frac{\Phi_i^{\mathrm{l+1/2}} - \Phi_i^{\mathrm{lower}}}{\Delta z^l} + \sigma_i^l \tag{A29}$$

$$\frac{\partial n_i^m}{\partial t} = -\frac{\Phi_i^{\mathrm{upper}} - \Phi_i^{m-1/2}}{\Delta z^m} + \sigma_i^m \tag{A30}$$

Plugging in Equation (A24), (A25) and (A26) into Equation (A29) and (A30) gives the following general expression for the rate densities change at the boundaries

$$\begin{aligned}\frac{\partial n_i^l}{\partial t} &= (A_i^{l,\mathrm{upper}} + B_i^{l,\mathrm{upper}})n_i^{l+1} \\ &+ (A_i^{l,\mathrm{center}} + B_i^{l,\mathrm{center}})n_i^l \\ &+ \frac{\Phi_i^{\mathrm{lower}}}{\Delta z^l} \\ &+ \sigma_i^l\end{aligned} \qquad \begin{aligned}\frac{\partial n_i^m}{\partial t} &= (A_i^{m,\mathrm{center}} + B_i^{m,\mathrm{center}})n_i^m \\ &+ (A_i^{m,\mathrm{lower}} + B_i^{m,\mathrm{lower}})n_i^{m-1} \\ &- \frac{\Phi_i^{\mathrm{upper}}}{\Delta z^m} \\ &+ \sigma_i^m\end{aligned} \tag{A31}$$

For gases, the A and B coefficients for the lower boundary are

$$\begin{aligned}A_{i,\mathrm{gas}}^{l,\mathrm{upper}} &= \frac{\alpha_i^{l+1/2}}{\Delta z^l \Delta z^{l+1/2}} \\ A_{i,\mathrm{gas}}^{l,\mathrm{center}} &= -\frac{\alpha_i^{l+1/2}}{\Delta z^l \Delta z^{l+1/2}}\end{aligned} \qquad \begin{aligned}B_{i,\mathrm{gas}}^{l,\mathrm{upper}} &= \frac{\beta_i^{l+1/2}}{\Delta z^{l+1} + \Delta z^l} + \frac{\gamma_i^{l+1}}{\Delta z^l} \\ B_{i,\mathrm{gas}}^{l,\mathrm{center}} &= \beta_i^{l+1/2}\frac{\Delta z^{l+1}}{\Delta z^l(\Delta z^{l+1} + \Delta z^l)}\end{aligned} \tag{A32}$$

and the upper boundary,

$$\begin{aligned}A_{i,\mathrm{gas}}^{m,\mathrm{center}} &= -\frac{\alpha_i^{m-1/2}}{\Delta z^m \Delta z^{m-1/2}} \\ A_{i,\mathrm{gas}}^{m,\mathrm{lower}} &= \frac{\alpha_i^{m-1/2}}{\Delta z^m \Delta z^{m-1/2}}\end{aligned} \qquad \begin{aligned}B_{i,\mathrm{gas}}^{m,\mathrm{center}} &= -\beta_i^{m-1/2}\frac{\Delta z^{m-1}}{\Delta z^m(\Delta z^m + \Delta z^{m-1})} - \frac{\gamma_i^m}{\Delta z^m} \\ B_{i,\mathrm{gas}}^{m,\mathrm{lower}} &= -\frac{\beta_i^{m-1/2}}{\Delta z^m + \Delta z^{m-1}}\end{aligned} \tag{A33}$$

A.2.2. *Particles*

We assume particle transport is governed by the rate they fall through the atmosphere (Equation (A6)). The flux is an advection equation, so we use a first order upwind scheme for stability. Additionally, the fall velocity w_i is always positive (i.e. particles always fall downward), so an upwind scheme should approximate the advective fluxes with a forward difference. In the previous subsection, we applied the same forward upwind scheme to the γ_i advective terms for gases. Therefore, by analogy to the γ_i terms in Equation (A28), the A and B coefficients in Equation (A27) for particles are,

$$\begin{aligned}A_{i,\mathrm{particle}}^{j,\mathrm{upper}} &= 0 \\ A_{i,\mathrm{particle}}^{j,\mathrm{center}} &= 0 \\ A_{i,\mathrm{particle}}^{j,\mathrm{lower}} &= 0\end{aligned} \qquad \begin{aligned}B_{i,\mathrm{particle}}^{j,\mathrm{upper}} &= \frac{w_i^{j+1}}{\Delta z^j} \\ B_{i,\mathrm{particle}}^{j,\mathrm{center}} &= -\frac{w_i^j}{\Delta z^j} \\ B_{i,\mathrm{particle}}^{j,\mathrm{lower}} &= 0\end{aligned} \tag{A34}$$

In the same vein, all of the A coefficients in Equation (A31) for particles are zero. The B coefficients for the boundaries are

$$\begin{aligned}B_{i,\mathrm{particle}}^{l,\mathrm{upper}} &= \frac{w_i^{l+1}}{\Delta z^l} \\ B_{i,\mathrm{particle}}^{l,\mathrm{center}} &= 0\end{aligned} \qquad \begin{aligned}B_{i,\mathrm{particle}}^{m,\mathrm{center}} &= -\frac{w_i^m}{\Delta z^m} \\ B_{i,\mathrm{particle}}^{m,\mathrm{lower}} &= 0\end{aligned} \tag{A35}$$

A.3. *Solving the Finite Volume Discretization*

Equations (A27) and (A31) and the corresponding coefficients for gases and particles (Equations (A28), (A32), (A33), (A34) and (A35)) are a system of ordinary differential equations (ODEs) which are a finite volume approximation of our original system of PDEs (Equation (A1)). Section 2.2.1 describes how `Photochem` solves these equations. In brief, we evolve Equations (A27) and (A31) using the CVODE stiff ODE integrator (A. C. Hindmarsh et al. 2005). In `Photochem`, CVODE can be used to study the time-evolution of an atmosphere, or alternatively integrate the atmosphere to a steady-state composition ($dn_i^j/dt = 0$).

A.4. *Condensation and Evaporation*

`Photochem`'s scheme for condensation and evaporation accomplishes the following simple goals: Gas-phase species should be converted to particles if they are above a given relative humidity (RH), and particles should be converted to gases if the gas is below a specified RH. Another requirement is that the rate of gas-to-particle or particle-to-gas conversion is smooth such that it does not introduce excessive "stiffness" in the system of ODEs. To accomplish these objectives, `Photochem` computes the rate constant of condensation with

$$k_{\text{cond}} = \begin{cases} A_{\text{cond}} \left(\frac{K_{zz}}{H_a^2}\right) \left(\frac{2}{\pi}\right) \arctan\left(\frac{r - r_c}{S r_c}\right) & r > r_c \\ 0 & r \leq r_c \end{cases} \tag{A36}$$

Here, A_{cond} is a condensation rate coefficient of order ~ 100, r is the relative humidity, r_c is the relative humidity of condensation ($r_c \approx 1$), and S is a smoothing factor ($S \approx 0.5$). Similarly, the rate constant of evaporation is

$$k_{\text{evap}} = \begin{cases} 0 & r < r_c \\ A_{\text{evap}} \left(\frac{w_i}{H_a}\right) \left(\frac{2}{\pi}\right) \arctan\left(\frac{1/r - 1/r_c}{S/r_c}\right) & r \leq r_c \end{cases} \tag{A37}$$

Here, A_{evap} is an evaporation rate coefficient of order ~ 10. By including terms like K_{zz}/H_a^2 and w_i/H_a, the rate constants condense or evaporate a species more rapidly than the gas or particle is vertically transported. The arctan term is a sigmoid function that smoothly varies the rate constant from 0 for small relative humidity, and, for example, $A_{\text{cond}}\left(K_{zz}/H_a^2\right)$ for large relativity humidity (in the case of condensation). Using H_2O as an example, the rate gas-phase and condensed-phase H_2O are produced and destroyed from condensation and evaporation is

$$E_{i,\text{H}_2\text{O,gas}} = -n_{\text{H}_2\text{O,gas}} k_{\text{cond}} + n_{\text{H}_2\text{O,particle}} k_{\text{evap}} \tag{A38}$$

$$E_{i,\text{H}_2\text{O,particle}} = -E_{i,\text{H}_2\text{O,gas}} \tag{A39}$$

Here, $n_{\text{H}_2\text{O,gas}}$ and $n_{\text{H}_2\text{O,particle}}$ are the number density of H_2O gas and particles in molecules cm^{-3} s^{-1}, respectively.

A.5. *Eddy Diffusion*

Like many other photochemical models, `Photochem` parametrizes turbulent vertical transport with an eddy diffusion flux (e.g., Equation 5.44 in D. C. Catling & J. F. Kasting (2017)):

$$\Phi_{i,\text{eddy}} = -K_{zz} n \frac{\partial}{\partial z}\left(\frac{n_i}{n}\right) \tag{A40}$$

Here, n is the total number density. To account for eddy diffusion, we need to rewrite Equation (A40) so that there are not any partial derivatives with respect to the total number density. To accomplish this, first consider the ideal gas law and hydrostatic equation,

$$P = nkT \tag{A41}$$

$$\frac{\partial P}{\partial z} = -g\rho = \frac{-gP\bar{\mu}}{N_a k T} \tag{A42}$$

Substituting the ideal gas law in the hydrostatic equation yields

$$\frac{\partial}{\partial z}(nT) = \frac{-gn\bar{\mu}}{N_a k} \tag{A43}$$

$$n\frac{\partial T}{\partial z} + T\frac{\partial n}{\partial z} = \frac{-gn\bar{\mu}}{N_a k} \tag{A44}$$

After rearrangement and substituting the definition of scale height,

$$\frac{1}{n}\frac{\partial n}{\partial z} = -\frac{1}{H_a} - \frac{1}{T}\frac{\partial T}{\partial z} \tag{A45}$$

Now consider the following expansion using the quotient rule

$$\frac{\partial}{\partial z}\left(\frac{n_i}{n}\right) = \frac{1}{n}\frac{\partial n_i}{\partial z} - \frac{n_i}{n^2}\frac{\partial n}{\partial z} \tag{A46}$$

Substituting Equation (A45) into Equation (A46) and rearrangement gives

$$n\frac{\partial}{\partial z}\left(\frac{n_i}{n}\right) = \frac{\partial n_i}{\partial z} + \frac{n_i}{H_a} + \frac{n_i}{T}\frac{\partial T}{\partial z} \tag{A47}$$

Finally, substituting Equation (A47) into Equation (A40) yields the eddy diffusion flux that we use in `Photochem`:

$$\Phi_{i,\text{eddy}} = -K_{zz} n_i \left(\frac{1}{n_i}\frac{\partial n_i}{\partial z} + \frac{1}{H_a} + \frac{1}{T}\frac{\partial T}{\partial z}\right) \tag{A48}$$

A.6. *Molecular Diffusion*

The general molecular diffusion equation giving the relative diffusion velocity of gas i with respect to gas j in one dimension is (Equation 15.1 in P. M. Banks & G. Kockarts (2013), or Equation 14.1, 1 in S. Chapman & T. G. Cowling (1990))

$$v_i - v_j = -D_{ij}\left(\frac{n^2}{n_i n_j}\frac{\partial}{\partial z}\left(\frac{n_i}{n}\right) + \frac{\mu_j - \mu_i}{\overline{\mu}}\frac{1}{P}\frac{\partial P}{\partial z} + \frac{\alpha_{Ti}}{T}\frac{\partial T}{\partial z} - \frac{\mu_i \mu_j}{\overline{\mu} N_a k T}(a_i - a_j)\right) \tag{A49}$$

Here, a_1 and a_2 are external accelerations of each molecule from, for example, a magnetic or electric field if the molecule is an ion. We assume neutral molecules such that $a_i = a_j = 0$. We also assume that the atmosphere is an ideal gas and is in hydrostatic equilibrium:

$$\frac{\partial P}{\partial z} = -g\rho = \frac{-gP\overline{\mu}}{N_a k T} \tag{A50}$$

$$\frac{1}{P}\frac{\partial P}{\partial z} = \frac{-g\overline{\mu}}{N_a k T} = \frac{-1}{H_a} \tag{A51}$$

Substitution of $a_i = a_j = 0$ and Equation (A51) into Equation (A49) gives

$$v_i - v_j = -D_{ij}\left(\frac{n^2}{n_i n_j}\frac{\partial}{\partial z}\left(\frac{n_i}{n}\right) - \frac{\mu_j - \mu_i}{\overline{\mu}}\frac{1}{H_a} + \frac{\alpha_{Ti}}{T}\frac{\partial T}{\partial z}\right) \tag{A52}$$

We make two further approximation: We assume gas i is a small abundance compared to gas j which we take to be a stationary background gas ($v_j = 0$, $n_j = n$, $\mu_j = \overline{\mu}$). Also, we neglect thermal diffusion ($\alpha_{Ti} = 0$):

$$v_i = -D_i\left(\frac{n}{n_i}\frac{\partial}{\partial z}\left(\frac{n_i}{n}\right) - \frac{1}{H_a} + \frac{1}{H_i}\right) \tag{A53}$$

Finally, substituting Equation (A47) into Equation (A53) yields the diffusive flux that we use in `Photochem`:

$$\Phi_{i,\text{molecular}} = n_i v_i = -D_i n_i \left(\frac{1}{n_i}\frac{\partial n_i}{\partial z} + \frac{1}{H_i} + \frac{1}{T}\frac{\partial T}{\partial z}\right) \tag{A54}$$

For most atmospheres, we estimate the molecular diffusion coefficient with the formula (Equation 15.29 in P. M. Banks & G. Kockarts (2013))

$$D_i = \frac{b_i}{n} = \frac{1.52 \times 10^{18}}{n}\sqrt{\left(\frac{1}{\mu_i} + \frac{1}{\overline{\mu}}\right)T} \tag{A55}$$

For hydrogen-dominated atmospheres we instead compute D_i with Equation 6 in G. Gladstone et al. (1996).

A.7. *Particle Fall Velocity*

The particle fall velocity (w_i) is given by stokes law with a slip correction factor ($C_{c,i}$) (Equation 9.42 in J. Seinfeld et al. (2006)).

$$w_i = \frac{2}{9}\frac{(\rho_i - \rho)r_i^2}{\eta}C_{c,i} \tag{A56}$$

We approximate the dynamic viscosity of air (η) with the following empirical relation from Equation 1-36 and Table 1-2 in F. M. White & J. Majdalani (2006). This expression is for modern Earth air.

$$\eta = 1.716 \times 10^{-4}\left(\frac{T}{273}\right)^{3/2}\left(\frac{384}{T+111}\right) \tag{A57}$$

The slip correction factor ($C_{c,i}$), is given by Equation 9.34 in J. Seinfeld et al. (2006).

$$C_{c,i} = 1 + \frac{\lambda}{r_i}\left(-1.257 + 0.4\exp\left(\frac{1.1r_i}{\lambda}\right)\right) \tag{A58}$$

Here, λ is the mean free path, which comes from the kinetic theory of gases (Equation 9.6 in J. Seinfeld et al. (2006))

$$\lambda = \frac{2\eta}{n}\sqrt{\frac{\pi N_a}{8kT\overline{\mu}}} \tag{A59}$$

B. MODEL DATA

All nominal simulations of the photochemistry and climate of the solar system atmospheres and WASP-39b use the same chemical reaction rates, thermodynamics, photolysis cross sections, and opacities. All model data, and their source in the literature, is available at the following Zenodo archive: https://doi.org/10.5281/zenodo.15785405. Furthermore, Tables 2, 3 and 4 describe the k-distributions, CIA and Rayleigh opacities, and photolysis reactions, respectively. Table 5 lists the literature citations for the observations shown in Figures 2, 4, 6, 7, and 9.

Table 2. k-distributions used in climate calculations[a]

Species	Source	Line shape	Cutoff	Broadening
H_2O[b]	HITEMP2010, HITRAN2016 (L. S. Rothman et al. 2010; I. E. Gordon et al. 2017)	Voigt	25 cm^{-1}	Earth air
CO_2	HITEMP2010 (L. S. Rothman et al. 2010)	Sub-Lorentzian[c]	500 cm^{-1}	Self-broadening
CH_4	HITEMP2020 (R. J. Hargreaves et al. 2020)	Voigt	25 cm^{-1}	Earth air
CO	HITEMP2019 G. Li et al. (2015)	Voigt	25 cm^{-1}	Self-broadening
O_2	HITRAN2016 (I. E. Gordon et al. 2017)	Voigt	25 cm^{-1}	Earth air
O_3	HITRAN2016 (I. E. Gordon et al. 2017)	Voigt	25 cm^{-1}	Earth air
NH_3	HITRAN2016 (I. E. Gordon et al. 2017)	Voigt	25 cm^{-1}	Earth air
SO_2	HITRAN2016 (I. E. Gordon et al. 2017)	Voigt	25 cm^{-1}	Earth air
C_2H_2	Downloaded w/ HAPI[d] on 4/23/25	Voigt	25 cm^{-1}	Earth air
C_2H_6	Downloaded w/ HAPI[d] on 4/23/25	Voigt	25 cm^{-1}	Earth air
HCl	Downloaded w/ HAPI[d] on 4/23/25	Voigt	25 cm^{-1}	Earth air
N_2O	HITEMP2019 (R. J. Hargreaves et al. 2019)	Voigt	25 cm^{-1}	Earth air
OCS	Downloaded w/ HAPI[d] on 4/23/25	Voigt	25 cm^{-1}	Earth air

[a]All k-distributions were computed with HELIOS-K (S. L. Grimm et al. 2021) for temperatures between 100 and 2000 K, and pressures from 10^3 to 10^{-5} bar.
[b]Plinth or base is removed because this opacity is combined with MT_CKD H_2O continuum.
[c]M. Y. Perrin & J. M. Hartmann (1989) χ factors.
[d]HITRAN Application Programming Interface (R. V. Kochanov et al. 2016).

Table 3. CIA, Rayleigh and Aerosol opacities

Opacity type	Opacity	Citation
CIA	H_2-H_2	P. Mollière et al. (2019)
	H_2-He	P. Mollière et al. (2019)
	N_2-N_2	P. Mollière et al. (2019)
	CH_4-CH_4	T. Karman et al. (2019)
	N_2-O_2	T. Karman et al. (2019)
	O_2-O_2	T. Karman et al. (2019)
	H_2-CH_4	T. Karman et al. (2019)
	CO_2-CO_2	T. D. Robinson & D. Crisp (2018); Y. J. Lee et al. (2016)
	CO_2-CH_4	T. Karman et al. (2019)
	CO_2-H_2	T. Karman et al. (2019)
	N_2-CH_4	T. Karman et al. (2019)
	N_2-H_2	T. Karman et al. (2019)
Rayleigh scattering[a]	N_2	J. Keady & D. Kilcrease (2002); R. Penndorf (1957)
	CO_2	J. Keady & D. Kilcrease (2002); D. E. Shemansky (1972)
	O_2	J. Keady & D. Kilcrease (2002); R. Penndorf (1957)
	H_2O	J. Keady & D. Kilcrease (2002); S. Ranjan & D. D. Sasselov (2017); W. F. Murphy (1977)
	H_2	J. Keady & D. Kilcrease (2002)
	He	J. Keady & D. Kilcrease (2002); R. Penndorf (1957)
	CO	J. Keady & D. Kilcrease (2002); R. Penndorf (1957)
	CH_4	N. E. Batalha et al. (2019)
	NH_3	N. E. Batalha et al. (2019)
Aerosols[b]	H_2SO_4	K. F. Palmer & D. Williams (1975)
	Dust	M. J. Wolff et al. (2009)
	Haze	B. N. Khare et al. (1984)

[a]Rayleigh scattering opacities are computed using a parameterization from I. M. Vardavas & J. H. Carver (1984).
[b]Assumes Mie scattering.

Table 4. Photolysis reactions

#	Species	Reactions	Cross Section Ref.	Yield Ref.
P1	C	-	a	-
P2	C_2	$\rightarrow C + C$	b, a	b
P3	C_2H	$\rightarrow C_2 + H$	a	a
P4	C_2H_2	$\rightarrow C_2H + H$	b, a	a, H. Okabe (1983)
P5	C_2H_4	$\rightarrow C_2H_2 + H + H$	b, a	d
P6		$\rightarrow C_2H_2 + H_2$		
P7		$\rightarrow C_2H_3 + H$		
P8	C_2H_6	$\rightarrow C_2H_2 + H_2 + H_2$	b, a	d
P9		$\rightarrow C_2H_4 + H + H$		
P10		$\rightarrow C_2H_4 + H_2$		
P11		$\rightarrow CH_3 + CH_3$		
P12		$\rightarrow CH_4 + {}^1CH_2$		
P13	C_3H_6	$\rightarrow C_2H_2 + CH_4$	I. C. Walker et al. (2007)	d
P14		$\rightarrow C_2H_3 + CH_3$		

Table 4. Photolysis reactions

#	Species	Reactions	Cross Section Ref.	Yield Ref.
P15		$\rightarrow C_2H_4 + {}^1CH_2$		
P16		$\rightarrow C_3H_4 + H_2$		
P17	C_4H_2	$\rightarrow C_2H + C_2H$	T. Ferradaz et al. (2009); N. Smith et al. (1998)	d
P18		$\rightarrow C_2H_2 + C_2$		
P19		$\rightarrow C_4H + H$		
P20		$\rightarrow C_4H_2$		
P21	C_4H_4	$\rightarrow C_2H_2 + C_2H_2$	A. Fahr & A. Nayak (1996)	d
P22		$\rightarrow C_4H_2 + H_2$		
P23	CH	$\rightarrow C + H$	b, a	b
P24	CH_2	$\rightarrow CH + H$	a	a
P25	CH_2CO	$\rightarrow {}^1CH_2 + CO$	Assumed	Assumed
P26	CH_2N_2	$\rightarrow {}^1CH_2 + N_2$	e	Assumed
P27	CH_3	$\rightarrow {}^1CH_2 + H$	a	d
P28		$\rightarrow CH_2 + H$		
P29	CH_3CHO	$\rightarrow CH_3 + HCO$	a	b
P30		$\rightarrow CH_4 + CO$		
P31	CH_3CN	$\rightarrow CH_3 + CN$	b, a	d
P32	CH_3OH	$\rightarrow CH_3 + OH$	a	J. Hagege et al. (1968)
P33		$\rightarrow CH_3O + H$		
P34		$\rightarrow H_2CO + H_2$		
P35	CH_4	$\rightarrow {}^1CH_2 + H_2$	a, E. Karkoschka (1994); A. Y. T. Lee et al. (2001)	a, B. Gans et al. (2011)
P36		$\rightarrow CH + H_2 + H$		
P37		$\rightarrow CH_2 + H + H$		
P38		$\rightarrow CH_3 + H$		
P39	CN	$\rightarrow C + N$	b, a	a
P40	CO	$\rightarrow C + O$	b, a	a
P41	CO_2	$\rightarrow CO + O$	a, J. A. Schmidt et al. (2013)	b
P42		$\rightarrow CO + O({}^1D)$		
P43	CS	$\rightarrow C + S$	a	a
P44	CS_2	$\rightarrow CS + S$	b, a	a
P45	Cl	-	b	-
P46	Cl_2	$\rightarrow Cl + Cl$	b	b
P47	ClO	$\rightarrow Cl + O$	S. Schmidt et al. (1998)	J. B. Burkholder et al. (1990)
P48		$\rightarrow Cl + O({}^1D)$		
P49	H	-	b, a	-
P50	H_2	$\rightarrow H + H$	b, a	a
P51	H_2CO	$\rightarrow CO + H + H$	b, a	c, b
P52		$\rightarrow CO + H_2$		
P53		$\rightarrow HCO + H$		
P54	H_2O	$\rightarrow H_2 + O({}^1D)$	b, a, S. Ranjan et al. (2020)	c, T. G. Slanger & G. Black (1982); L. J. Stief et al. (1975)
P55		$\rightarrow O + H + H$		
P56		$\rightarrow OH + H$		
P57	H_2O_2	$\rightarrow OH + OH$	a	c, a
P58	H_2S	$\rightarrow HS + H$	b	b, a
P59	H_2SO_4	$\rightarrow SO_3 + H_2O$	J. R. Lane & H. G. Kjaergaard (2008)	X. Zhang et al. (2012)
P60	HCCCN	$\rightarrow C_2H + CN$	b, a	b
P61	HCN	$\rightarrow H + CN$	b, a	a

Table 4. Photolysis reactions

#	Species	Reactions	Cross Section Ref.	Yield Ref.
P62	HCO	$\rightarrow H + CO$	a	a
P63	HCl	$\rightarrow H + Cl$	a	b, a
P64	HNCO	$\rightarrow H + NCO$	b, a	b
P65		$\rightarrow NH + CO$		
P66	HNO_3	$\rightarrow OH + NO_2$	b	b
P67	HO_2	$\rightarrow OH + O$	a	b
P68	HOCl	$\rightarrow OH + Cl$	b	b
P69	HS	$\rightarrow H + S$	a	a
P70	HSO	$\rightarrow HS + O$	Assumed	Assumed
P71	He	-	b	-
P72	N	-	b, a	-
P73	N_2	$\rightarrow N + N(^2D)$	b, a	a
P74	N_2H_4	$\rightarrow N_2H_3 + H$	e, G. L. Vaghjiani (1993); H. Biehl & F. Stuhl (1991)	d
P75	N_2O	$\rightarrow N_2 + O(^1D)$	a	c, a
P76	NH	$\rightarrow N + H$	a	a
P77	NH_2	$\rightarrow NH + H$	b, a	b
P78	NH_3	$\rightarrow NH + H + H$	e, b, a, B.-M. Cheng et al. (2006)	b
P79		$\rightarrow NH + H_2$		
P80		$\rightarrow NH_2 + H$		
P81	NO	$\rightarrow N + O$	b, a	a
P82	NO_2	$\rightarrow NO + O$	c, b	a
P83	NO_3	$\rightarrow NO + O_2$	b	b
P84		$\rightarrow NO_2 + O$		
P85	O	-	b, a	-
P86	O_2	$\rightarrow O + O$	a	c
P87		$\rightarrow O + O(^1D)$		
P88	O_3	$\rightarrow O + O_2$	b, a	b, Y. Matsumi et al. (2002)
P89		$\rightarrow O(^1D) + O_2$		
P90	OCS	$\rightarrow CO + S$	a	c, a
P91	OClO	$\rightarrow ClO + O$	b	b
P92		$\rightarrow ClO + O(^1D)$		
P93	OH	$\rightarrow O + H$	b, a	a
P94	S	-	b, a	-
P95	S_2	$\rightarrow S + S$	a	a
P96	S_3	$\rightarrow S_2 + S$	R. I. Billmers & A. L. Smith (1991)	Assumed
P97	S_4	$\rightarrow S_2 + S_2$	e, R. I. Billmers & A. L. Smith (1991)	Assumed
P98		$\rightarrow S_3 + S$		
P99	S_8	-	A. M. Bass (1953)	-
P100	SO	$\rightarrow S + O$	b, a	a
P101	SO_2	$\rightarrow S + O_2$	a	b
P102		$\rightarrow SO + O$		
P103	SO_3	$\rightarrow SO_2 + O$	c	Assumed

Table 4. Photolysis reactions

#	Species	Reactions	Cross Section Ref.	Yield Ref.

Notes. a: A. N. Heays et al. (2017); b: W. F. Huebner & J. Mukherjee (2015); c: J. Burkholder et al. (2020); d: P. Lavvas et al. (2008); e: H. Keller-Rudek et al. (2013). P13: The P. Lavvas et al. (2008) paths making $CH_2CCH_2 + H_2$, $CH_3C_2H + H_2$ and $C_3H_5 + H$ are all in the $C_3H_4 + H_2$ branch. P25: Assumed to be identical to OCS. P26: We used the T = 298 K file from H. Keller-Rudek et al. (2013). P32: J. Hagege et al. (1968) reports two quantum yields, and we average them. P41: We use a low resolution version of the 270 K J. A. Schmidt et al. (2013) data. P59: We extrapolated the J. R. Lane & H. G. Kjaergaard (2008) cross section beyond 181 nm. P70: Assumed to be identical to HO_2. P73: A. N. Heays et al. (2017) Figure 10 suggests $N + N(^2D)$ is the dominant path. P88: We assume the 250 K quantum yields from Y. Matsumi et al. (2002) between 306 and 328 nm. P97: We assume even split between $S_3 + S$ and $S_2 + S_2$ chanel. P99: Extracted from Figure 2 of Bass (1953) by Kevin Zahnle. For S8 rings.

Table 5. Sources for the observations shown in Figure 2, 4, 6, 7 and 9

Planet	Species	Citations
Venus	CO	W. Wilson et al. (1981); L. Young (1972); E. Marcq et al. (2015, 2008); D. V. Cotton et al. (2012); D. Grassi et al. (2014); V. Oyama et al. (1980); V. A. Krasnopolsky (2010a); J. Pollack et al. (1993); E. Marcq et al. (2006); B. Bézard & C. de Bergh (2007); A. Collard et al. (1993); V. A. Krasnopolsky (2008); B. Fegley (2014); V. A. Krasnopolsky (2014); B. Gelman et al. (1979); V. Oyama et al. (1979); P. Connes et al. (1968); B. Bezard et al. (1990); C. C. C. Tsang et al. (2008); E. Marcq et al. (2005)
	H_2O	V. Moroz et al. (1990); T. Donahue et al. (1997); A. Fedorova et al. (2015); J. Evans & R. Ingalls (1969); A. Fedorova et al. (2016); B. Bézard et al. (2011); B. J. Sandor & R. T. Clancy (2005); L. Mukhin et al. (1982); S. Chamberlain et al. (2013); T. Encrenaz et al. (2015); G. Arney et al. (2014); E. Marcq et al. (2008); J. Bell et al. (1991); V. Meadows & D. Crisp (1996); V. Cottini et al. (2012a); J. Pollack et al. (1993); E. Marcq et al. (2006); A. Fedorova et al. (2008); T. Donahue & R. Hodges (1992); B. Bézard & C. de Bergh (2007); Y. Surkov et al. (1982); I. A. Surkov et al. (1987); C. de Bergh et al. (1995); B. Bezard et al. (1990); V. Moroz et al. (1979); C. C. C. Tsang et al. (2008)
	H_2S	V. A. Krasnopolsky (2008)
	H_2SO_4	J. Oschlisniok et al. (2012)
	HCl	P. Connes et al. (1967); G. Arney et al. (2014); B. J. Sandor & R. T. Clancy (2012); B. Bezard et al. (1990); N. Iwagami et al. (2008); L. Young (1972); V. A. Krasnopolsky (2010b)
	O_2	V. Oyama et al. (1980); L. Mukhin et al. (1982); V. Oyama et al. (1979); E. Marcq et al. (2018)
	OCS	J. Pollack et al. (1993); E. Marcq et al. (2006); G. Arney et al. (2014); E. Marcq et al. (2008); B. Bézard & C. de Bergh (2007); L. Mukhin et al. (1982); V. A. Krasnopolsky (2010a); E. Marcq et al. (2005)
	S_3	B. Maiorov et al. (2005); B. Bézard & C. de Bergh (2007); V. A. Krasnopolsky (2013)
	S_4	V. A. Krasnopolsky (2013)
	SO	C. Na et al. (1990); T. Encrenaz et al. (2015)
	SO_2	J. Pollack et al. (1993); L. Zasova et al. (1993); T. Encrenaz et al. (2012); B. Gelman et al. (1979); V. Oyama et al. (1979); C. Na et al. (1990); J. S. Greaves et al. (2021); G. Arney et al. (2014); E. Marcq et al. (2008); J.-L. Bertaux et al. (1996); B. Bézard & C. de Bergh (2007); V. Oyama et al. (1980); J. Hoffman et al. (1980)
Earth	CH_4	S. T. Massie & D. M. Hunten (1981)
	CO	B. Funke et al. (2009)
	H_2	D. H. Ehhalt et al. (1975)
	H_2O	U.S. Standard Atmosphere 1976
	H_2SO_4	A. A. Viggiano & F. Arnold (1981)
	HNO_3	S. T. Massie & D. M. Hunten (1981)
	N_2O	S. T. Massie & D. M. Hunten (1981)
	NO	S. T. Massie & D. M. Hunten (1981)
	NO_2	S. T. Massie & D. M. Hunten (1981)
	O_3	S. T. Massie & D. M. Hunten (1981)
	OCS	E. C. Y. Inn et al. (1979); M. P. Barkley et al. (2008)

Table 5. Sources for the observations shown in Figure 2, 4, 6, 7 and 9

Planet	Species	Citations
	OH	S. T. Massie & D. M. Hunten (1981)
	SO_2	H. Georgii & F. X. Meixner (1980); W. Jaeschke et al. (1976)
Mars	CO	J. Bouche et al. (2021)
	H_2O_2	T. Encrenaz et al. (2019)
	HO_2	J. Alday et al. (2024)
	NO	V. A. Krasnopolsky (2006b)
	O_2	B. Sandel et al. (2015); M. G. Trainer et al. (2019)
	O_3	M. R. Patel et al. (2021)
	H_2	V. A. Krasnopolsky & P. D. Feldman (2001)
Titan	C_2H_2	V. Vuitton et al. (2006); C. A. Nixon et al. (2013)
	C_2H_4	V. Vuitton et al. (2006); C. A. Nixon et al. (2013)
	C_2H_6	V. Vuitton et al. (2006); C. A. Nixon et al. (2013)
	CH_3CN	J. Cui et al. (2009); V. Vuitton et al. (2006); A. Marten (2002)
	CO	R. de Kok et al. (2007)
	CO_2	R. de Kok et al. (2007); J. Cui et al. (2009)
	H_2O	V. Cottini et al. (2012b); J. Cui et al. (2009)
	HCCCN	J. Cui et al. (2009); V. Vuitton et al. (2006); A. Marten (2002)
	HCN	A. Adriani et al. (2011); V. Vuitton et al. (2006); A. Marten (2002)
	NH_3	J. Cui et al. (2009); N. Teanby et al. (2013)
Jupiter	C_2H_2	J. I. Moses et al. (2005); G. Gladstone et al. (1996)
	C_2H_4	P. N. Romani et al. (2008); B. Bézard et al. (2001)
	C_2H_6	G. Gladstone et al. (1996); T. Fouchet et al. (2000)
	CH_4	P. Drossart et al. (1999)
	CO	B. Bézard et al. (2002)
	HCN	B. Bézard et al. (1995)
	NH_3	C. Moeckel et al. (2023)

Notes. We gathered most of the Venus, Earth and Jupiter observations from P. B. Rimmer et al. (2021) (their Table 5), S.-M. Tsai et al. (2021) (their Figure 9) and P. B. Rimmer & C. Helling (2016) (their Figure 12), respectively. All data is available at this Zenodo archive: https://doi.org/10.5281/zenodo.16509950.

REFERENCES

Ackerman, A. S., & Marley, M. S. 2001, ApJ, 556, 872, doi: 10.1086/321540

Adriani, A., Dinelli, B., López-Puertas, M., et al. 2011, Icarus, 214, 584–595, doi: 10.1016/j.icarus.2011.04.016

Alday, J., Trokhimovskiy, A., Belyaev, D. A., et al. 2024, Monthly Notices of the Royal Astronomical Society, 532, 4429–4435, doi: 10.1093/mnras/stae1814

Allen, M., Yung, Y. L., & Waters, J. W. 1981, J. Geophys. Res., 86, 3617, doi: 10.1029/JA086iA05p03617

Amundsen, D. S., Tremblin, P., Manners, J., Baraffe, I., & Mayne, N. J. 2017, A&A, 598, A97, doi: 10.1051/0004-6361/201629322

Arney, G., Meadows, V., Crisp, D., et al. 2014, Journal of Geophysical Research (Planets), 119, 1860, doi: 10.1002/2014JE004662

Arney, G., Domagal-Goldman, S. D., Meadows, V. S., et al. 2016, Astrobiology, 16, 873, doi: 10.1089/ast.2015.1422

Atreya, S. K., Hofstadter, M. H., In, J. H., et al. 2020, SSRv, 216, 18, doi: 10.1007/s11214-020-0640-8

Banks, P. M., & Kockarts, G. 2013, Aeronomy (Elsevier)

Barkley, M. P., Palmer, P. I., Boone, C. D., Bernath, P. F., & Suntharalingam, P. 2008, Geophysical Research Letters, 35, doi: 10.1029/2008gl034270

Bass, A. M. 1953, JChPh, 21, 80, doi: 10.1063/1.1698629

Batalha, N. E., Marley, M. S., Lewis, N. K., & Fortney, J. J. 2019, ApJ, 878, 70, doi: 10.3847/1538-4357/ab1b51

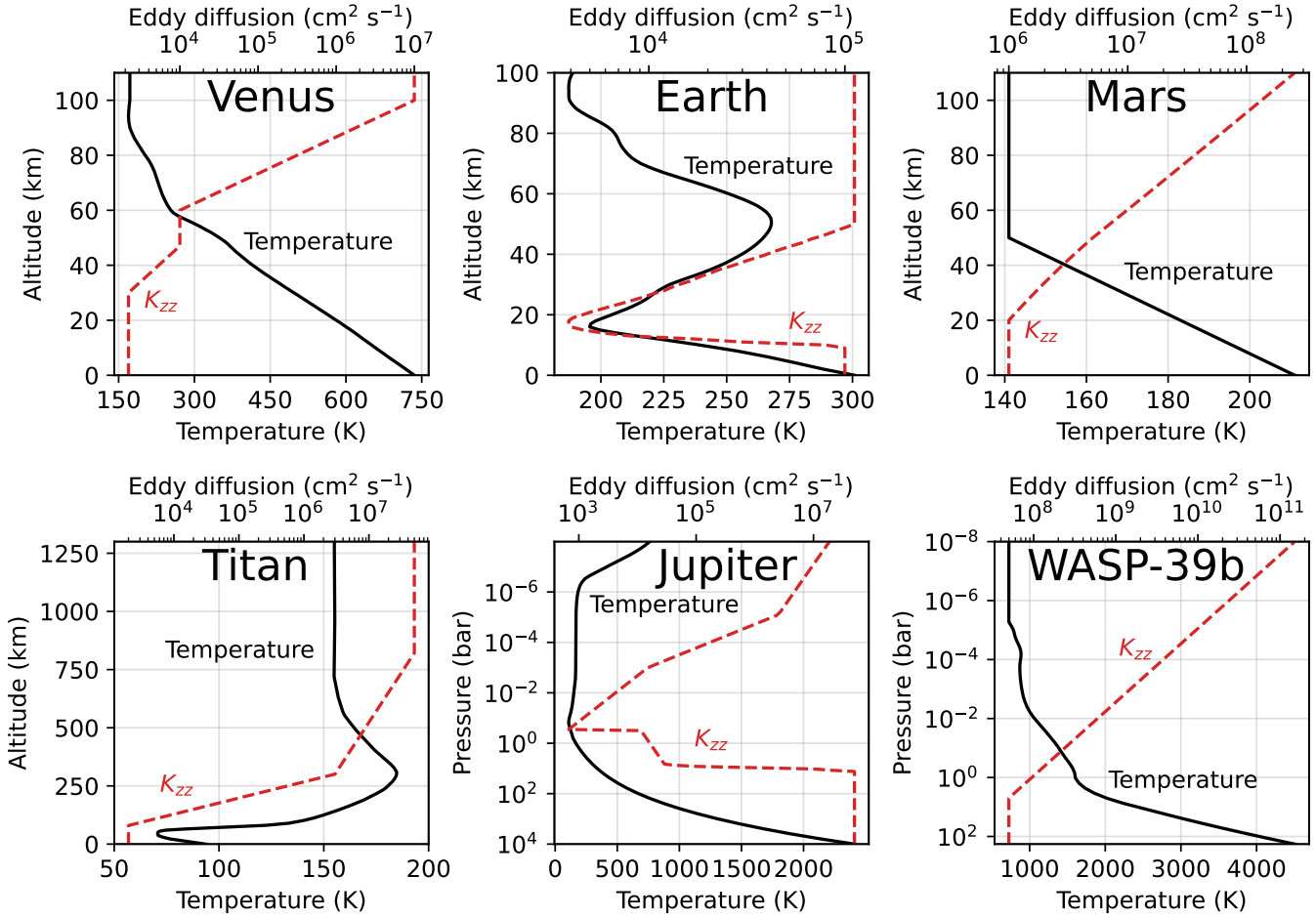

Figure 13. The temperature and eddy diffusion profiles used in our photochemical simulations of Venus, Earth, Mars, Titan, Jupiter and WASP-39b.

Behnel, S., Bradshaw, R., Citro, C., et al. 2011, Computing in Science and Engineering, 13, 31, doi: 10.1109/MCSE.2010.118

Beiler, S. A., Mukherjee, S., Cushing, M. C., et al. 2024, ApJ, 973, 60, doi: 10.3847/1538-4357/ad6759

Bell, J., Crisp, D., Lucey, P., et al. 1991, Science, 252, 1293, doi: 10.1126/science.252.5010.1293

Benneke, B., Roy, P.-A., Coulombe, L.-P., et al. 2024, arXiv e-prints, arXiv:2403.03325, doi: 10.48550/arXiv.2403.03325

Bertaux, J.-L., Widemann, T., Hauchecorne, A., Moroz, V., & Ekonomov, A. 1996, J. Geophys. Res., 101, 12709, doi: 10.1029/96JE00466

Bezard, B., de Bergh, C., Crisp, D., & Maillard, J. P. 1990, Nature, 345, 508, doi: 10.1038/345508a0

Biehl, H., & Stuhl, F. 1991, Journal of Photochemistry and Photobiology A: Chemistry, 59, 135

Bierson, C. J., & Zhang, X. 2020, Journal of Geophysical Research (Planets), 125, e06159, doi: 10.1029/2019JE006159

Billmers, R. I., & Smith, A. L. 1991, The Journal of Physical Chemistry, 95, 4242

Bouche, J., Coheur, P., Giuranna, M., et al. 2021, Journal of Geophysical Research: Planets, 126, doi: 10.1029/2020je006480

Burkholder, J., Sander, S., Abbatt, J., et al. 2020, Chemical kinetics and photochemical data for use in atmospheric studies; evaluation number 19, Tech. rep., Pasadena, CA: Jet Propulsion Laboratory, National Aeronautics and Space ...

Burkholder, J. B., Orlando, J. J., & Howard, C. J. 1990, The Journal of Physical Chemistry, 94, 687–695, doi: 10.1021/j100365a033

Bézard, B., & de Bergh, C. 2007, Journal of Geophysical Research: Planets, 112, doi: 10.1029/2006je002794

Bézard, B., Fedorova, A., Bertaux, J.-L., Rodin, A., & Korablev, O. 2011, Icarus, 216, 173, doi: 10.1016/j.icarus.2011.08.025

Bézard, B., Griffith, C., Lacy, J., & Owen, T. 1995, Icarus, 118, 384–391, doi: 10.1006/icar.1995.1198

Bézard, B., Lellouch, E., Strobel, D., Maillard, J.-P., & Drossart, P. 2002, Icarus, 159, 95–111, doi: 10.1006/icar.2002.6917

Bézard, B., Moses, J., Lacy, J., et al. 2001, in AAS/Division for Planetary Sciences Meeting Abstracts, Vol. 33, AAS/Division for Planetary Sciences Meeting Abstracts #33, 22.07

Cadieux, C., Doyon, R., MacDonald, R. J., et al. 2024, ApJL, 970, L2, doi: 10.3847/2041-8213/ad5afa

Catling, D. C., & Kasting, J. F. 2017, Atmospheric evolution on inhabited and lifeless worlds (Cambridge University Press)

Catling, D. C., Krissansen-Totton, J., Kiang, N. Y., et al. 2018, Astrobiol., 18, 709, doi: 10.1089/ast.2017.1737

Cavalié, T., Lunine, J., & Mousis, O. 2023, Nature Astronomy, 7, 678, doi: 10.1038/s41550-023-01928-8

Chamberlain, S., Bailey, J., Crisp, D., & Meadows, V. 2013, Icarus, 222, 364, doi: 10.1016/j.icarus.2012.11.014

Chapman, S., & Cowling, T. G. 1990, The mathematical theory of non-uniform gases: an account of the kinetic theory of viscosity, thermal conduction and diffusion in gases (Cambridge university press)

Cheng, B.-M., Lu, H.-C., Chen, H.-K., et al. 2006, ApJ, 647, 1535, doi: 10.1086/505615

Collard, A., Taylor, F., Calcutt, S., et al. 1993, Planet. Space Sci., 41, 487, doi: 10.1016/0032-0633(93)90031-V

Connes, P., Connes, J., Benedict, W., & Kaplan, L. 1967, ApJ, 147, 1230, doi: 10.1086/149124

Connes, P., Connes, J., Kaplan, L., & Benedict, W. 1968, ApJ, 152, 731, doi: 10.1086/149590

Constantinou, T., Shorttle, O., & Rimmer, P. B. 2025, Nature Astronomy, 9, 189, doi: 10.1038/s41550-024-02414-5

Cottini, V., Ignatiev, N., Piccioni, G., et al. 2012a, Icarus, 217, 561, doi: 10.1016/j.icarus.2011.06.018

Cottini, V., Nixon, C., Jennings, D., et al. 2012b, Icarus, 220, 855–862, doi: 10.1016/j.icarus.2012.06.014

Cotton, D. V., Bailey, J., Crisp, D., & Meadows, V. 2012, Icarus, 217, 570, doi: 10.1016/j.icarus.2011.05.020

Creecy, E. C., Li, L., Jiang, X., et al. 2021, Geophys. Res. Lett., 48, e95356, doi: 10.1029/2021GL095356

Crisp, D. 1986, Icarus, 67, 484, doi: 10.1016/0019-1035(86)90126-0

Cui, J., Yelle, R., Vuitton, V., et al. 2009, Icarus, 200, 581–615, doi: 10.1016/j.icarus.2008.12.005

Currie, M. H., & Meadows, V. S. 2025, PSJ, 6, 96, doi: 10.3847/PSJ/adc004

Dai, L., Shao, W., & Sheng, Z. 2024, A&A, 689, A55, doi: 10.1051/0004-6361/202450552

de Bergh, C., Bezard, B., Crisp, D., et al. 1995, Advances in Space Research, 15, 79, doi: 10.1016/0273-1177(94)00067-B

de Kok, R., Irwin, P., Teanby, N., et al. 2007, Icarus, 186, 354–363, doi: 10.1016/j.icarus.2006.09.016

Domagal-Goldman, S. D., Meadows, V. S., Claire, M. W., & Kasting, J. F. 2011, Astrobiology, 11, 419, doi: 10.1089/ast.2010.0509

Donahue, T., Grinspoon, D., Hartle, R., & Hodges, R. 1997, in Venus II: Geology, Geophysics, Atmosphere, and Solar Wind Environment, ed. S. W. Bougher, D. M. Hunten, & R. J. Phillips, 385

Donahue, T., & Hodges, R. 1992, J. Geophys. Res., 97, 6083, doi: 10.1029/92JE00343

Drossart, P., Fouchet, T., Crovisier, J., et al. 1999, in ESA Special Publication, Vol. 427, The Universe as Seen by ISO, ed. P. Cox & M. Kessler, 169

Ehhalt, D. H., Heidt, L. E., Lueb, R. H., & Pollock, W. 1975, pure and applied geophysics, 113, 389–402, doi: 10.1007/bf01592926

Encrenaz, T., Greathouse, T., Roe, H., et al. 2012, A&A, 543, A153, doi: 10.1051/0004-6361/201219419

Encrenaz, T., Moreno, R., Moullet, A., Lellouch, E., & Fouchet, T. 2015, Planet. Space Sci., 113, 275, doi: 10.1016/j.pss.2015.01.011

Encrenaz, T., Greathouse, T. K., Aoki, S., et al. 2019, A&A, 627, A60, doi: 10.1051/0004-6361/201935300

Evans, J., & Ingalls, R. 1969, in The Venus Atmosphere, ed. R. Jastrow & S. I. Rasool, 169

Fahr, A., & Nayak, A. 1996, Chemical Physics, 203, 351, doi: 10.1016/0301-0104(95)00401-7

Fedorova, A., Bézard, B., Bertaux, J.-L., Korablev, O., & Wilson, C. 2015, Planet. Space Sci., 113, 66, doi: 10.1016/j.pss.2014.08.010

Fedorova, A., Marcq, E., Luginin, M., et al. 2016, Icarus, 275, 143, doi: 10.1016/j.icarus.2016.04.010

Fedorova, A., Korablev, O., Vandaele, A., et al. 2008, Journal of Geophysical Research: Planets, 113, doi: 10.1029/2008je003146

Fegley, B. 2014, in Planets, Asteriods, Comets and The Solar System, ed. A. M. Davis, Vol. 2, 127–148

Ferradaz, T., Bénilan, Y., Fray, N., et al. 2009, Planet. Space Sci., 57, 10, doi: 10.1016/j.pss.2008.10.005

Filiberto, J., Trang, D., Treiman, A. H., & Gilmore, M. S. 2020, Science Advances, 6, eaax7445, doi: 10.1126/sciadv.aax7445

Fischer, E., Martínez, G. M., Rennó, N. O., Tamppari, L. K., & Zent, A. P. 2019, Journal of Geophysical Research (Planets), 124, 2780, doi: 10.1029/2019JE006080

Fortune, M., Gibson, N. P., Diamond-Lowe, H., et al. 2025, arXiv e-prints, arXiv:2505.22186. https://arxiv.org/abs/2505.22186

Fouchet, T., Lellouch, E., Bézard, B., et al. 2000, A&A, 355, L13, doi: 10.48550/arXiv.astro-ph/0002273

Funke, B., López-Puertas, M., García-Comas, M., et al. 2009, Atmospheric Chemistry and Physics, 9, 2387–2411, doi: 10.5194/acp-9-2387-2009

Gans, B., Boyé-Péronne, S., Broquier, M., et al. 2011, Physical Chemistry Chemical Physics (Incorporating Faraday Transactions), 13, 8140, doi: 10.1039/C0CP02627A

Garvin, J. B., Getty, S. A., Arney, G. N., et al. 2022, PSJ, 3, 117, doi: 10.3847/PSJ/ac63c2

Gelman, B., Zolotukhin, V., Lamonov, N., et al. 1979, An analysis of the chemical composition of the atmosphere of Venus on an AMS of the Venera-12 using a gas chromatograph,, An analysis of the chemical composition of the atmosphere of Venus on an AMS of the Venera-12 using a gas chromatograph Transl. into ENGLISH of Analiz Khimicheskogo Sostava Atmosfery Venery na AMS Venera-12 Gazovym Khromatografom (Moscow), 1979 11 p

Georgii, H., & Meixner, F. X. 1980, Journal of Geophysical Research: Oceans, 85, 7433–7438, doi: 10.1029/jc085ic12p07433

Giorgi, F., & Chameides, W. L. 1985, J. Geophys. Res., 90, 7872, doi: 10.1029/JD090iD05p07872

Gladstone, G., Allen, M., & Yung, Y. 1996, Icarus, 119, 1–52, doi: 10.1006/icar.1996.0001

Goodwin, D. G., Moffat, H. K., Schoegl, I., Speth, R. L., & Weber, B. W. 2024, Cantera: An Object-oriented Software Toolkit for Chemical Kinetics, Thermodynamics, and Transport Processes,, https://www.cantera.org doi: 10.5281/zenodo.14455267

Gordon, I. E., Rothman, L. S., Hill, C., et al. 2017, JQSRT, 203, 3, doi: 10.1016/j.jqsrt.2017.06.038

Gordon, I. E., Rothman, L. S., Hargreaves, R. J., et al. 2022, JQSRT, 277, 107949, doi: 10.1016/j.jqsrt.2021.107949

Gordon, S., & McBride, B. J. 1994, Computer program for calculation of complex chemical equilibrium compositions and applications. Part 1: Analysis, Tech. rep., NASA. https://ui.adsabs.harvard.edu/abs/2024arXiv241021364L

Graham, R. J., Lichtenberg, T., Boukrouche, R., & Pierrehumbert, R. T. 2021, PSJ, 2, 207, doi: 10.3847/PSJ/ac214c

Grassi, D., Politi, R., Ignatiev, N., et al. 2014, Journal of Geophysical Research (Planets), 119, 837, doi: 10.1002/2013JE004586

Greaves, J. S., Richards, A. M., Bains, W., et al. 2021, Nature Astronomy, 5, 655, doi: 10.1038/s41550-020-1174-4

Grimm, S. L., Malik, M., Kitzmann, D., et al. 2021, ApJS, 253, 30, doi: 10.3847/1538-4365/abd773

Hagege, J., Roberge, P., & Vermeil, C. 1968, Transactions of the Faraday Society, 64, 3288

Hargreaves, R. J., Gordon, I. E., Rey, M., et al. 2020, ApJS, 247, 55, doi: 10.3847/1538-4365/ab7a1a

Hargreaves, R. J., Gordon, I. E., Rothman, L. S., et al. 2019, JQSRT, 232, 35, doi: 10.1016/j.jqsrt.2019.04.040

Hauglustaine, D. A., Granier, C., Brasseur, G. P., & MéGie, G. 1994, J. Geophys. Res., 99, 1173, doi: 10.1029/93JD02987

Heays, A. N., Bosman, A. D., & van Dishoeck, E. F. 2017, A&A, 602, A105, doi: 10.1051/0004-6361/201628742

Hindmarsh, A. C., Brown, P. N., Grant, K. E., et al. 2005, ACM Transactions on Mathematical Software (TOMS), 31, 363

Hoffman, J., Hodges, R., Donahue, T., & McElroy, M. 1980, J. Geophys. Res., 85, 7882, doi: 10.1029/JA085iA13p07882

Hu, R., Seager, S., & Bains, W. 2012, ApJ, 761, 166, doi: 10.1088/0004-637X/761/2/166

Huebner, W. F., Keady, J. J., & Lyon, S. P. 1992, Ap&SS, 195, 1, doi: 10.1007/BF00644558

Huebner, W. F., & Mukherjee, J. 2015, Planet. Space Sci., 106, 11, doi: 10.1016/j.pss.2014.11.022

Ih, J., Kempton, E. M. R., Whittaker, E. A., & Lessard, M. 2023, ApJL, 952, L4, doi: 10.3847/2041-8213/ace03b

Inn, E. C. Y., Vedder, J. F., Tyson, B. J., & O'Hara, D. 1979, Geophysical Research Letters, 6, 191–193, doi: 10.1029/gl006i003p00191

Innes, H., Tsai, S.-M., & Pierrehumbert, R. T. 2023, ApJ, 953, 168, doi: 10.3847/1538-4357/ace346

Iwagami, N., Ohtsuki, S., Tokuda, K., et al. 2008, Planet. Space Sci., 56, 1424, doi: 10.1016/j.pss.2008.05.009

Jackson, R. B., Saunois, M., Bousquet, P., et al. 2020, Environmental Research Letters, 15, 071002, doi: 10.1088/1748-9326/ab9ed2

Jaeschke, W., Schmitt, R., & Georgii, H. 1976, Geophysical Research Letters, 3, 517–519, doi: 10.1029/gl003i009p00517

Kahre, M. A., Haberle, R. M., Wilson, R. J., et al. 2023, Icarus, 400, 115561, doi: 10.1016/j.icarus.2023.115561
Karkoschka, E. 1994, Icarus, 111, 174, doi: 10.1006/icar.1994.1139
Karman, T., Gordon, I. E., van der Avoird, A., et al. 2019, Icarus, 328, 160, doi: 10.1016/j.icarus.2019.02.034
Kasting, J. F. 1988, Icarus, 74, 472, doi: 10.1016/0019-1035(88)90116-9
Kasting, J. F. 1991, Icarus, 94, 1, doi: 10.1016/0019-1035(91)90137-I
Kasting, J. F., Liu, S. C., & Donahue, T. M. 1979, J. Geophys. Res., 84, 3097, doi: 10.1029/JC084iC06p03097
Kasting, J. F., Pollack, J. B., & Crisp, D. 1984, Journal of Atmospheric Chemistry, 1, 403, doi: 10.1007/BF00053803
Kasting, J. F., Whitmire, D. P., & Reynolds, R. T. 1993, Icarus, 101, 108, doi: 10.1006/icar.1993.1010
Keady, J., & Kilcrease, D. 2002, in Allen's Astrophysical Quantities (Springer), 95–120
Kee, R. J., Coltrin, M. E., & Glarborg, P. 2003, Chemically reacting flow: theory and practice (John Wiley & Sons)
Keller-Rudek, H., Moortgat, G. K., Sander, R., & Sörensen, R. 2013, Earth System Science Data, 5, 365, doi: 10.5194/essd-5-365-201310.5194/essdd-6-411-2013
Khare, B. N., Sagan, C., Arakawa, E. T., et al. 1984, Icarus, 60, 127, doi: 10.1016/0019-1035(84)90142-8
Knollenberg, R. G., & Hunten, D. M. 1980, J. Geophys. Res., 85, 8039, doi: 10.1029/JA085iA13p08039
Kochanov, R. V., Gordon, I. E., Rothman, L. S., et al. 2016, JQSRT, 177, 15, doi: 10.1016/j.jqsrt.2016.03.005
Kopparapu, R. K., Ramirez, R., Kasting, J. F., et al. 2013, ApJ, 765, 131, doi: 10.1088/0004-637X/765/2/131
Kozakis, T., Mendonça, J. M., & Buchhave, L. A. 2022, A&A, 665, A156, doi: 10.1051/0004-6361/202244164
Krasnopolsky, V. A. 2006a, Icarus, 185, 153, doi: 10.1016/j.icarus.2006.06.003
Krasnopolsky, V. A. 2006b, Icarus, 182, 80–91, doi: 10.1016/j.icarus.2005.12.003
Krasnopolsky, V. A. 2007, Icarus, 191, 25, doi: 10.1016/j.icarus.2007.04.028
Krasnopolsky, V. A. 2008, Icarus, 197, 377, doi: 10.1016/j.icarus.2008.05.020
Krasnopolsky, V. A. 2010a, Icarus, 209, 314, doi: 10.1016/j.icarus.2010.05.008
Krasnopolsky, V. A. 2010b, Icarus, 208, 539, doi: 10.1016/j.icarus.2010.02.012
Krasnopolsky, V. A. 2012, Icarus, 218, 230, doi: 10.1016/j.icarus.2011.11.012
Krasnopolsky, V. A. 2013, Icarus, 225, 570, doi: 10.1016/j.icarus.2013.04.026
Krasnopolsky, V. A. 2014, Icarus, 237, 340, doi: 10.1016/j.icarus.2014.04.043
Krasnopolsky, V. A., & Feldman, P. D. 2001, Science, 294, 1914–1917, doi: 10.1126/science.1065569
Krasnopolsky, V. A., & Parshev, V. A. 1981, Nature, 292, 610, doi: 10.1038/292610a0
Lane, J. R., & Kjaergaard, H. G. 2008, Journal of Physical Chemistry A, 112, 4958, doi: 10.1021/jp710863r
Lavvas, P., Coustenis, A., & Vardavas, I. 2008, Planetary and Space Science, 56, 27–66, doi: 10.1016/j.pss.2007.05.026
Lavvas, P. P., Coustenis, A., & Vardavas, I. M. 2008, Planet. Space Sci., 56, 27, doi: 10.1016/j.pss.2007.05.026
Leconte, J. 2021, A&A, 645, A20, doi: 10.1051/0004-6361/202039040
Leconte, J., Spiga, A., Clément, N., et al. 2024, A&A, 686, A131, doi: 10.1051/0004-6361/202348928
Lee, A. Y. T., Yung, Y. L., Cheng, B.-M., et al. 2001, ApJL, 551, L93, doi: 10.1086/319827
Lee, Y. J., Sagawa, H., Haus, R., et al. 2016, Journal of Geophysical Research (Planets), 121, 1737, doi: 10.1002/2016JE005087
Lei, E., & Mollière, P. 2024, arXiv e-prints, arXiv:2410.21364, doi: 10.48550/arXiv.2410.21364
LeVeque, R. J., et al. 2002, Finite volume methods for hyperbolic problems, Vol. 31 (Cambridge university press)
Li, G., Gordon, I. E., Rothman, L. S., et al. 2015, ApJS, 216, 15, doi: 10.1088/0067-0049/216/1/15
Li, L., Jiang, X., West, R. A., et al. 2018, Nature Communications, 9, 3709, doi: 10.1038/s41467-018-06107-2
Li, Q., Jacob, D. J., Yantosca, R. M., et al. 2003, Journal of Geophysical Research (Atmospheres), 108, 8827, doi: 10.1029/2002JD003075
Lincowski, A. P., Meadows, V. S., Crisp, D., et al. 2018, ApJ, 867, 76, doi: 10.3847/1538-4357/aae36a
Lincowski, A. P., Meadows, V. S., Zieba, S., et al. 2023, ApJL, 955, L7, doi: 10.3847/2041-8213/acee02
Lodders, K. 2019, arXiv e-prints, arXiv:1912.00844, doi: 10.48550/arXiv.1912.00844
Loison, J. C., Hébrard, E., Dobrijevic, M., et al. 2015, Icarus, 247, 218, doi: 10.1016/j.icarus.2014.09.039
López-Valverde, M. A., Funke, B., Brines, A., et al. 2023, Journal of Geophysical Research (Planets), 128, e2022JE007278, doi: 10.1029/2022JE007278

Maiorov, B., Ignat'ev, N., Moroz, V., et al. 2005, Solar System Research, 39, 267, doi: 10.1007/s11208-005-0042-1
Malik, M., Kempton, E. M. R., Koll, D. D. B., et al. 2019a, ApJ, 886, 142, doi: 10.3847/1538-4357/ab4a05
Malik, M., Kitzmann, D., Mendonça, J. M., et al. 2019b, AJ, 157, 170, doi: 10.3847/1538-3881/ab1084
Malik, M., Grosheintz, L., Mendonça, J. M., et al. 2017, AJ, 153, 56, doi: 10.3847/1538-3881/153/2/56
Manabe, S., & Wetherald, R. T. 1967, Journal of the Atmospheric Sciences, 24, 241, doi: 10.1175/1520-0469(1967)024⟨0241:TEOTAW⟩2.0.CO;2
Mancini, L., Esposito, M., Covino, E., et al. 2018, A&A, 613, A41, doi: 10.1051/0004-6361/201732234
Marcq, E., Bézard, B., Drossart, P., et al. 2008, Journal of Geophysical Research: Planets, 113, doi: 10.1029/2008je003074
Marcq, E., Bézard, B., Encrenaz, T., & Birlan, M. 2005, Icarus, 179, 375, doi: 10.1016/j.icarus.2005.06.018
Marcq, E., Encrenaz, T., Bézard, B., & Birlan, M. 2006, Planet. Space Sci., 54, 1360, doi: 10.1016/j.pss.2006.04.024
Marcq, E., Lellouch, E., Encrenaz, T., et al. 2015, Planet. Space Sci., 113, 256, doi: 10.1016/j.pss.2014.12.013
Marcq, E., Mills, F. P., Parkinson, C. D., & Vandaele, A. C. 2018, SSRv, 214, 10, doi: 10.1007/s11214-017-0438-5
Marten, A. 2002, Icarus, 158, 532–544, doi: 10.1006/icar.2002.6897
Massie, S. T., & Hunten, D. M. 1981, Journal of Geophysical Research: Oceans, 86, 9859–9868, doi: 10.1029/jc086ic10p09859
Matsumi, Y., Comes, F. J., Hancock, G., et al. 2002, Journal of Geophysical Research (Atmospheres), 107, 4024, doi: 10.1029/2001JD000510
McKay, C. P., Coustenis, A., Samuelson, R. E., et al. 2001, Planet. Space Sci., 49, 79, doi: 10.1016/S0032-0633(00)00051-9
McKay, C. P., Pollack, J. B., & Courtin, R. 1989, Icarus, 80, 23, doi: 10.1016/0019-1035(89)90160-7
McKay, C. P., Pollack, J. B., & Courtin, R. 1991, Science, 253, 1118, doi: 10.1126/science.11538492
Meadows, V., & Crisp, D. 1996, J. Geophys. Res., 101, 4595, doi: 10.1029/95JE03567
Meadows, V. S., Reinhard, C. T., Arney, G. N., et al. 2018, Astrobiology, 18, 630, doi: 10.1089/ast.2017.1727
Mills, F. P., & Allen, M. 2007, Planet. Space Sci., 55, 1729, doi: 10.1016/j.pss.2007.01.012
Moeckel, C., de Pater, I., & DeBoer, D. 2023, The Planetary Science Journal, 4, 25, doi: 10.3847/psj/acaf6b
Mollière, P., Wardenier, J. P., van Boekel, R., et al. 2019, A&A, 627, A67, doi: 10.1051/0004-6361/201935470
Montabone, L., Forget, F., Millour, E., et al. 2015, Icarus, 251, 65, doi: 10.1016/j.icarus.2014.12.034
Moreno, R., Lellouch, E., Lara, L. M., et al. 2012, Icarus, 221, 753, doi: 10.1016/j.icarus.2012.09.006
Moroz, V., Moshkin, B., Ekonomov, A., et al. 1979, Soviet Astronomy Letters, 5, 118
Moroz, V., Spankuch, D., Titov, D., et al. 1990, Advances in Space Research, 10, 77, doi: 10.1016/0273-1177(90)90168-Y
Moré, J. J., Garbow, B. S., & Hillstrom, K. E. 1980, User Guide for MINPACK-1, Tech. Rep. ANL-80-74, Argonne National Laboratory, Argonne, IL. https://www.osti.gov/biblio/6997562
Moses, J. I., Fouchet, T., Bézard, B., et al. 2005, Journal of Geophysical Research: Planets, 110, doi: 10.1029/2005je002411
Moses, J. I., Visscher, C., Keane, T. C., & Sperier, A. 2010, Faraday Discussions, 147, 103, doi: 10.1039/c003954c
Mount, G. H., Warden, E. S., & Moos, H. W. 1977, ApJL, 214, L47, doi: 10.1086/182440
Mukherjee, S., Batalha, N. E., Fortney, J. J., & Marley, M. S. 2023, ApJ, 942, 71, doi: 10.3847/1538-4357/ac9f48
Mukherjee, S., Fortney, J. J., Wogan, N. F., Sing, D. K., & Ohno, K. 2024, arXiv e-prints, arXiv:2410.17169, doi: 10.48550/arXiv.2410.17169
Mukherjee, S., Schlawin, E., Bell, T. J., et al. 2025, arXiv e-prints, arXiv:2502.17418, doi: 10.48550/arXiv.2502.17418
Mukhin, L., Gelman, B., Lamonov, N., et al. 1982, Soviet Astronomy Letters, 8, 216
Murphy, W. F. 1977, JChPh, 67, 5877, doi: 10.1063/1.434794
Na, C., Esposito, L., & Skinner, T. 1990, J. Geophys. Res., 95, 7485, doi: 10.1029/JD095iD06p07485
Nicovich, J. M., Kreutter, K. D., & Wine, P. H. 1990, JChPh, 92, 3539, doi: 10.1063/1.457862
Nixon, C. A., Jennings, D. E., Bézard, B., et al. 2013, The Astrophysical Journal, 776, L14, doi: 10.1088/2041-8205/776/1/l14
Okabe, H. 1983, JChPh, 78, 1312, doi: 10.1063/1.444868
Oschlisniok, J., Häusler, B., Pätzold, M., et al. 2012, Icarus, 221, 940, doi: 10.1016/j.icarus.2012.09.029
Oyama, V., Carle, G., Woeller, F., & Pollack, J. 1979, Science, 203, 802, doi: 10.1126/science.203.4382.802
Oyama, V., Carle, G., Woeller, F., et al. 1980, J. Geophys. Res., 85, 7891, doi: 10.1029/JA085iA13p07891

Palmer, K. F., & Williams, D. 1975, ApOpt, 14, 208, doi: 10.1364/AO.14.000208
Patel, M. R., Sellers, G., Mason, J. P., et al. 2021, Journal of Geophysical Research: Planets, 126, doi: 10.1029/2021je006837
Pearce, B. K. D., Molaverdikhani, K., Pudritz, R. E., Henning, T., & Hébrard, E. 2020, ApJ, 901, 110, doi: 10.3847/1538-4357/abae5c
Penndorf, R. 1957, Journal of the Optical Society of America (1917-1983), 47, 176, doi: 10.1364/JOSA.47.000176
Perrin, M. Y., & Hartmann, J. M. 1989, JQSRT, 42, 311, doi: 10.1016/0022-4073(89)90077-0
Pollack, J., Dalton, J., Grinspoon, D., et al. 1993, Icarus, 103, 1, doi: 10.1006/icar.1993.1055
Ranjan, S., & Sasselov, D. D. 2017, Astrobiology, 17, 169, doi: 10.1089/ast.2016.1519
Ranjan, S., Schwieterman, E. W., Harman, C., et al. 2020, ApJ, 896, 148, doi: 10.3847/1538-4357/ab9363
Revels, J., Lubin, M., & Papamarkou, T. 2016, arXiv:1607.07892 [cs.MS]. https://arxiv.org/abs/1607.07892
Rimmer, P. B., & Helling, C. 2016, ApJS, 224, 9, doi: 10.3847/0067-0049/224/1/9
Rimmer, P. B., Jordan, S., Constantinou, T., et al. 2021, PSJ, 2, 133, doi: 10.3847/PSJ/ac0156
Robinson, T. D., & Crisp, D. 2018, JQSRT, 211, 78, doi: 10.1016/j.jqsrt.2018.03.002
Romani, P. N., Jennings, D. E., Bjoraker, G. L., et al. 2008, Icarus, 198, 420–434, doi: 10.1016/j.icarus.2008.05.027
Rothman, L. S., Gordon, I. E., Barber, R. J., et al. 2010, JQSRT, 111, 2139, doi: 10.1016/j.jqsrt.2010.05.001
Rustamkulov, Z., Sing, D. K., Mukherjee, S., et al. 2023, Nature, 614, 659, doi: 10.1038/s41586-022-05677-y
Salawitch, R. J., McBride, L. A., Thompson, C. R., et al. 2022, Twenty Questions and Answers About the Ozone Layer: 2022 Update, Tech. rep., World Meteorological Organization
Sandel, B., Gröller, H., Yelle, R., et al. 2015, Icarus, 252, 154–160, doi: 10.1016/j.icarus.2015.01.004
Sander, R. 2015, Atmospheric Chemistry & Physics, 15, 4399, doi: 10.5194/acp-15-4399-201510.5194/acpd-14-29615-2014
Sandor, B. J., & Clancy, R. T. 2005, Icarus, 177, 129, doi: 10.1016/j.icarus.2005.03.020
Sandor, B. J., & Clancy, R. T. 2012, Icarus, 220, 618, doi: 10.1016/j.icarus.2012.05.016
Schmidt, J. A., Johnson, M. S., & Schinke, R. 2013, Proceedings of the National Academy of Science, 110, 17691, doi: 10.1073/pnas.1213083110
Schmidt, S., Benter, T., & Schindler, R. N. 1998, Chemical Physics Letters, 282, 292, doi: 10.1016/S0009-2614(97)01302-X
Schmidt, S. P., MacDonald, R. J., Tsai, S.-M., et al. 2025, arXiv e-prints, arXiv:2501.18477, doi: 10.48550/arXiv.2501.18477
Schwieterman, E. W., Kiang, N. Y., Parenteau, M. N., et al. 2018, Astrobiol., 18, 663
Schwieterman, E. W., Olson, S. L., Pidhorodetska, D., et al. 2022, ApJ, 937, 109, doi: 10.3847/1538-4357/ac8cfb
Segura, A., Kasting, J. F., Meadows, V., et al. 2005, Astrobiology, 5, 706, doi: 10.1089/ast.2005.5.706
Seiff, A., Schofield, J. T., Kliore, A. J., et al. 1985, Advances in Space Research, 5, 3, doi: 10.1016/0273-1177(85)90197-8
Seiff, A., Kirk, D. B., Knight, T. C. D., et al. 1998, J. Geophys. Res., 103, 22857, doi: 10.1029/98JE01766
Seinfeld, J., Seinfeld, P., & Pandis, S. 2006, Atmospheric Chemistry and Physics: From Air Pollution to Climate Change, Wiley-Interscience publication (Wiley)
Seinfeld, J. H., & Pandis, S. N. 2016, Atmospheric chemistry and physics: from air pollution to climate change (John Wiley & Sons)
Selsis, F., Leconte, J., Turbet, M., Chaverot, G., & Bolmont, É. 2023, Nature, 620, 287, doi: 10.1038/s41586-023-06258-3
Shemansky, D. E. 1972, JChPh, 56, 1582, doi: 10.1063/1.1677408
Slanger, T. G., & Black, G. 1982, JChPh, 77, 2432, doi: 10.1063/1.444111
Smith, N., Bénilan, Y., & Bruston, P. 1998, Planetary and space science, 46, 1215
Sohl, L. E., Fauchez, T. J., Domagal-Goldman, S., et al. 2024, PSJ, 5, 175, doi: 10.3847/PSJ/ad5830
Steudel, R., ed. 2003, Topics in Current Chemistry, Vol. 230, Elemental Sulfur and Sulfur-Rich Compounds I (Springer), doi: 10.1007/b12115
Stief, L. J., Payne, W. A., & Klemm, R. B. 1975, JChPh, 62, 4000, doi: 10.1063/1.430323
Surkov, I. A., Shcheglov, O., Ryvkin, M., Sheinin, D., & Davydov, N. 1987, Kosmicheskie Issledovaniia, 25, 678
Surkov, Y., Ivanova, V., Pudov, A., et al. 1982, Pisma v Astronomicheskii Zhurnal, 8, 411
Teanby, N., Irwin, P., Nixon, C., et al. 2013, Planetary and Space Science, 75, 136–147, doi: 10.1016/j.pss.2012.11.008
Thompson, M. A., Krissansen-Totton, J., Wogan, N., Telus, M., & Fortney, J. J. 2022, Proceedings of the National Academy of Science, 119, e2117933119, doi: 10.1073/pnas.2117933119

Thuillier, G., Floyd, L., Woods, T. N., et al. 2004, in Solar Variability and its Effects on Climate. Geophysical Monograph 141, ed. J. M. Pap, P. Fox, C. Frohlich, H. S. Hudson, J. Kuhn, J. McCormack, G. North, W. Sprigg, & S. T. Wu, Vol. 141, 171, doi: 10.1029/141GM13

Tomasko, M. G., Bézard, B., Doose, L., et al. 2008a, Planet. Space Sci., 56, 648, doi: 10.1016/j.pss.2007.10.012

Tomasko, M. G., Doose, L., Engel, S., et al. 2008b, Planet. Space Sci., 56, 669, doi: 10.1016/j.pss.2007.11.019

Tomasko, M. G., Doose, L. R., Smith, P. H., & Odell, A. P. 1980, J. Geophys. Res., 85, 8167, doi: 10.1029/JA085iA13p08167

Toon, O. B., McKay, C. P., Ackerman, T. P., & Santhanam, K. 1989, J. Geophys. Res., 94, 16287, doi: 10.1029/JD094iD13p16287

Trainer, M. G., Wong, M. H., McConnochie, T. H., et al. 2019, Journal of Geophysical Research: Planets, 124, 3000–3024, doi: 10.1029/2019je006175

Tsai, S.-M., Lyons, J. R., Grosheintz, L., et al. 2017, ApJS, 228, 20, doi: 10.3847/1538-4365/228/2/20

Tsai, S.-M., Malik, M., Kitzmann, D., et al. 2021, ApJ, 923, 264, doi: 10.3847/1538-4357/ac29bc

Tsai, S.-M., Lee, E. K. H., Powell, D., et al. 2023, Nature, 617, 483, doi: 10.1038/s41586-023-05902-2

Tsang, C. C. C., Irwin, P. G. J., Wilson, C. F., et al. 2008, Journal of Geophysical Research: Planets, 113, doi: 10.1029/2008je003089

Vaghjiani, G. L. 1993, JChPh, 98, 2123, doi: 10.1063/1.464190

Vardavas, I. M., & Carver, J. H. 1984, Planet. Space Sci., 32, 1307, doi: 10.1016/0032-0633(84)90074-6

Viggiano, A. A., & Arnold, F. 1981, Geophysical Research Letters, 8, 583–586, doi: 10.1029/gl008i006p00583

Visscher, C., & Moses, J. I. 2011, ApJ, 738, 72, doi: 10.1088/0004-637X/738/1/72

Visscher, C., Moses, J. I., & Saslow, S. A. 2010, Icarus, 209, 602, doi: 10.1016/j.icarus.2010.03.029

Vuitton, V., Yelle, R. V., & Anicich (Retired), V. G. 2006, The Astrophysical Journal, 647, L175–L178, doi: 10.1086/507467

Waite, J. H., Bell, J., Lorenz, R., Achterberg, R., & Flasar, F. M. 2013, Planet. Space Sci., 86, 45, doi: 10.1016/j.pss.2013.05.018

Walker, I. C., Holland, D. M. P., Shaw, D. A., McEwen, I. J., & Guest, M. F. 2007, Journal of Physics B Atomic Molecular Physics, 40, 1875, doi: 10.1088/0953-4075/40/10/021

White, F. M., & Majdalani, J. 2006, Viscous fluid flow, Vol. 3 (McGraw-Hill New York)

Wilson, W., Klein, M., Kahar, R., et al. 1981, Icarus, 45, 624, doi: 10.1016/0019-1035(81)90029-4

Windsor, J. D., Robinson, T. D., Kopparapu, R. k., et al. 2023, PSJ, 4, 94, doi: 10.3847/PSJ/acbf2d

Wogan, N. 2025a, Differentia, v0.1.4 Zenodo, doi: 10.5281/zenodo.15678369

Wogan, N. 2025b, SolarSystemExploration, v1.0.0 Zenodo, doi: 10.5281/zenodo.16509802

Wogan, N. 2025c, Photochem, v0.6.7 Zenodo, doi: 10.5281/zenodo.16322107

Wogan, N. 2025d, Clima, v0.5.11 Zenodo, doi: 10.5281/zenodo.15786151

Wogan, N. 2025e, Equilibrate, v0.2.0 Zenodo, doi: 10.5281/zenodo.16508386

Wogan, N. 2025f, photochem_clima_data, v0.3.0 Zenodo, doi: 10.5281/zenodo.15785405

Wogan, N. 2025g, Planetary Atmosphere Observations, v0.0.3 Zenodo, doi: 10.5281/zenodo.16509950

Wogan, N. F., Batalha, N. E., Zahnle, K. J., et al. 2024, ApJL, 963, L7, doi: 10.3847/2041-8213/ad2616

Wogan, N. F., Catling, D. C., Zahnle, K. J., & Claire, M. W. 2022, Proceedings of the National Academy of Science, 119, e2205618119, doi: 10.1073/pnas.2205618119

Wogan, N. F., Catling, D. C., Zahnle, K. J., & Lupu, R. 2023, PSJ, 4, 169, doi: 10.3847/PSJ/aced83

Wogan, N. F., Mang, J., Batalha, N. E., et al. 2025, Research Notes of the American Astronomical Society, 9, 108, doi: 10.3847/2515-5172/add407

Wolff, M. J., Smith, M. D., Clancy, R. T., et al. 2009, Journal of Geophysical Research (Planets), 114, E00D04, doi: 10.1029/2009JE003350

Wunderlich, F., Grenfell, J. L., & Rauer, H. 2023, A&A, 676, A135, doi: 10.1051/0004-6361/202142548

Xue, Q., Bean, J. L., Zhang, M., et al. 2024, ApJL, 973, L8, doi: 10.3847/2041-8213/ad72e9

Young, L. 1972, Icarus, 17, 632, doi: 10.1016/0019-1035(72)90029-2

Yu, W., & Blair, M. 2013, Computer Physics Communications, 184, 1446, doi: 10.1016/j.cpc.2012.12.025

Yung, Y. L., & Demore, W. B. 1982, Icarus, 51, 199, doi: 10.1016/0019-1035(82)90080-X

Zahnle, K., Haberle, R. M., Catling, D. C., & Kasting, J. F. 2008, Journal of Geophysical Research (Planets), 113, E11004, doi: 10.1029/2008JE003160

Zahnle, K., Marley, M. S., Morley, C. V., & Moses, J. I. 2016, ApJ, 824, 137, doi: 10.3847/0004-637X/824/2/137

Zahnle, K. J. 1986, J. Geophys. Res., 91, 2819, doi: 10.1029/JD091iD02p02819

Zasova, L., Moroz, V., Esposito, L., & Na, C. 1993, Icarus, 105, 92, doi: 10.1006/icar.1993.1113

Zhang, X., Liang, M. C., Mills, F. P., Belyaev, D. A., & Yung, Y. L. 2012, Icarus, 217, 714, doi: 10.1016/j.icarus.2011.06.016